UNIVERSITA' DEGLI STUDI DI NAPOLI

"FEDERICO II"

FACOLTA' DI INGEGNERIA

CORSO DI LAUREA IN INGEGNERIA ELETTRONICA

ACQUISITION SYSTEM FOR DETECTING IMPACTS OF HIGH ENERGY PROTON BEAMS ON THE LHC COLLIMATOR

Relatore
Ch.mo Prof.
Felice CENNAMO

Candidato
Giovanni SPIEZIA
Matr. 45/4716

Correlatore
Dott. Stefano REDAELLI

ANNO ACCADEMICO 2003/2004

CONTENTS

INTRODUCTION

This thesis work has been carried out at the European Organisation for Nuclear Research (CERN) of Geneva, where the Large Hadron Collider (LHC) is being built. The LHC machine will accelerate and bring in collision 7 TeV proton beams but also heavier ions up to lead. Two counter-rotating beams will be steered into collision at a nominal centre-of-mass energy of 14 TeV in order to study the interaction of the basic constituent of matter at the TeV energy level. This can only be achieved by using superconducting magnets that produce magnetic fields in the multi-Tesla range, required to bend and focus the particle trajectories. During stable physics runs, the total stored energy per beam will be more than 350 MJ. This large amount of energy, more than two orders of magnitude larger than what has been achieved so far in hadron storage rings, can seriously damage the beam line elements in case of accidental beam losses. Even in standard machine operation, any significant beam loss in the cold magnets must be kept under control to avoid quenches. However, beam losses cannot be completely suppressed and then the handling of the high intensity LHC beams and the associated high loss rates of protons requires a powerful collimation system. The collimator is a mechanical structure, composed by two moveable jaws, which will be placed close to the circulating beam to absorb halo particles. In order to ensure an efficient beam cleaning, several collimators will be placed in two LHC insertions dedicated to the momentum and betatron cleaning. Since the collimators sit close to the circulating beams, they will be hit by the beam in case of various accident cases. Therefore, the collimation system has also an important role in the machine protection. The design of the collimation system has recently being finalized. Presently, this design is being assessed to verify whether the proposed solution can meet the stringent LHC requirements. Collimator tests with beam have been carried out at the SPS for this purpose. Among others, it has been foreseen to hit the collimator jaws with 450 GeV proton beams at intensities of approximately 10^{13} protons. An important issue, which have been addressed in this thesis, is the detection of beam impact on the collimators in such kind of cases. As a possible solution, vibration and sound measurements of the collimator jaws were proposed to detect such kind of impact.

This work aims at the design and the test of a data acquisition system for measuring the vibrations induced by the impact of a high intensity proton beam onto the collimator. The main goal of this system is the detection of the beam impact on the collimator and then the evaluation of the induced vibrations to check the status of the collimator. The analyzing of the output data may individuate the characteristic frequencies of the collimator system and the

studying of such property should allow checking the mechanical conditions of the structure. Since the proton impact with the jaws produces a large amount of radiation, which standard electronics components cannot stand, a main requirement for the data acquisition system is the full remote control. To achieve this proposal a set of sensors were installed onto the collimator. There are 7 piezoelectric accelerometers mounted on three different points of the collimator, along different directions. A free-field microphone is installed very close to the collimator; it was used for the detection of beam induced shock wave to have a cross-check with accelerometer data. Each sensor is equipped by a preamplifier for the decoupling function. The analogic signals from the preamplifiers are sampled by a data acquisition board; the 8 channels are simultaneously sampled up to a maximum rate 102.4 kS/s. Because of the radioactive environment we need a remote control to perform the data acquisition. An application was developed in LabWindows 7.0 to allow the management of the system. It consents to perform the data acquisition, to set the software selectable parameters of the data board and of the devices which can be programmed via RS232 interface. The measurements have been performed over a wide range of beam intensities and impact parameters.

1 LHC

1.1 The LHC Project

The Large Hadron Collider (LHC) is a circular accelerator under construction at the European Organization for Nuclear Research (CERN). The LHC machine will accelerate and collide 7 TeV proton beams but also heavier ions up to lead. It will be installed in the Geneva area in a 27 Km long underground tunnel (Fig. 1.1) that has been housing the Large Electron-Positron collider (LEP) until 2000. The project has been approved in 1994 and it will be commissioned in 2007.

Fig. 1.1: Overview of the Geneva area with a drawn of the two circular accelerators: Super Proton Synchrotron (SPS 7 Km) and the larger Large Hadron Collider (LHC 27 Km).

Two counter-rotating proton beams will collide at a nominal centre-of-mass energy of14 TeV and a nominal luminosity of 10^{34} $cm^{-2}s^{-1}$ in order to study the interaction of the basic constituent of matter at the TeV energy level. The collision will allow also experiments with lead nuclei that will reach collision energies up to 1150 TeV and luminosities up to 10^{27} cm^{-2} s^{-1}.

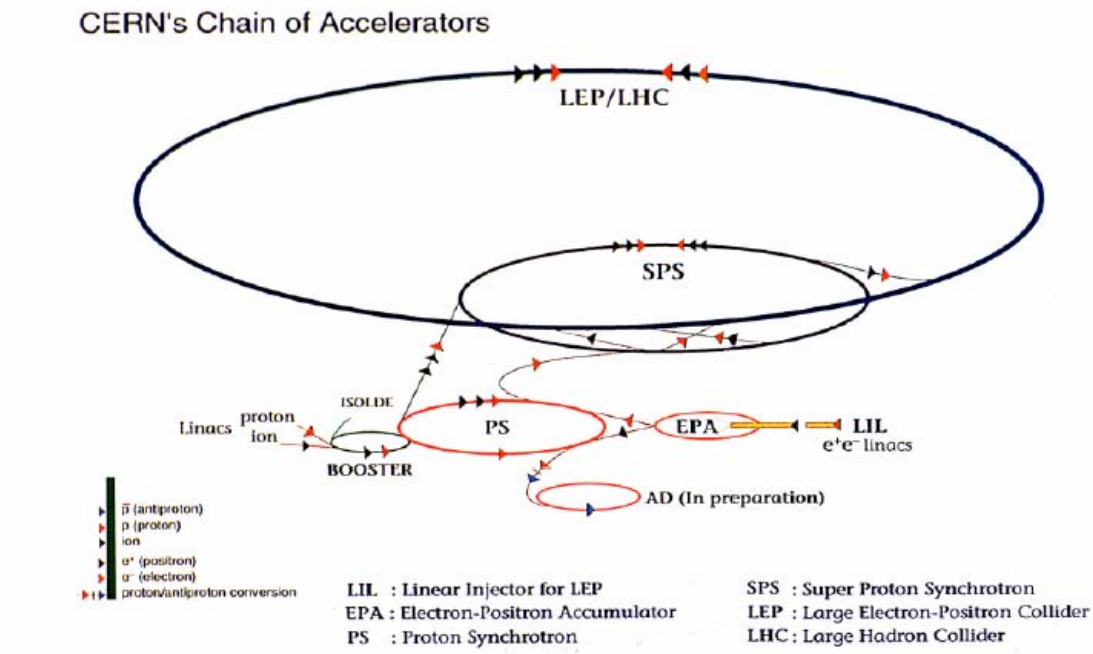

Fig.1.2: The CERN accelerators structure from the beam production trough different acceleration steps up to the largest accelerator the LHC.

Figure 1.2 shows the chain of the CERN accelerators. Bunches of about 10^{11} particles (spaced by delays of 25 to 75 ns) are prepared in the Booster and PS, and are accelerated up to the injection energy of the SPS (26 GeV). The beam will then be injected from the SPS into the LHC at the insertion points IP2 and IP8 (Fig. 1.3) at the energy of 450 GeV.

The two counter rotating proton beams will be accelerated by the Radio Frequency cavities (RF) placed at the insertion point four (IP4) in order to achieve the nominal energy of 7 TeV and then steered to collide in the centre of the four experimental detectors LHCb, ATLAS, ALICE and CMS placed in the interaction points IP8, IP1, IP2 and IP5, respectively as depicted in Fig. 1.3. The four experiments were designed to study a large range of physics: Higgs bosons, super-

symmetric particles, CP violation and B-physics. Cleaning of the beams concerning orbit (betatron cleaning) and momentum is performed at the insertion points 3 and 7. The beam dump is located atIP6.

Fig.1.3: Layout of the Large Hadron Collider project with all the interaction points, the radio frequency insertions and the beam cleaning area [3].

1.2 Particle Circular Accelerators

In general particle accelerators are machines that accelerate charged particles to high kinetic energies by applying electro magnetic fields. A particle of charge q and momentum moving through an electromagnetic field is submitted to the Coulomb and Lorentz's forces given by:

$$\vec{F} = \frac{d\vec{p}}{dt} = q(\vec{E} + \vec{v} \wedge \vec{B}) \qquad \text{(Eq. 1.1)}$$

where $\vec{F}$ is the electro magnetic force exerted by the electric field $\vec{E}$ and the magnetic field $\vec{B}$ on a particle of velocity $\vec{v}$.

The electric field $\vec{E}$ changes the particle trajectory and velocity so the momentum and the energy can be modified. This force can be used to accelerate and decelerate particles.

A constant magnetic field $\vec{B}$ normal to the particle velocity produces variations of the particle trajectory without changing the module of the particle's momentum.

Modern circular accelerators, such as the LHC, make use of both principles. The particle beams are constrained by strong magnetic fields to circulate on a closed orbit. In this condition the particle beams can be accumulated, stored in the ring and accelerated.

The acceleration is provided by a small number of cavities that accelerate the beams at each revolution by applying an electric field in the direction of the motion.

Three fundamental elements are necessary to realize this principle design:

- Particle beams have to be accelerated. Radio Frequency cavities (RF) are installed in the arc in order to increase the particle energy on every turn.
- Particles must be guided on the reference "circular" orbit; for this reason 1232 dipole field magnets will be installed in the arcs to bend the beam on the reference trajectory.
- Particle beams must maintain during their revolution a proper intensity and size, they must be focused; for this reason 360 quadrupole magnets are used to focus particles onto the reference orbit.

A complex machine like the LHC must also rely on a series of corrector magnets, which are used to stabilize the beam during its long running time.

The bending dipole field intensity is imposed by the curvature of the orbit and by the particles energy. At the equilibrium the Lorentz and the centrifugal forces of the particle beam are equal in intensity and opposite in sign. In the LHC particle beams will be highly relativistic, practically circulating at the speed of light *c*. The equilibrium condition results in the following expression:

$$|B| = \frac{E\upsilon}{\rho c^2 q} = \frac{E}{\rho c q} \qquad \text{(Eq.1.2)}$$

where E is the energy of particle of charge q and c is the speed of light.

The equilibrium condition requires a magnetic field that changes with and respect to the particle energy and velocity for a designed circular orbit of bending radius ρ.

For the LHC the orbit radius is constrained by the existing LEP tunnel, which will be used for housing the accelerator, and the energy will range from a 450 GeV injection level up to the nominal beam energy of 7 TeV.

To reach the energy of 7 TeV on a circular trajectory with a curvature radius of 2803 m, a nominal bending dipole field B of 8.33 T at collision for protons beam is calculated. Similar reasoning can be used to determine the quadrupole gradient necessary to achieve the nominal working point. The LHC quadrupoles magnets are designed for a gradient of 223 T/m and a peak field of about 7 T. These high intensity magnetic fields can only be achieved with superconducting magnets. The LHC will contain a total of 8.400 magnets, including the 1232 (15 m long) dipoles, 360 (3.25 m long) quadrupoles and the various families of corrector magnets (dipoles, quadrupoles, sextupoles, octupoles and decapoles).

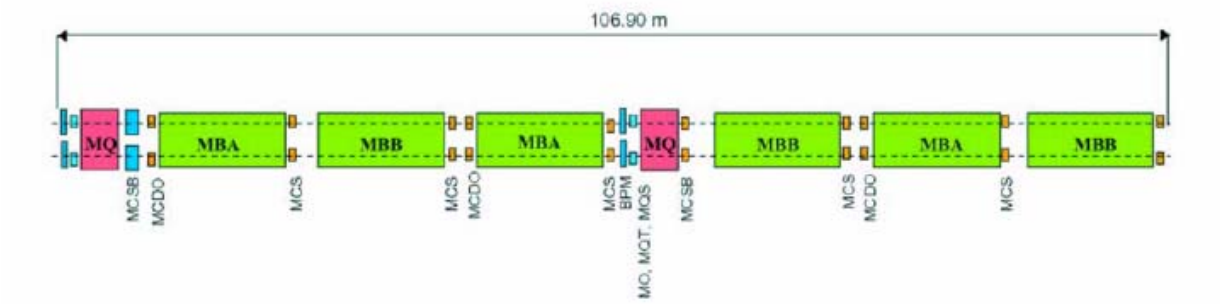

Fig. 1.4: Schematic layout of one LHC cell (one arc contains 23 cells). MBB and MBA are the main dipole magnets while MQ are the main quadrupole magnets. MQT is a trim quadrupole corrector, MQS is a skew trim quadrupole, MO is a lattice octupole, MCSB is a sextupole plus an orbit corrector (a skew sextupole). MCS are sextupole spool pieces and MCDO are octupole and decapole spool pieces.

These magnets will be installed with 8-fold symmetry in arc sectors composed mostly of regular cells (23 per sector), dispersion suppressor and matching sections and straight sections before the experiments. A regular cell has six dipole magnets and two quadrupole magnets (see Fig. 1.4). Sextupole, nested octupole and decapole magnets are placed at the ends of the main dipole magnets to correct field errors. Other octupole and combined sextupole and dipoles

corrector magnets are installed close to the main quadrupole magnets to control orbit and average beam parameters.

1.3 Harmonics tolerances from the beam dynamics

The beam enters the machine as a cloud of particles with a spread in momentum and a spread in trajectories directions with respect to the nominal energy and to the ideal orbit.

Transverse displacements of the beam would cause the loss of particles hitting the vacuum pipe if they were not guided and focused (by focusing and defocusing quadrupoles that restore particles back on the reference trajectory). As a result of the focusing and defocusing devices, every particle oscillates around the ideal orbit displaying the so-called *betatron* oscillating motion. The envelope of these oscillations follows the betatron function $\beta(s)$, where s represents the longitudinal coordinate along the design orbit. Stability requirements for the beam motion impose stringent constraints to the quality of the magnetic field of the LHC magnets. These constraints have been expressed into a set a maximum field imperfections (tolerances on the multipoles) to be achieved at operation and summarized in field quality errors tables. The tolerances have been determined considering constraints on energy and orbit, tune, coupling, second and third order chromaticity, as well as the available corrector strength and considerations of dynamic aperture. The field errors can be characterized by error contributions that are common to all magnets, called *systematic field errors*, error contributions that are typical of one magnet sub-set (e.g. manufacturer or cable type), referred to as *uncertainty field errors,* and purely *random* contributions related to the width of the normal distribution of the errors around the average. In the following we will recall the major tolerances on multipoles stemming from beam dynamics requirements.

1.4 Beam Features

1.4.1 Energy and Orbit

Particles orbiting in a circular accelerator are oscillating around the design orbit.

During their evolutions, particles go through magnets that present "field errors" and so deviate from their orbit. For this reason orbit excursions must be limited. Moreover particles have a natural spread in momentum around the nominal value. This natural spread in momentum results in different interaction of each particle with the dipole field and an orbit distortion.

The main requirements are the following:

- The peak orbit excursion should be inferior to 0.4 σ in the arc and 0.25 σ (dynamic change) in the cleaning sections, where σis the width of the Gaussian that approximates the profile of the beam density and is often called the *beam size*. The RMS orbit excursion has to be smaller than 4 mm to preserve the mechanical acceptance of the ring at the injection level.
- The energy has to be controlled within $\Delta E/E < 10^{-4}$.

1.4.2 Tune

The tune is the number of betatron oscillations per turn that particles undergo following their betatron oscillating motion travelling around the ring. The focusing and defocusing periodic fields, due to quadrupoles, determine the betatron function as well as the tune.

1.4.3 Dynamic aperture

Any variation of the current in the magnet at operation generates additional multipole field errors (b_n and a_n, with n>3). In the presence of these multipolar field components, the particle beam trajectory is modified and may become unstable. The dynamic aperture is defined as the maximum initial oscillation amplitude that guarantees stable particle motion over a given number of turns. This amplitude is expressed in multiples of the RMS beam size σ and together with the associated number of turns. For the LHC a value of 12 σis considered as safe.

1.4.4 Bunch, Batch

The bunch is a collection of particles captured within a RF bucket which is a confined region that delimits the longitudinal phase space of the particles.

The nominal bunch intensity is $N_b = 1.15 \times 10^{11}$.

Bunch duration is defined as:

$$\sigma_t = \frac{\sigma_s}{v} \qquad \text{(Eq.1.3)}$$

where v is the speed of the particles in the storage rings and σ_s is the bunch length.

The batch is a train of bunches; the PS batch is a train of 72 bunches injected into the SPS in one PS to SPS transfer, the SPS batch is a train of 4 x 72 or 3 x72 bunches injected into the LHC in one SPS to LHC transfer.

2 BEAM CLEANING AND COLLIMATION SYSTEM

2.1 Introduction

Each of the two LHC rings will handle a stored beam energy of up to 350 MJ (3×10^{14} p at 7 TeV), two orders of magnitude beyond the achievements in the Tevatron or HERA . Comparing transverse energy densities, LHC advances the state of the art by even three orders of magnitude, from 1 MJ/mm^2 to 1 GJ/mm^2. This makes the LHC beams highly destructive. At the same time the superconducting magnets in the LHC would quench at 7 TeV if small amounts of energy (on the level of 30 mJ/cm^{-3}, induced by a local transient loss of 4×10^7 protons) are deposited into the superconducting magnet coils .

Any significant beam loss into the cold aperture must therefore be avoided. However, beam losses cannot be completely suppressed. A so-called “primary beam halo” will continuously be filled by various beam dynamics processes and the beam current lifetime will be finite. The handling of the high intensity LHC beams and the associated high loss rates of protons requires a powerful collimation system with the following functionality:

1. Efficient cleaning of the beam halo during the full LHC beam cycle, such that beam-induced quenches of the super-conducting magnets are avoided during routine operation.
2. Minimization of halo-induced backgrounds in the particle physics experiments.
3. Passive protection of the machine aperture against abnormal beam loss. Beam loss monitors at the collimators detect any unusually high loss rates and generate a beam abort trigger.
4. Scraping of beam tails and diagnostics of halo population.
5. Abort gap cleaning in order to avoid spurious quenches after normal beam dumps.

The collimators must be sufficiently robust to fulfill these tasks without being damaged both during normal and abnormal operational conditions.

2.2 Design Goals

Any possible hardware solution for the collimators can only resist a small fraction of the LHC beam. The maximum beam load that is expected on the collimators must be estimated in

order to make an appropriate design. Experience from operating accelerators shows that beam losses are always higher than the theoretical optimum. Real-world beam losses are driven by imperfections, operational problems, unexpected beam physics processes, technical components operating out of specification, human errors and failures of equipment. This section summarizes the assumed beam load on the collimators. Based on these estimates the required cleaning efficiency is derived and some design principles for the layout of the collimation system are summarized. The collimation design is here described for proton-proton operation of the LHC.

2.2.1 Specification of maximum collimator beam load

Beam impact at the collimators is divided into normal and abnormal processes. Normal proton losses can occur due to beam dynamics (particle diffusion, scattering processes, and instabilities) or operational variations (orbit, tune, chromaticity changes during ramp, squeeze, collision). These losses must be minimized but cannot be avoided completely. Abnormal losses result from failure or irregular behaviour of accelerator components. The design of the collimation system relies on the specified normal and abnormal operational conditions and if these conditions are met it is expected that the collimation system will work correctly and that components will not be damaged. It is assumed that the beams are dumped when the proton loss rates exceed the specified maximum rates.

Mode	T [s]	τ [h]	R_{loss} [p/s]	P_{loss} [kW]
Injection	cont	1.0	0.8×10^{11}	6
	10	0.1	8.6×10^{11}	63
Ramp	≈ 1	0.006	1.6×10^{13}	1200
Top energy	cont	1.0	0.8×10^{11}	97
	10	0.2	4.3×10^{11}	487

Tab 2.1: Specified minimum beam lifetime τ, their duration T, the proton loss rate R_{loss}, and maximum power deposition P_{loss} in the cleaning insertion

Normal proton losses

Based on the experience with other accelerators it is expected that the beam lifetime during a fill of the LHC will sometimes drop substantially below the normal value. The collimation

system should be able to handle increased particle losses, in order to avoid beam aborts and to allow correction of parameters and restoration of nominal conditions. In particular, the range of acceptable lifetime must allow commissioning of the machine and performance tuning in nominal running. For periods of up to 10 s beam lifetimes of 0.1 h (injection) and 0.2 h (top energy) must be accepted. The peak loss rate at injection energy occurs at the start of the ramp with an expected beam lifetime of 20 s for the first second of the ramp. For continuous losses a minimum possible lifetime of 1 h is specified for injection and top energy. For details see. Table2.1 summarizes the specified lifetimes and the corresponding maximum power deposition in the cleaning insertion. The collimators should be able to withstand the specified beam load. At injection the protons impact on the material at a few micron from the collimator edge. At 7 TeV this transverse impact parameter can be as small as a few hundred nanometre.

Low beam lifetimes can occur due to orbit and optics changes, e.g. during injection, start of ramp, or squeeze. Proton losses can therefore occur locally at a single collimator jaw, where they develop into nuclear showers. The lost energy is only to a small extent dissipated in the jaw itself; the downstream elements and the surrounding materials absorb most of the proton energy.

Abnormal proton losses

Much effort has been invested into a powerful LHC machine protection system, designed to handle equipment failures. Primary proton losses will occur at the collimators if they are at nominal positions. The beam loss at the jaws is continuously monitored with fast Beam Loss Monitors. In case an abnormal increase of beam loss signal is detected, a beam abort is initiated and will be completed within 2-3 turns (178-267 μs). The beam is dumped before it can damage any accelerator components, including the collimators. The reliability of this process must be very high. Here it is assumed that in case of equipment failure the disturbed beam will always end up in the beam dump. However, this machine protection philosophy does not protect against single turn problems like irregularities of the beam dump itself and abnormally injected beam. For these fast losses any jaw can be hit, because the primary collimators only cover one phase space location and the overall LHC tune will vary. Abnormal proton losses can be due to injection failures of the extraction system. Based on this analysis of injection failures it is assumed that the amplitude of an oscillation can reach 6-10 σ and can affect both planes and therefore the collimator jaws must withstand the impact of a full injected batch without damage.

2.2.2 Definition of cleaning inefficiency

Halo particles are characterized by their normalized offsets $A_{x,y}$ in the transverse coordinates *x, y*.

The collimation system will capture most particles with large radial amplitudes. However, a secondary halo is generated from the primary collimators and a tertiary halo is leaked from the secondary collimators (see Fig. 2.1). In order to define the cleaning inefficiency η_c a variable normalized ring aperture a_c is considered.

For *N* particles impacting at the collimators, the cleaning inefficiency is then defined as the following leakage rate:

$$\eta_c(a_c, n_1, n_2) = \frac{1}{N}\sum_{i=1}^{N} H(A_r - a_c) \qquad \text{(Eq. 2.1)}$$

H is the Heaviside step function. The cleaning inefficiency gives the fraction of protons impacting on the primary collimators, which escape the collimators and reach at least a normalized ring amplitude a_c for given settings n_1 and n_2 of primary and secondary collimators. These protons will be lost into the cold aperture around the ring. Losses are diluted over some length L_{dil} and a local cleaning inefficiency is defined as:

$$\tilde{\eta}_c = \frac{\eta_c}{L_{dil}} \qquad \text{(Eq. 2.2)}$$

2.2.3 Maximum leakage rates for protection against quenches

The maximum leakage rates or in other words the required cleaning inefficiency can be specified from the maximum loss rates, the quench limit, and the dilution length. The quench level R_q is estimated to be 7×10^8 protons/m/s for 450 GeV and for slow, continuous losses.

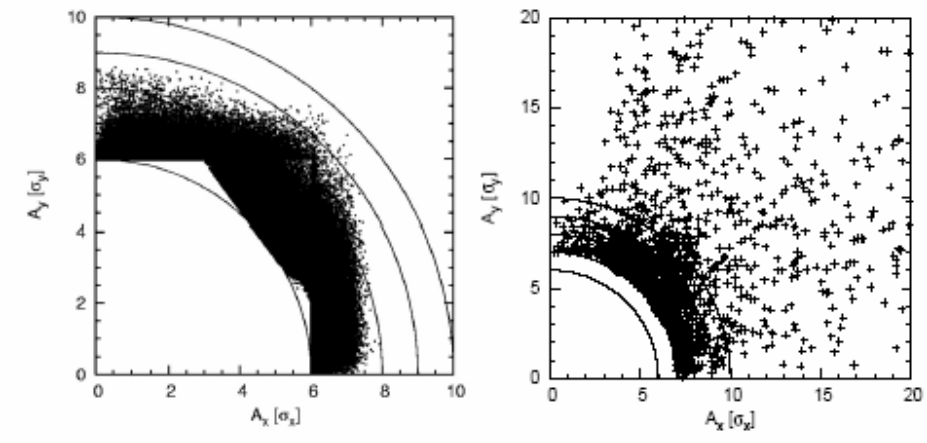

Figure 2.1 Transverse distribution of secondary (left) and tertiary (right) beam halos in normalised units

The total intensity allowed at the quench limit is shown as a function of the local collimation inefficiency in Figure 2.2. It is assumed that a minimum beam lifetime of 0.2 h at top energy and 0.1 h at injection must be ensured for operation (see Table 2.1). It is noted that the most stringent requirements on the collimation inefficiency arise at top energy. The nominal intensity of 3×10^{14} protons per beam requires a collimation inefficiency of 2×10^{-5} m^{-1}. Injection has less strict requirements. The settings n_1, n_2 and n_3 of primary, secondary and tertiary collimators must be carefully adjusted in order to minimize the leakage rates of the cleaning insertions.

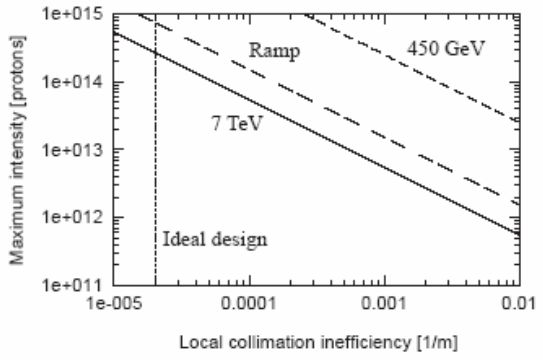

Figure 2.2: The maximum total intensity is shown as a function of the local collimation inefficiency for injection, top energy, and the start of the ramp. A beam lifetime of 0.2 h at top energy and 0.1 h at injection is assumed. The ideal design value for local inefficiency is indicated.

2.2.4 Layout Goals

In order to achieve the required low inefficiencies of around 10^{-3} (before dividing by the dilution length) several design principles have been developed and included in the layout of the LHC collimation system:

- A multi-stage cleaning process is implemented. Primary collimators intercept the lost primary protons and generate an on-momentum and off-momentum secondary proton halo. The secondary proton halo is intercepted by the secondary collimators which leak only a small tertiary halo. The tertiary halo is lost in the cold aperture but is populated sparsely enough that quenches are mostly avoided (see Figure 18.2). Tertiary collimators are used locally to provide additional protection from the tertiary halo (e.g. at the aperture bottlenecks in the triplets).
- The phase advances between different collimators and their orientations are optimized to achieve the best possible coverage in the x-x'-y-y' phase space. An additional optimization is performed to locate collimators at larger values of the beta function, thus obtaining larger opening gaps and a reduced impedance.
- As far as possible, collimators are located in front of bending magnets so that a large fraction of the proton-induced cascade is then swept out of the machine aperture and neutral particles do not propagate far downstream.
- Separately optimized cleaning systems are dedicated to the cleaning of protons with high betatron amplitudes (betatron cleaning in IR7) and off-momentum protons (momentum cleaning in IR3).
- The collimators have been located in warm sections of the machine because the warm magnets are much more tolerant to local beam losses and can accept the particle showers that exit the collimators.

2.2.5 Radiological considerations

The cleaning insertions become some of the most activated sections at the LHC.

Of particular importance for maintenance are estimates of remanent dose rates from induced radioactivity. As studies have shown, these dose rates depend strongly on various factors, such as on the collimation layout, local shielding, the materials chosen, the cooling time and the location of the collimators within the beam line layout. Close to the collimators dose rates from activated beamline components or shielding typically reach several tens of mSv/h, whereas the dose rate from the collimator jaws (on close contact) can be significantly higher. The design of the collimators and adjacent equipment (high reliability, fast connections, . . .) takes into account the fact that intervention time in these regions will have to be limited. It has been shown for the former layout that the warm magnets and other accelerator equipment in the cleaning insertions can withstand the expected radiation. However, the accumulated dose in the collimator tanks and the surrounding shielding is expected to be 1-100 MGy/year, thus rather radiation hard equipment will have to be installed. This significantly exceeds CERN's acceptable radiation dose to standard cables of 500 kGy. Since the shielding layout will be different as assumed in preceding calculations, further detailed studies might become necessary.

2.3 The concept of a phased approach

A detailed analysis of possible collimator materials and concepts did not produce any single collimator solution that fulfills all the design goals for LHC collimation (see also discussion in section 18.5). In particular it was found that a trade-off exists between collimator robustness and collimator induced impedance. In order to in spite of these problems meet the LHC design goals, a number of sub-systems have been defined which have specific tasks and which can conveniently be fitted into different installation phases. The system for beam cleaning and collimation in the LHC will be constructed and installed in three phases. This phased approach relies on the fact that difficulties and performance goals for the LHC are distributed in time, following the natural evolution of the LHC performance. The phased approach allows initial operation with a collimation system with fewer components than previously foreseen. The following section describes the different phases and the associated philosophy of beam cleaning and collimation.

2.3.1 Description of the phases

The initial phase 1 system will be the central part of the overall collimation system. The phase 1 collimation system is designed to withstand the specified beam impact and will be the system to be used for injection and ramp up to nominal or even ultimate intensities. During collisions at 7 TeV, the phase 1 collimation system may be operating at the impedance limit, limiting the maximum intensity and thus LHC luminosity. The three-stage 7 TeV set-up during phase 1 collimation is illustrated in Fig. 2.3 referring to σ at 7 TeV). Tertiary collimators in the experimental insertions provide additional shadow for the super-conducting triplet magnets.

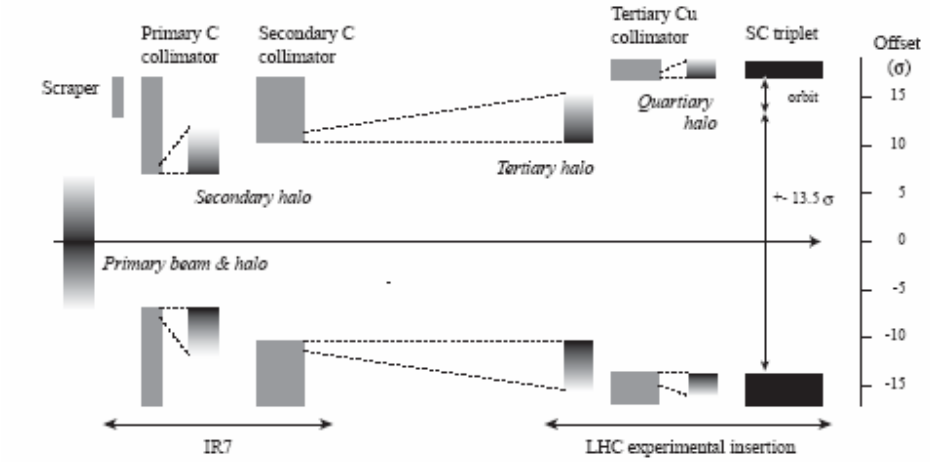

Figure 2.3: Principle of betatron collimation and beam cleaning during collision in phase 1.

The phase 2 system will complement the high robustness secondary collimators in IR3 and IR7 with 30 low impedance “hybrid” collimators. These hybrid collimators will have a reduced robustness but low impedance and excellent mechanical tolerances and will support nominal performance. The hybrid collimators will only be used in stable conditions at top energy, when risk of damage is significantly reduced.

The phase 3 several years after LHC start-up, 4 additional collimators will be installed in order to capture the high luminosity collision debris downstream of IR1 and IR5.

The phase 4 is for an eventual efficiency up grade. The collimation sub-systems in IR3 and IR7 were reduced by 16 collimators in order to reduce the number of components (total cost, work load for phase 1) and to limit their contribution to impedance. Compared to the full complement

of collimators, the associated cost in performance is a factor 2 loss in efficiency. Placeholders are kept for all suppressed collimators. If LHC operation reveals problems with cleaning efficiency, the best possible cleaning efficiency and protection can be achieved by adding the 16 collimators.

2.4 Description of the phase 1 of the collimation

Phase 1 of collimation will provide a collimation system with maximum robustness. It is accepted to operate at the LHC impedance limit and to reduce the luminosity reach somewhat below nominal performance. The system must be ready for the start-up of the LHC and will support commissioning and initial luminosity running without a further upgrade. For phase 1 it is foreseen to install 62 collimators and 6 scrapers. The numbers and types of components are given in Table 2.2.

Acronym	Number	Locations	Purpose
TCP	8	IR3, IR7	Primary collimators
TCSG	30	IR3, IR7	Secondary collimators
TCT	16	IR1, IR2, IR5, IR8	Tertiary collimators
TCLI	4	IR2, IR8	Injection protection
TCLP	4	IR1, IR5	Protection luminosity debris
TCSP	6	IR3, IR7	Beam scraping

Table 2.2: Overview on the collimators installed for phase 1 of LHC collimation. The numbers refer to the total number of elements as required for both beams.

2.4.1 High robustness graphite collimators for phase 1 (TCP/TCSG)

Collimators with maximum robustness are required for the phase 1 system. The decision was that a graphite material should be used for the LHC collimators based on the specified maximum beam load on the collimators. Both fine grain graphite (carbon, C) and fiber-reinforced graphite (carboncarbon, C-C) have sufficient robustness to withstand all specified beam load cases at injection and top energy without damage. Graphite materials exhibit a significant variation in electrical resistivity, ranging from 7 $\mu\Omega$m to about 30 $\mu\Omega$m. For impedance calculations an electrical resistivity of 14 $\mu\Omega$m (fine-grain graphite) was assumed. The specific variety of

graphite will be selected based on measurements to be made at CERN of electrical properties, vacuum performance, and mechanical tolerances.

Peak temperature increase

The energy deposition in Graphite and other materials due to a single module dump pre-fire at 7 TeV was calculated with FLUKA. The results are summarized in Table 2.3. It can be seen that graphite and beryllium exhibit a reasonable maximum temperature increase after impact of the 8 out of 2808 LHC bunches. Aluminium, titanium and copper show destructive maximum heating. The heating along the length of a collimator jaw is illustrated in Figure 2.4. The development of the particle cascade and the longitudinal position with maximum heating are visible. For a graphite secondary jaw (1 m length) the peak temperature is reached at the end of the jaw. Energy deposition was calculated for all specified beam load cases and for both protons and ions. The results indicated that graphite jaws meet the requirements of maximum robustness. They must have a transverse depth of at least 15 mm to avoid excessive showering in a higher-Z back plate.

Material	Density [g/cm^{-3}]	Max. energy deposition [GeV/cm^{-3}]	Max. temperature [°K]	Energy escaping [%]
Graphite	1.77	1.3×10^{13}	800	96.4
Beryllium	1.85	0.9×10^{13}	310	97.0
Aluminium	2.70	5.3×10^{13}	2700	88.8
Titanium	4.54	1.7×10^{14}	> 5000	79.5
Copper coating (100μm)	8.96	7.0×10^{14}	> 5000	34.4

Tab 2.3: Density, maximum energy deposition, maximum temperature, and fraction of energy escaping a 1.4 m long collimator jaw of different materials. Some materials are heated well above their melting point and it is noted that the temperature is given for illustration only.

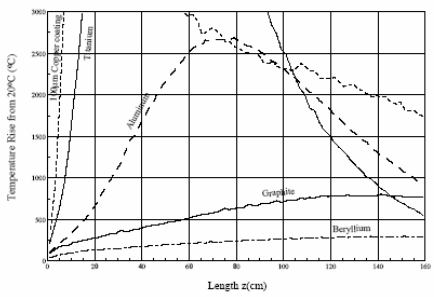

Figure 2.4: Maximum temperature increase for different longitudinal slices of a collimator block and for different materials.

Heat load and cooling

During normal operation the collimators will experience a varying heat load from electro-magnetic fields (RF heating) and from direct beam deposition and an appropriate cooling system is required. The maximum heat load occurs at 7 TeV where up to 4×10^{11} p/s can be lost for 10 s (case of 0.2 h beam lifetime). It was found that the longitudinal power density depends on the beam-to-jaw collinearity. Small misalignments reduce the length of traversal and energy is deposited in a shorter distance, e. g. a 5 μrad misalignment reduces the traversal length to 2 cm. This is illustrated in Figure 2.5. The proton induced power is then 2960 W which must be compared to a 1785 W for perfect alignment. The maximum possible peak power deposition from primary proton is expected to be close to 3 kW.

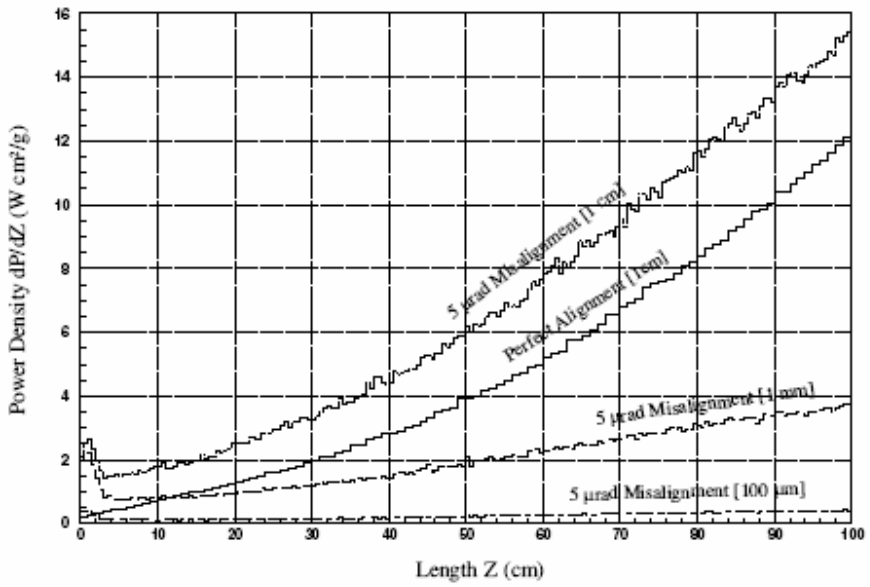

Figure 2.5: Longitudinal power density along a 1 m long graphite collimator, plotted versus the longitudinal position. It is assumed that 4×10^{11} p/s impact at 7 TeV with impact parameters of 0-200 nm (case of 0.2 h beam lifetime). The curves correspond to a perfect parallelism between protons and jaw (perfect alignment) and a 5 μrad misalignment. The power density is integrated in several transverse ranges of 0.1 mm to 10 mm.

RF heating was estimated to be below about 0.5 kW per jaw. In addition comes the power deposition due to showers that originate in upstream collimators. Energy deposition in a

secondary collimator was found to be up to 30 kW in phase 1 and 130 kW in phase 2. The maximum power deposition in a phase 1 collimator amounts to 34 kW for peak losses during 10 s. The maximum continuous power load for a specified beam lifetime of 1 h amounts to about 7 kW. In conclusion, a secondary collimator with two jaws must withstand a power load of 34 kW during 10 s and 7 kW continuously in phase 1. An appropriate cooling system is under study with the goal to hold the jaw temperature below 50 °C and to prevent significant mechanical deformations. Dedicated cooling systems are required for the two cleaning insertions. The systems will provide independent control of cooling water for each collimator. It is particularly important that the activated water can be drained and refurbished remotely during a collimator bake-out or a collimator exchange.

Impedance implications (resistivity, coating)

Graphite materials have a relatively high resistivity, ranging from 7 $\mu\Omega$m to about 30 $\mu\Omega$m. This results in significant contributions to the LHC impedance from the collimators. In order to minimize impedance it is crucial to select the graphite material with the lowest possible resistivity, if at all possible. A market survey and measurements are ongoing. A thin 1 μm coating of copper might be placed on all graphite collimators, if it can be shown that this coating will adhere reasonably well and will not damage the graphite jaw in case of abnormal beam impact.

2.4.2 Mechanical collimator design

The mechanical design of collimators that can withstand the high intensity LHC beam is challenging. Collimators do not only need to be very robust but at the same time quite long (high energy protons) and very precise (small collimation gaps). The functional requirements for TCP and TCSG collimators are summarized in Table 2.4 . The small minimum gap size of 0.5 mm and the small beam size at the collimators (200 μm rms) implies tight mechanical tolerances. These are relaxed for initial running. The numbers quoted refer to nominal running. Achieving these tolerances would in principle allow closing the TCP and TCSG collimators of phase 1 to 6 σ and 7 σ. For beam-based alignment the jaws must be remotely movable with good precision.

Reproducibility of settings is crucial in order to avoid lengthy re-optimizations. The absolute opening of the collimator gap is safety-critical and must be known at all times with good accuracy. A movement orthogonal to the collimation plane allows provision of spare surface, e.g. after coating has been locally damaged by the beam.

Parameter	Unit	TCP	TCSG
Azimuthal orientation		X, Y, S	various
Jaw material		C or C-C	C or C-C
Jaw length	cm	20	100
Jaw tapering	cm	2×10	2×10
Jaw dimensions	mm^2	65×25	65×25
Jaw coating		0-1 μm Cu	0-1 μm Cu
Jaw resistivity	$\mu\Omega$m	minimal	minimal
Surface roughness	μm	≤ 1	≤ 1.6
Surface flatness	μm	25	25
Heat load (peak)	kW	1.5	34
Heat load (continuous)	kW	1.5	7
Max. operational temperature	°C	50	50
Outbaking temperature	°C	250	250
Maximum full gap	mm	60	60
Minimum full gap	mm	0.5	0.5
Knowledge of gap	μm	50	50
Jaw position control	μm	≤ 10	≤ 10
Control jaw-beam angle	μrad	≤ 15	≤ 15
Reproducibility of setting	μm	20	20
DOF movement (hor. collimator)		X, X', Y	X, X', Y
DOF movement (vert. collimator)		Y, Y', X	Y, Y', X
Positional installation accuracy	μm	100	100
Angular installation accuracy	μrad	150	150

Tab 2.4: Functional requirements for the TCP and TCSG type collimators. The orientation of objects with one or two parallel jaws is horizontal (X), vertical (Y), or close to 45 degree (S). The required degrees of freedom (DOF) for jaw movements are listed.

Technical concept

The present technical concept (see Figure 2.6) is the result of the analysis of a wide spectrum of options and alternatives; the guiding principle for the mechanical design has been the use and optimization of proven technologies, mainly drawn from LEP collimator experience. However, due to the unprecedented specification, it was also necessary to make use of innovative technologies and novel materials, such as Carbon/ Carbon composites.

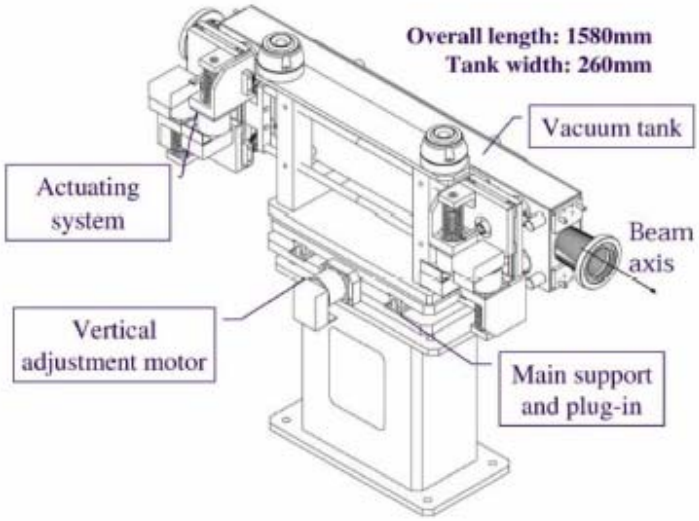

Figure 2.6: General layout and dimensions of the LHC secondary collimator (vertical configuration).

The main technical features of the LHC secondary collimators are:

1. An internal alignment system allowing both lateral displacement and angular adjustment.
2. A jaw clamping system to ensure good thermal conductance and free thermal expansion.
3. An efficient cooling system.
4. A precise actuation system including a semi-automatic mechanical return and a misalignment prevention device.
5. A plug-in external alignment system, allowing a quick and simple positioning of the collimator assembly in the machine.
6. A motorization and a control set.

The system is free from the effect of vacuum force.

The jaw assembly design

The design of the jaw assembly was chosen based on the clamping concept: the graphite or C/C jaw is pressed against the copper-made heat exchanger by a steel bar on which a series of springs is acting. The jaw assembly is held together by steel plates (see Figure 2.7). To minimize

the thermal path from the hottest spot, where the beam impact takes place, to the cooling pipes, the jaw width has been reduced to an allowable minimum (25 mm), as demanded by preliminary thermo-mechanical analysis.

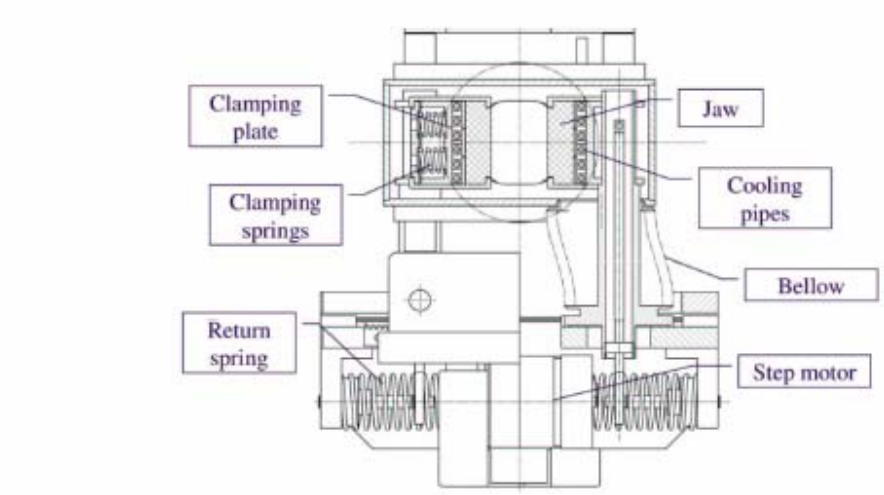

Figure 2.7: Secondary collimator mechanical assembly (cross-section of a horizontal TCSG).

Since the thermal expansion coefficient of copper is three times (or more) larger than graphite's, a fixed joint between the jaw and the copper plate is not possible, if one wants to avoid unacceptable distortions; hence, the contact must allow for relative sliding between the two surfaces. At the same time, to ensure proper heat conduction at the contact interface, a certain pressure has to be applied between these surfaces. The pressure was estimated through a semi-analytical model developed by Fuller and Marotta. A higher pressure leads to better conductance, but, in turn, it means higher mechanical stresses on the jaw; therefore a trade-off had to be found: the nominal pressure on the interface is set to 5 bar. To minimize the effect of differential thermal expansion on the jaw surface precision, the transverse distance from the two supporting axles to the internal reference surface of the jaw has been reduced to 40 mm.

The cooling system

The heat exchanger is constituted by two OFE-copper pipes per jaw brazed on one side to a copper plate and on the other to a stainless steel bar. Each pipe has three turns to increase the heat exchange (Figure 2.8). To ease the brazing and avoid harmful air traps, the pipe section is square. The inner diameter of the pipes is 6 mm. The measure of the outgassing rates of graphitic materials led to the specification of a maximum operating temperature of 50 °C for the jaw material. This imposes the use of chilled water. To meet such a strict requirement, the coolant temperature must be as low as possible: the assumed inlet temperature is 15°C to limit possible condensation problems (to this regard, a certain margin exists, since temperature could be further reduced to 12 °C). The water flow rate is 5 l/min per pipe, leading to a flow velocity of ≈3 m/s. This value is in fact rather high and might lead to erosion-corrosion problems on the soft copper pipe bends; however it is necessary both to ensure the evacuation of the high heat loads anticipated and to limit the thermally-induced deformations. In any case, the flow rate can be adjusted for each collimator by specific flow-fix valves. A cooling system is also foreseen for the outer surface of the vacuum tank.

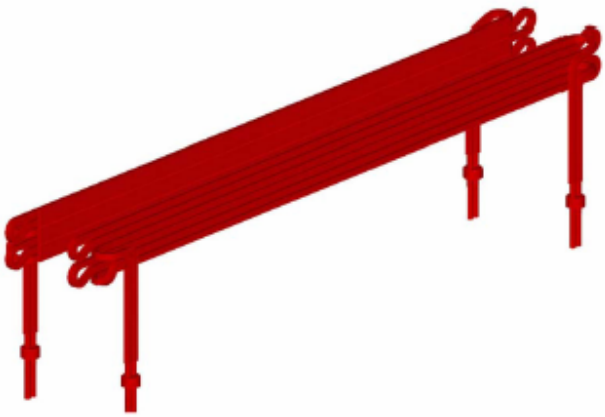

Figure 2.8: Cooling system: the multi-turn cooling pipes and the copper plates.

Motorization and actuation system

Each jaw is independently actuated by two stepper-motors (Figure 2.9). This allows both lateral displacement (with a nominal stroke of 30 mm plus 5 mm of extra-stroke) and angular

adjustment. Excessive tilt of the jaw is prevented by a rack and pinion system which avoids relative deviation between the two axes larger than 2 mm (i.e. 2 mrad). Each motor directly drives, via a roller screw/nut set, a table which allows the precise positioning of the jaw supporting axle. Each table is mounted on anti-friction linear guide-ways. The advancement for each motor step is 10 μm. Vacuum tightness is guaranteed by four bellows which can be bent sideways (not shown). The system is preloaded by a return spring to make the system play-free. The return spring also ensures a semi-automatic back-driving of the jaw in case of motor failure. The position control is guaranteed by the motor encoder and by four linear position sensors. Stops and anti-collision devices for jaw motion are also foreseen.

The vacuum tank and the external alignment system

The vacuum tank has a traditional conception. It is manufactured in AISI 316L stainless steel and mainly electron-beam welded. The structural design is the same for all the collimator configurations (horizontal, vertical or skew). The tank is supported by brackets whose design depends upon the orientation. The whole system is pre-aligned and then placed on a support table via a plug-in system. A stepper motor allows the adjustment of the whole assembly by 10 mm in order to move the jaws on the plane of collimation and present a fresher surface in the beam impact area in case the initial impact area is damaged.

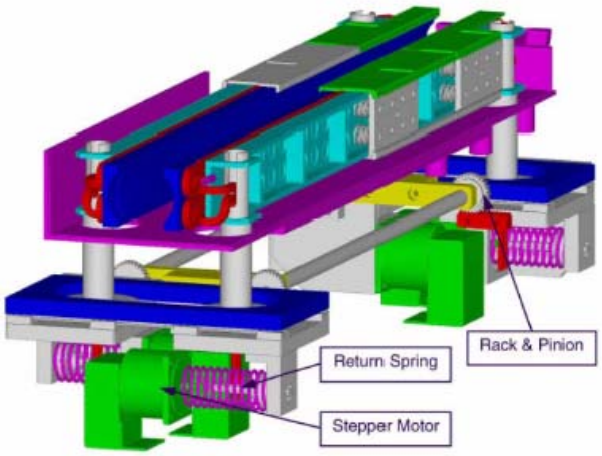

Figure 2.9: Motorization and actuation system.

2.4.3 Additional Collimators

Tertiary collimators

The most stringent requirements for the collimation system occur during collisions at 7 TeV when the stored energy is maximal and local aperture restrictions occur at the experimental triplets. In order to protect the triplets in case of the unlikely event that mis-kicked beams escape the protection systems, it is useful to install local protection. In addition, *tertiary collimators* can help to fulfill the efficiency requirements by providing a local cleaning stage at the location where it is needed. Local cleaning is highly efficient because global changes of beam parameters (orbit, beta beat) do not perturb the local shadow.

Scrapers

Scraping of proton beams is an important accelerator technique. It is often used for diagnostics purposes, control of background, or to avoid peaks in loss rate. The LHC primary collimators are specified for a minimum opening of 5 σ (about ± 1 mm). They are crucial for beam cleaning and should not be used for other purposes. It has therefore been decided to include 6 dedicated scrapers (horizontal, vertical, momentum for each beam) into the LHC design and they will be located at the corresponding primary collimators. Material, length, and detailed design of the LHC scrapers remain to be decided. Scrapers are foreseen to be installed for phase 1 of LHC collimation.

Fixed absorbers

The collimators absorb only a small fraction of the energy from the lost protons (on the order of a few %). Particle showers exit from the collimator jaws and carry the lost energy downstream. In order to avoid quenches or excessive heating, the particle cascades must be intercepted by additional fixed absorbers downstream of the collimators. Detailed shower calculations will be

performed in order to decide the length, location, and eventual cooling requirements for fixed absorbers. Absorbers will be required for phase 1 of LHC collimation.

Collimators for collision debris (TCLP)

The movable TCLP collimators are used to capture part of the debris from the p-p interactions at the experimental insertions in IR1 and IR5. They will be made out of 1 m long copper jaws and can be installed in two batches of 4 components in phase 1 and phase 3. The detailed design remains to be decided.

Injection collimators (TCLI)

Special TCLI collimators are part of the protection system for LHC injection. These movable devices complement the protection from the TDI device (it is used for injection set-up and machine protection in case of a malfunction of the injection system) and will intercept mis-kicked beam in IR2 and IR8. A detailed design remains to be decided. TCLI collimators are required for phase 1 of LHC collimation.

2.4.4 Operational conditions for collimation

The operational set-up of the LHC collimation system for significant intensities can be envisaged only after some pre-requisites have been fulfilled by LHC operation. They are listed in order of importance:

- Design aperture has been established (in particular a maximum beta beat of 20% and a maximum peak orbit of 4 mm must be guaranteed during the LHC beam cycle).
- Nominal beam loss rates have been established (the minimum beam lifetime should not drop below 0.2 h during the full LHC beam cycle).
- Transient changes in orbit and beta beat are under control, fulfilling the collimation injection tolerances (orbit and tune loops have been commissioned).

The margin gained by running with lower intensities would be used for bringing up cleaning efficiency from an initially sub-optimal to a fully optimized situation. The collimation system will be operationally characterized by the achieved cleaning efficiency and the induced impedance. It is expected that impedance limitations become apparent only at 7 TeV if more than about 40% of nominal intensity is stored with a 25 ns bunch spacing. A careful trade-off will be required to define the optimal operational strategy with collimation, based on the actually observed limitations in the LHC machine. The tertiary collimators increase the operational flexibility and introduce additional ways of optimizing performance.

2.4.5 Beam-based optimisation of collimator settings by Beam Loss Monitors

The set-up and optimization of the collimation system will be done in several beam-based steps, relying on the measurements from Beam Loss Monitors (BLM) which will be installed near every collimator. Following set-up procedures at other colliders the following logic could apply:

1. Separate beam-based calibration of each collimator: After producing a well-defined cut-off in the beam distribution (e.g. with a scraper), the two ends of each collimator jaw are moved until the beam edge is touched (witnessed by a downstream beam loss signal). This step defines an absolute reference position and angle for each jaw, which is valid for given and hopefully reproducible orbit and optics functions.
2. System set-up: After restoring the reference beam conditions all collimators are set to their target gaps and positions, directly deduced from the absolute reference positions obtained in step 1. The cleaning inefficiency is observed in a few critical BLM's in the downstream areas.
3. Empirical system tuning: The cleaning inefficiency is minimized by empirical tuning on the few relevant BLM's where quenches can occur. The most efficient collimators are optimized first. The optimization is orthogonal if the beam direction is followed. Possible cross-talks between beams can be avoided by single beam optimization.

4. Automatic tuning algorithms: Once some experience has been gained with the collimation system a more advanced automatic tuning algorithm may be envisaged, taking into account collimator response matrices.

The detailed process of set-up and optimization of the collimation system requires further studies and work.

3 EXPERIMENTAL SETUP

3.1 Overview of the installation layout

3.1.1 Goal and requirements

Before the start of the Phase 1 collimator series production, several experiments have been performed to test the required functionalities and the robustness of the collimators. In particular on October 2004 a test was performed to study the effects of the beam impact on the jaws of a secondary collimator.

The main goal of this work is the developing of a data acquisition system which must allow detecting the proton beam impact onto the collimator. The collimator has to assure the continuous working of the LHC machine by avoiding any beam loss that could occur. To achieve this proposal the collimator structure must be such robust to not get any damage due to the collision of the beam loss. However, some abnormal operational conditions may corrupt the mechanical structure of the jaws of the collimators. Thus, a diagnostic system is required to detect an eventual damage of the collimator. The data acquisition system developed allows to measure in remote mode the vibrations induced by the beam impact on the collimator, thanks to 7 accelerometers mounted in three different points of the structure. A microphone permits to measure the beam induced shock wave to have a cross-check with accelerometer data. The analysis of the vibration signals and of the microphone signal consents to individuate the collision of the proton beam on the jaws; in addition the studying in the frequency domain of the output signals may show the characteristic frequencies of the mechanical structure of the collimator. Indeed, by measuring the frequency components excited by the bump, it is possible to establish the mechanical conditions of the collimator because, if damage occurred, it changes the characteristic frequencies of the structure. The studying of the signals in the time domain may allow individuating the vibration directions and their amplitude; any change of these features should be due to different operational forms of the collimator. Thus, the evaluation of these features helps to understand the state of the collimator.

This was the first time that such measurements were performed and then the data acquisition system has to be tested too. The robustness test aims to verify the sturdiness of the

jaws of the collimator and then the proton beam will bump into the collimator at high intensity. This collision produced a high level of radiations whose effects on the instrumentation are not yet known and represent the main doubt.

3.1.2 Tunnel layout and available sensors

The robustness test was executed on a secondary collimator prototype, placed in the tunnel TT40. The following figure shows the layout of the tunnel.

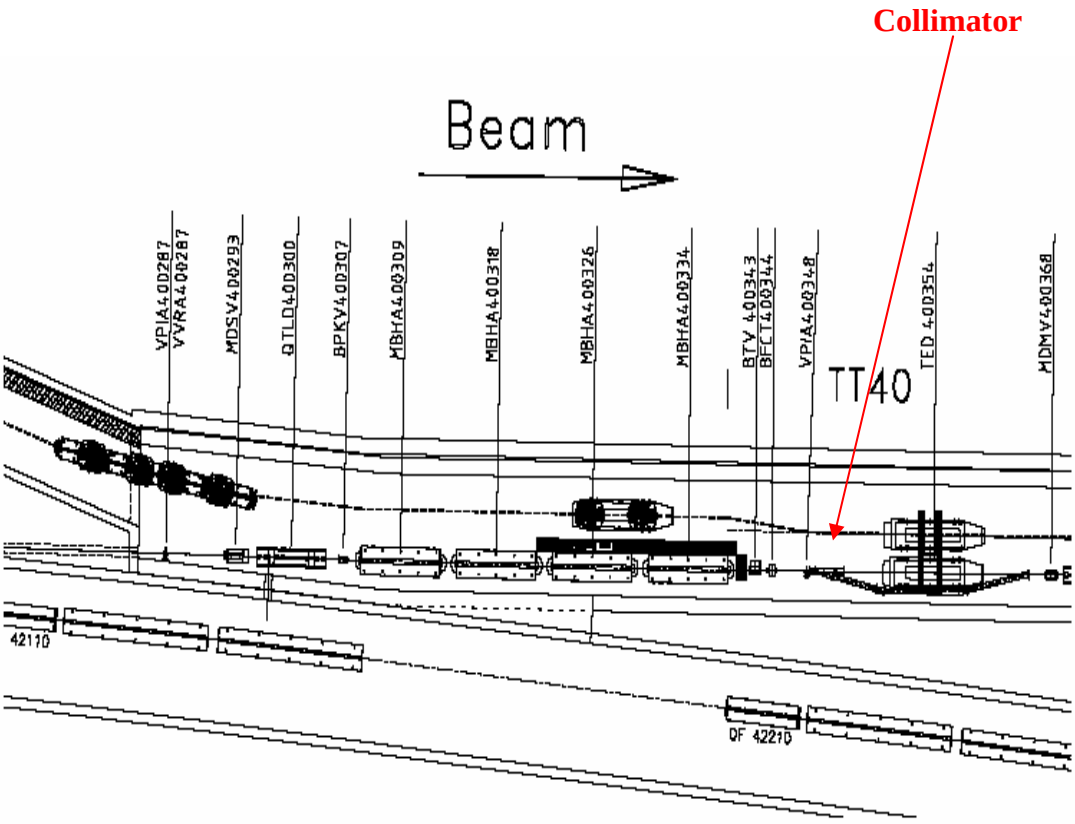

Fig. 3.1: Layout of the beam-line in TT40

The extracted beam from SPS ring will pass through the TT40 tunnel. The accelerometers are mounted on three different points along the directions shown in the Fig. 3.2.

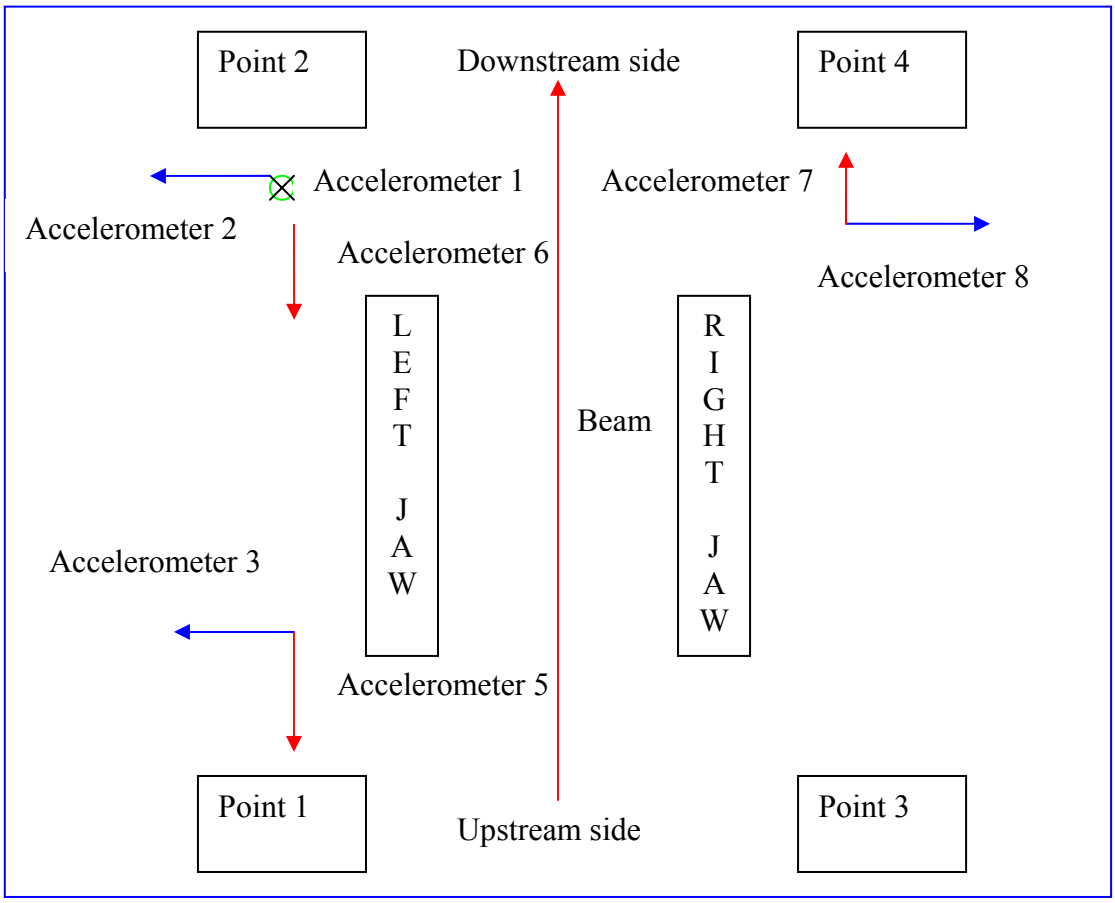

Fig. 3.2: Scheme of the installing position of the accelerometers

	Model	Position	Direction	Channel Board
Accelerometer 1	2273AM1 B&K	Downstream Left	Vertical	1
Accelerometer 2	2273A B&K	Downstream Left	Horizontal	2
Accelerometer 3	2273A B&K	Upstream Left	Horizontal	3
Microphone	B&K 4189	Upstream Left	-	4
Accelerometer 5	AP 40	Upstream Left	Longitudinal	5
Accelerometer 6	AP 40	Downstream Left	Longitudinal	6
Accelerometer 7	AP 37	Downstream Rigth	Longitudinal	7
Accelerometer 8	AP 37	Downstream Right	Horizontal	8

Tab. 3.1: Accelerometers position

The table 3.1 indicates the positions for the different kind of accelerometers and their measurement direction; the number of the accelerometer is referred to the corresponding channel of the board data acquisition to which the device is connected. Only in the point 2

(Fig. 3.3) there are three accelerometers, one for each spatial direction; both other two points are equipped with two accelerometers mounted in the directions of the beam plane.

The accelerometers have been screwed on a steal block which is mounted onto the table moved by the stepper motors, via a roller screw/nut.

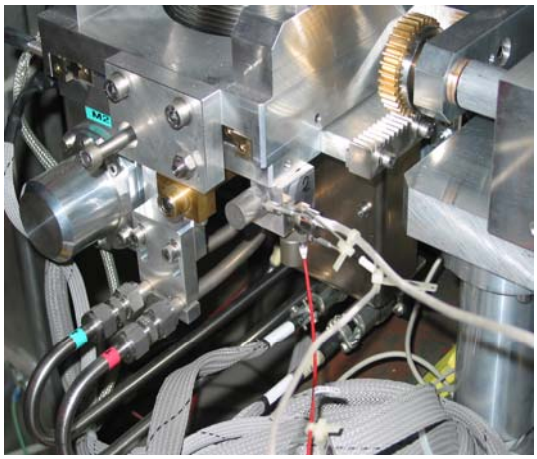

Fig. 3.3: Point2

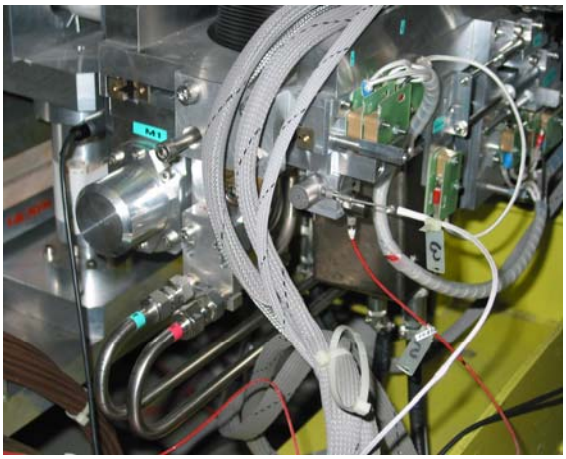

Fig.3.4:Point1

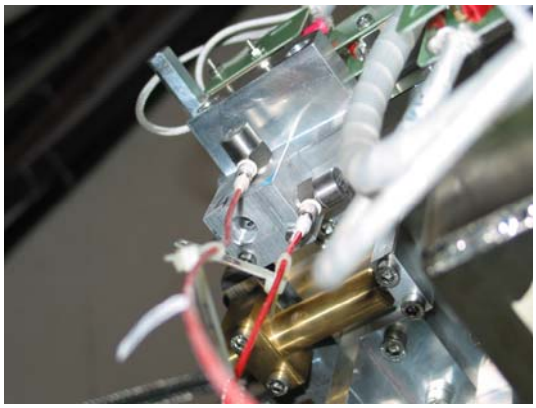

Fig. 3.5:Point4

The microphone is a NEXUS prepolarized Free-field ½" microphone (B&K), type 4189; the associated preamplifier is the Deltatron Preamplifier, type 2671. It is placed onto an iron support on the upstream left side of the collimator, oriented versus the source of the sound. The device is connected to the channel board 4.

Fig. 3.6 : Microphone

Fig. 3.7: Detail

Because of the radioactive environment, three B&K accelerometers have been chosen because the constructor guaranteed the properly working in nuclear environments. In particular they can be used in presence of an integrated gamma flux up to 6.2 x 10^{10} and integrated neutron flux up to 3.7 x 10^{18} N/cm^2 . The results of the simulations FLUKA showed that these values should guarantee the surviving of the sensors in presence of the beam at high intensity (Appendix B). The accelerometers come with special radiation hardened cables for the connection to the conditioning amplifier.

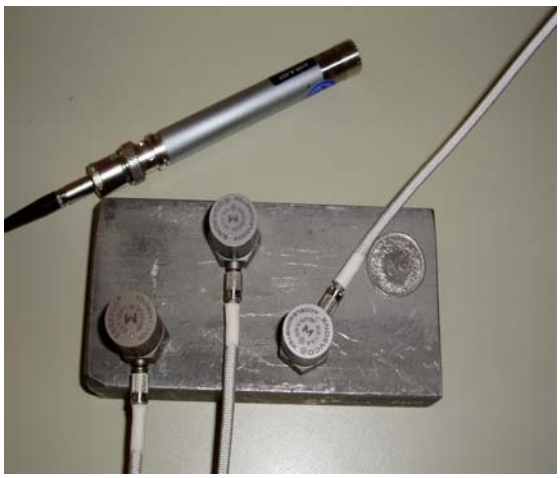

Fig. 3.8: B&K accelerometers and B&K microphone. Fig.3.9 : AP Accelerometers

The other accelerometers are AP Tech devices; they offer a low cost solution combined with extreme reliability for most vibration and shock measurement requirements. Thanks to

this trade-off between quality and low cost four AP accelerometers have been chosen to have a number of sensors enough to equip both sides of the collimator. The following tables summarize the main features of the accelerometers and of the microphone.

	Model	**Serial n°**	**Sensitivity [pC/ms^{-2}]**	**Shock limit [g]**	**Sinusoidal vibration limit [g]**
Accelerometer 1	B&K 2273AM	10624	1.085	3000	500
Accelerometer 2	B&K 2273A	11012	0.3791	10000	1000
Accelerometer 3	B&K 2273A	11010	0.3722	10000	1000
Accelerometer 5	AP 40	23712	2.1826	10000	_
Accelerometer 6	AP 40	23498	2.0602	10000	_
Accelerometer 7	AP 37	02069	0.9893	15000	_
Accelerometer 8	AP37	02053	1.0607	15000	_

Tab 3.2: Accelerometers properties

Microphone	**Response**	**Sensitivity**	**Frequency**	**Range Polarization**	**LLF (–3 dB)**
Type 4189	Free-field	41.6 mV/Pa	6.3Hz to 20 kHz	0V (prepolarized)	2 Hz to 4Hz

Tab. 3.3: Main features of the microphone.

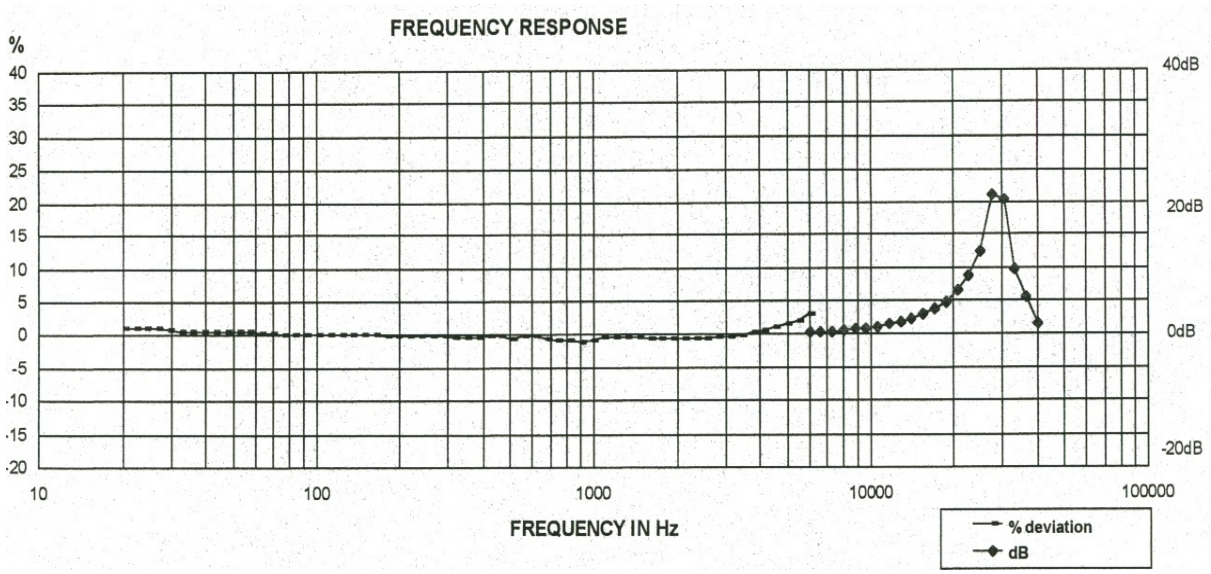

Fig. 3.10: Calibration certificate of the accelerometer B&K 2273A

It is noted that the accelerometer 1 is constructed in such way to provide mechanical isolation of the seismic mass from the mounting base, resulting in very low strain sensitivity. The case is made of Inconel and provides for hermeticity through welding and glass-to-metal fusion at the connector.

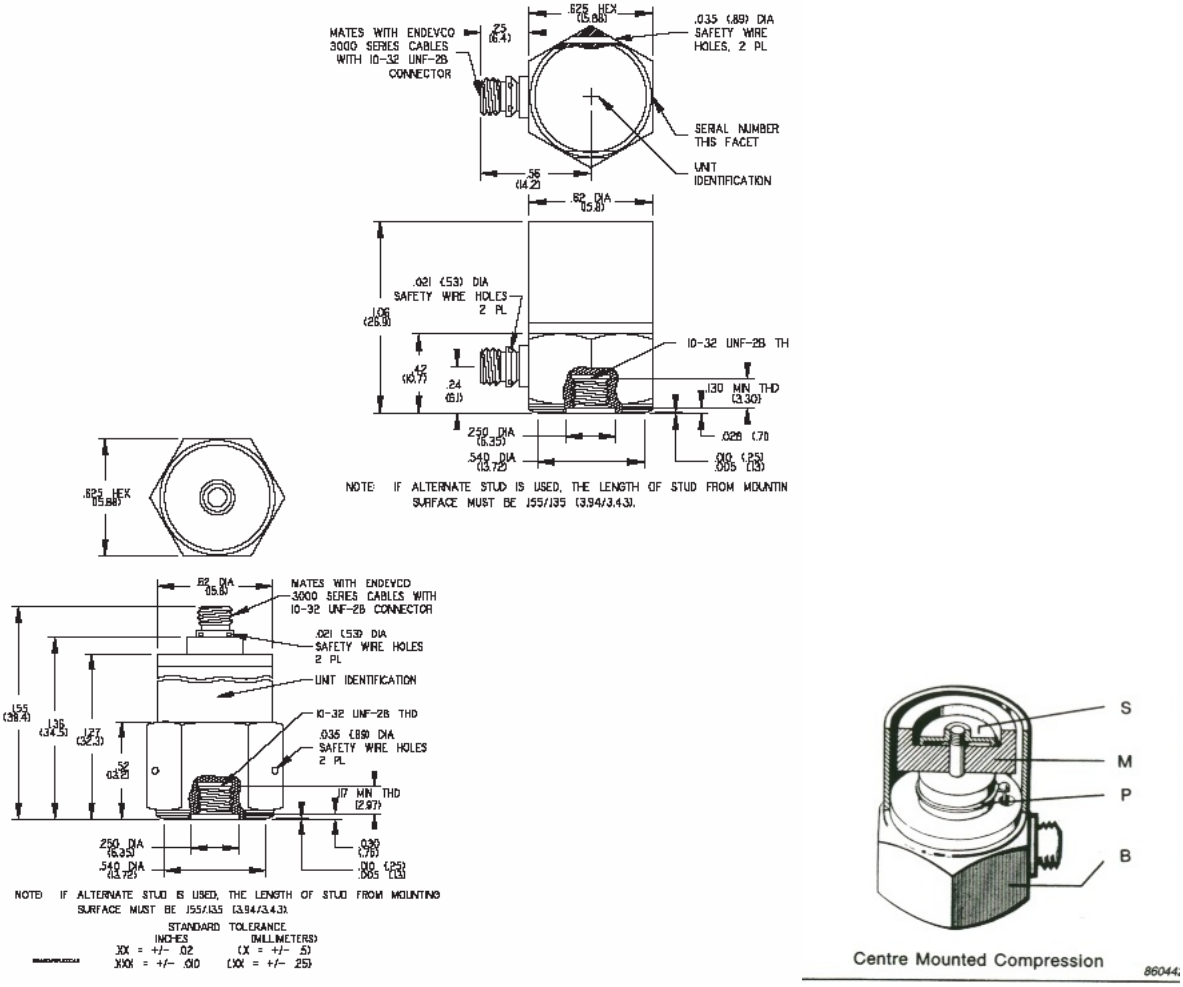

Fig. 3.11: Mechanical structure of the accelerometer 2273AM1

The signals from the three B&K accelerometers and from the microphone are converted into a low impedance signals suitable for the transmission by the B&K conditioning preamplifier NEXUS which is designed for applications where very high charge inputs (up to 100 nC) can occur. The signals from the AP accelerometers are converted by four independent line-drive amplifiers. The accelerometers are connected to the preamplifiers by special cables (for charge transmission see par. 3.2) 15 metres long. A coaxial cable has been used for the microphone. The preamplifiers are placed under a quadruple magnet. The distance of 15 metres from the collimator should be enough to avoid an influence on the

electronics due to a high radiation environment. Long cables were excluded because of the cost.

B&K preamplifier

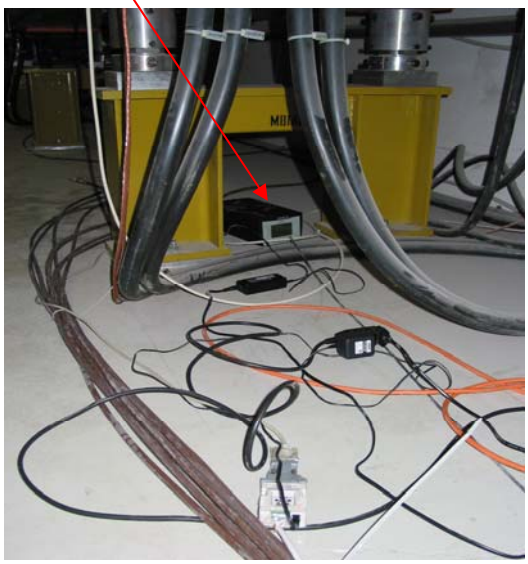

Fig. 3.12

AP preamplifier

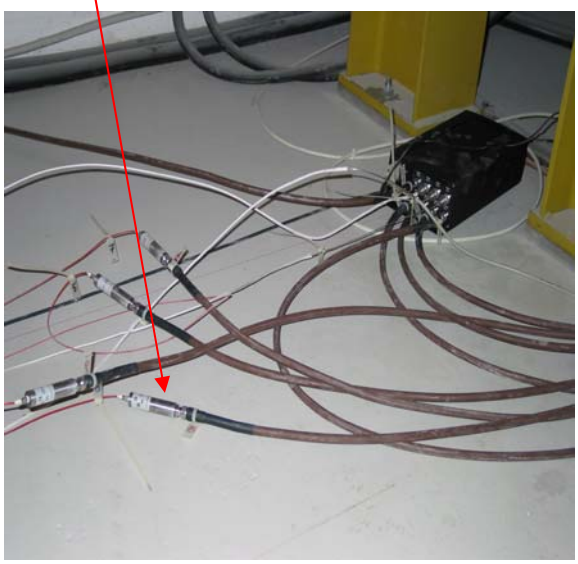

Fig. 3.13

The NEXUS preamplifier has an independent power supply and its remote control is possible by serial cable. It is very professional and it allows setting the output sensitivity for the three B&K accelerometers and the microphone. This feature gives us the possibility to change these parameters during the experiment by the remote control of the preamplifier to avoid the signal saturation. This is very important because it is the first time that such experiment was planned and then the characteristics of the vibration signal that will be acquired are unknown. The AP preamplifiers need an external DC-supply to work. For these preamplifiers no control is possible.

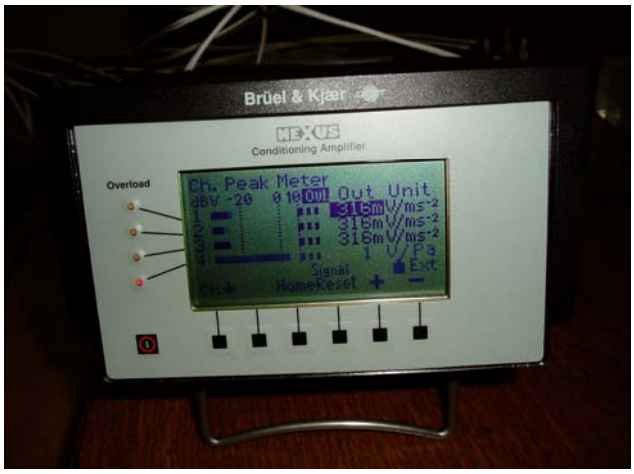

Fig. 3.14: NEXUS preamplifier

The data from these devices have been acquired with the 8-channel data-acquisition board NI 4472 installed on a pc placed in TA40. The TA40 is the access tunnel for TT40.

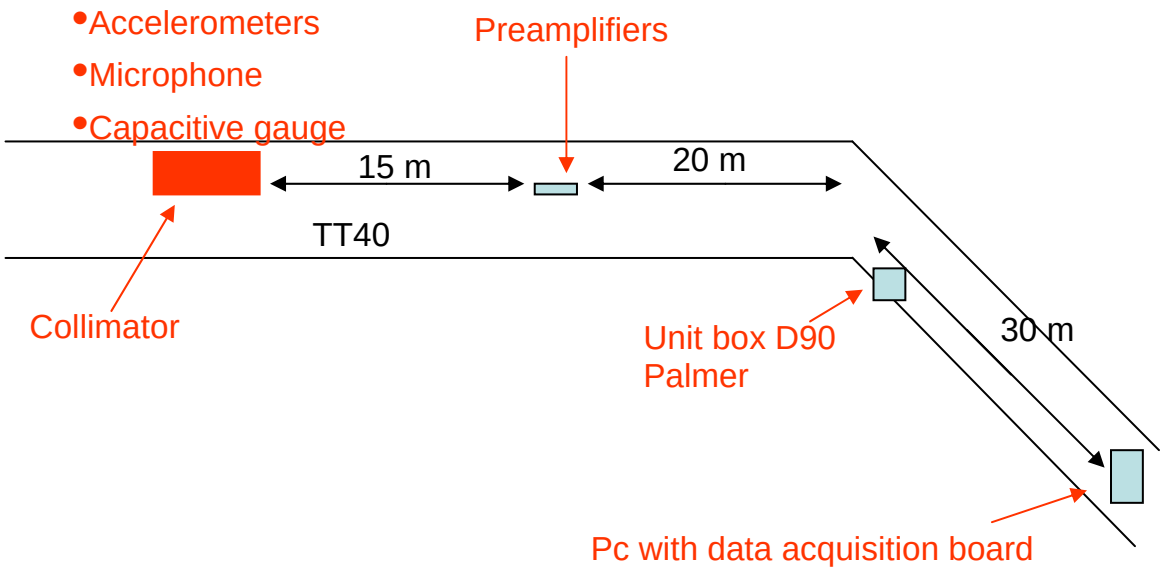

Fig. 3.15: Plan view of the TA40 Access Tunnel.

The features of the board data acquisition will be shown in the chapter 4. Coaxial cables were used for the transmission of the signals from the preamplifiers to the pc where is installed the data acquisition boards. The preamplifiers are placed in TT40 and the pc is in TA40 more than 50 metres far from the collimator. The installing position of the pc has been decided in according with the results of FLUKA simulations (Appendix B) which shows a decreasing of the radiation level only in the lower leg of TA40. However, this distance constrains to the using of long cables with a consequent increasing of the noise level. The coaxial cables present a rated capacitance 84 pF/m and a maximum attenuation 0.67 dB/m at 10 MHz.

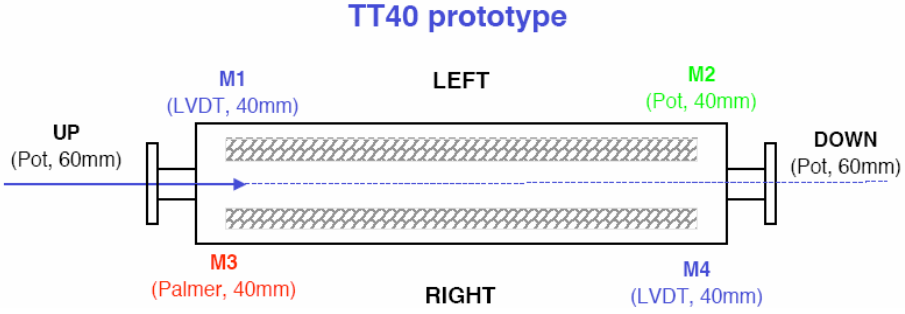

Fig. 3.16: Gauge positions installed on the collimator

These features should guarantee a good signal-ratio noise for the signal transmission. For the remote control of the NEXUS preamplifier a current-loop converter was used on both sides of the RS 232 cable because its length (50 metres) may be a problem for the correct transmission of the RS 232 command.

Fig. 3.17: Current loop converter

In addition to the vibration measurements, it was planned to lead also a continuous monitoring of the position of a jaw of the collimator by a position sensor that was independent from the other devices for the position measurements installed on the collimator. It is noted this measurement is independent from the vibration analysis. A Sylvac capacitive gauge was installed on the right jaw and connected to the Unit Display D90 (Sylvac) by a 30 metres long cable which consents to install the Display box at the end of the access tunnel TA40 (Fig. 3.15), about 30 metres far from the place of the pc. The cable of 30 metres was not a standard accessory and then a special recalibration of the electronic input circuit of display unit was required. This device has to measure the position of the jaw in respect to the beam.

Capacitive gauge

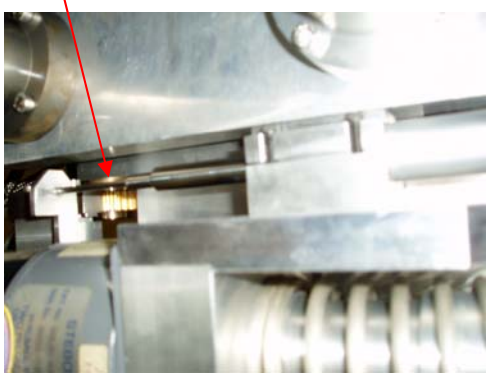

Fig. 3.18: Capacitive gauge on the right jaw

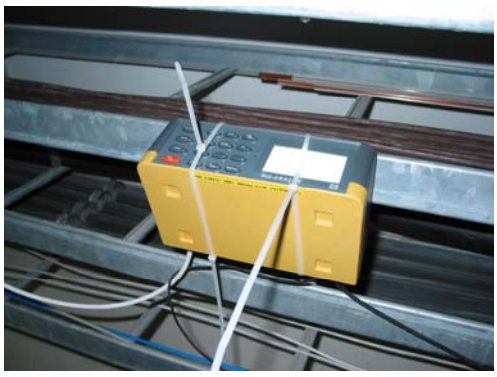

Fig. 3.19: Display unit D90

Due to the impossibility to access to the experiment place, a power supply switch was prepared to allow the physical reset of the calculator in TA40; the switch is checked by a

micro-pc to which we can access by a web server. Here a scheme is presented to show the architecture of the entire data acquisition system:

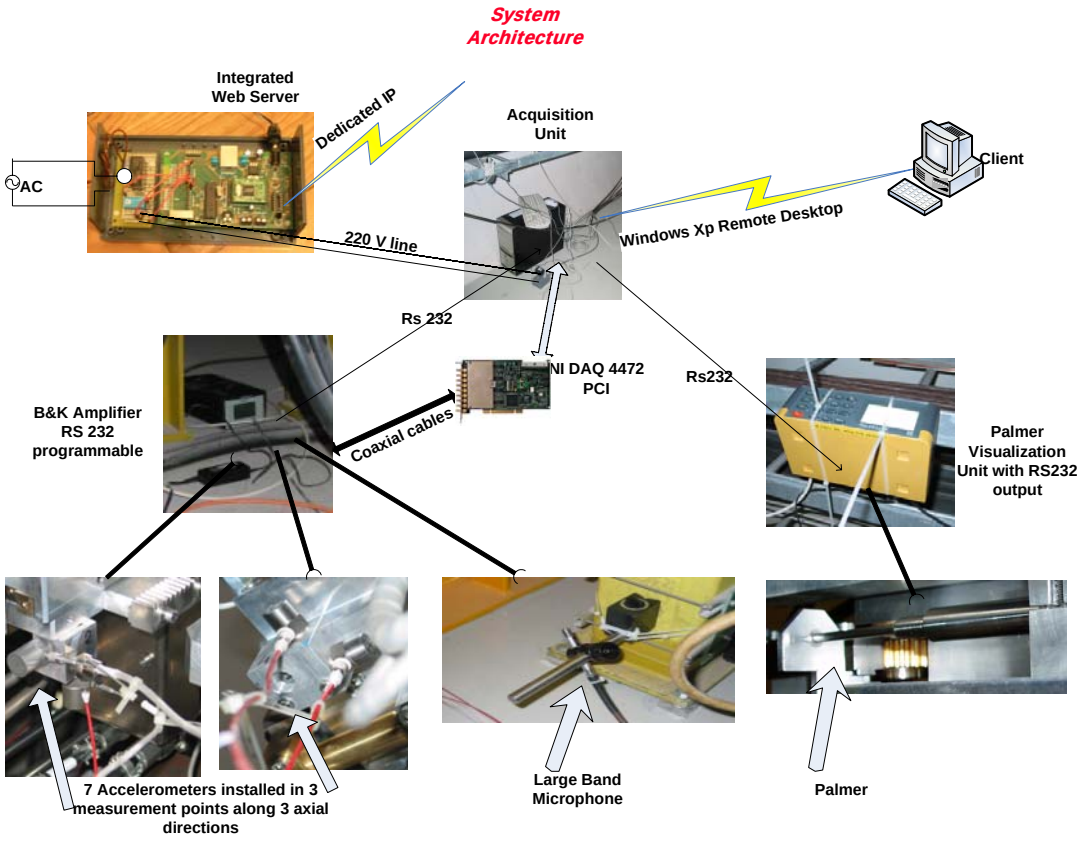

Fig. 3.20: architecture of the data acquisition system

3.1.3 Overview of software

Due to the radioactive environment, the data acquisition has to be performed in remote mode. For the control of the measurement system, an application has been developed in LabWindows 7.0. This software provides a graphical interface which allows:

- The control of the data acquisition
- The setting of the parameters of the data board.

A section of this software is dedicated to the NEXUS amplifier which is a device RS232 programmable. It is possible to set both the input and the output parameters of the preamplifier (gain, sensitivity, cut off frequency of the input filter), to monitor the status of the device, to perform a test to check if the accelerometer are well mounted.

This application allows performing a first analysis of the data also (plot of the data and FFT).

Independent software was developed for the control of the Display unit of the capacitive gauge, which is possible to programme by the RS232 standard. The chapter 5 is dedicated to the presentation of such applications.

3.1.4 Overview of other used sensors

The collimator is equipped with other instrumentation which will provide extensive diagnostics. There are sensor positions for each motor (point 1, point 2, point 3, point 4) to check the moving of the jaws; other sensors are dedicated to

- Measurement of collimator gap at both the extremity of the collimator tank to monitor the average gap and the angle between the two jaws.
- Independent measurement of one jaw at both the extremity.

There are 2 temperature sensors mounted onto both the extremity of the two jaws; various switches provide signals to indicate the critical positions of the jaw (in, out, anti-collision between the two jaws). Beam loss monitor (BLM) are installed close the collimator on both downstream and upstream side to measure the radiation level due to the proton beam; these sensors are used for the set up and the alignment of the collimator.

3.1.5 Measurement conditions

The main goal of the test in TT40 is to verify the robustness of the carbon jaw of the LHC secondary collimator. The left jaw of the TT40 prototype is made of fibre-reinforced graphite (C-C) and the right one is made of graphite (C). The collimator must be sufficiently robust to fulfil its task, that is, efficient cleaning of the beam halo during the full LHC beam cycle, without being damaged in both normal and abnormal operational conditions. For the robustness test, it was planned to hit the jaws of the collimator prototype with a 450 GeV proton beam at increasing intensity up to the maximum of 4 x 72 bunches (intensity around 4 x 10^{13} protons). This is the nominal intensity of a full LHC injection batch and corresponds to the maximum intensity beam that can hit the LHC collimator in case of injection failures.

The measurements have been performed in different conditions:

- Low proton beam intensity for the alignment operations of the collimators
- Bump into each jaw at the maximum proton beam intensity (4 x 72 bunches) for different transverse impact parameter
- Bump into each jaw at increasing proton beam intensity for a specific transverse impact parameter

- Bump into the TED (target 5 m distant from the collimator) at increasing proton beam intensity

The table below summarizes the conditions of the measurement at high intensity performed on the 8th November.

N° Acquisition	Time	Intensity	Description	Impact parameter
1	22:16	1x72 bunches 7.6 10^{12} #p	Left jaw	5 mm
2	22:21	1x72 bunches 7.8 10^{12} #p	Right jaw	5 mm
3	22:33	2x72 bunches 1.0 10^{13} #p	TED	-
4	22:51	2x72 bunches 1.6 10^{13} #p	Left jaw	5 mm
5	23:04	2x72 bunches 1.6 10^{13} #p	TED	-
6	23:26	2x72 bunches 1.4 10^{13} #p	Right jaw	5 mm
7	00:00	3x72 bunches 2.0 10^{13} #p	Left jaw	5 mm
8	00:06	4x72 bunches 2.6 10^{13} #p	TED	-
9	00:10	4x72 bunches 3.0 10^{13} #p	Left jaw	5 mm
10	00:15	4x72 bunches 3.0 10^{13} #p	Left jaw	4 mm
11	00:35	4x72 bunches 3.1 10^{13} #p	Left jaw	3 mm
12	00:40	4x72 bunches 2.7 10^{13} #p	Left jaw	2 mm
13	00:46	4x72 bunches 3.0 10^{13} #p	Left jaw	1 mm
14	00:49	4x72 bunches 3.1 10^{13} #p	Left jaw	6 mm
15	00:54	4x72 bunches 3.0 10^{13} #p	Right jaw	5 mm
16	00:57	4x72 bunches 3.1 10^{13} #p	Right jaw	4 mm
17	01:01	4x72 bunches 3.0 10^{13} #p	Right jaw	3 mm
18	01:07	4x72 bunches 2.9 10^{13} #p	Right jaw	2 mm
19	01:09	4x72 bunches 2.9 10^{13} #p	Right jaw	1 mm

Tab. 3.4: Description of the measurement conditions

It is noted that the measurement of the transverse impact parameter is not very precise; this is due to the technique of the beam based alignment which can not ensure a precise evaluation of the jaw in respect to the beam. During the tests it was not known with high precision the angle of the jaws too.

3.2 The piezoelectric accelerometers

3.2.1 Principle of functioning

The piezoelectric accelerometer presents these main properties:

1. Usable over very wide frequency range
2. Excellent linearity over a very wide dynamic range
3. Vibration measurements are possible in a wide range of environmental conditions

Because of these features, for our application, the piezoelectric accelerometer is preferred to other vibration transducer as geophones, position potentiometer or piezoresistive transducer.

A piezoelectric material develops an electrical charge when subjected to a force. The domains within the molecular structure of the material become aligned in such way that an external force causes deformations of the domains and charges of opposite polarity to form on opposite ends of the material. Fig 3.21 shows a simplified illustration of this effect. When a piezoelectric accelerometer vibrates, forces proportional to the applied acceleration act on the piezoelectric elements and the charge generated by them is picked up by the contact. It is the extremely linear relationship between the applied force and the developed charge which results in the excellent characteristics of this sensor. The sensitivity of this accelerometer is given in pC/g or in pC/ms^{-2} ($g = 9.8\ ms^{-2}$ is acceleration of gravity).

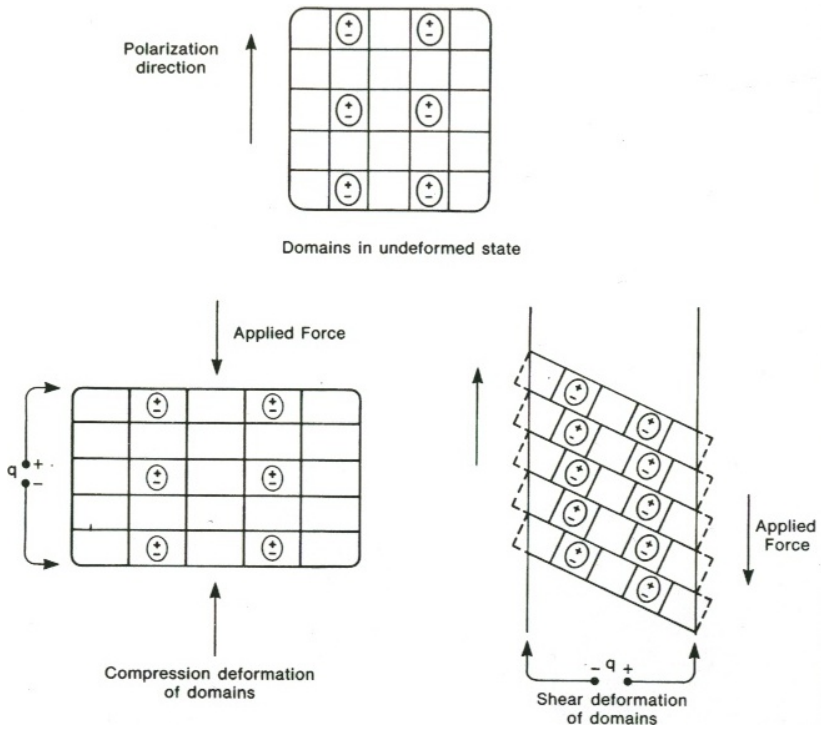

Fig 3.21: Simple model of the piezoelectric effect

3.2.2 Analytical treatment of accelerometer operation

Fig. 3.22 shows a scheme of the accelerometer; the two masses, m_b and m_s are unsupported and connected by an ideal spring.

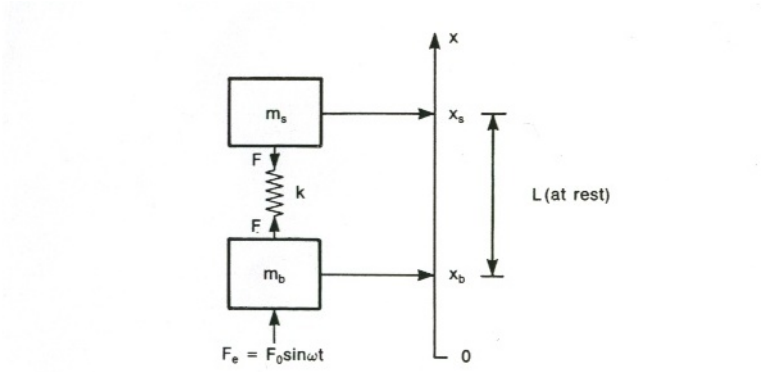

Fig 3.22: Simplified model of an accelerometer

The following expressions describes the forces present in the model

$$F = k(x_s - x_b - L) \quad \text{(Eq. 3.1)}$$

$$m_b x_b = F + F_e \quad \text{(Eq. 3.2)}$$

$$m_s \ddot{x}_s = -F \quad \text{(Eq. 3.3)}$$

$$\ddot{x}_s - \ddot{x}_b = -\frac{F}{m_s} - \frac{F + F_e}{m_b} \quad \text{(Eq. 3.4)}$$

$$r = x_s - x_b - L \quad \text{(Eq. 3.5)}$$

$$\frac{1}{\mu} = \frac{1}{m_s} + \frac{1}{m_b} \quad \text{(Eq. 3.6)}$$

$$\mu \ddot{r} = -kr - \frac{Fe}{m_b}\mu \quad \text{(Eq. 3.7)}$$

Here m_s is the seismic mass, m_b is the mass of the accelerometer base, k is the equivalent stiffness of the piezoelectric elements, r is the relative displacement of the seismic mass to the base and μ is often referred to as the "reduced mass". When the accelerometer is in a free hanging position and is not being excited by external force the equation of the motion becomes

$$\mu\ddot{r} = -kr \qquad \text{(Eq. 3.8)}$$

Assuming that the displacement r varies harmonically with an amplitude R

$$r = R\sin(\omega t) \qquad \text{(Eq. 3.9)}$$

$$-\mu R\omega^2 \sin(\omega t) = -kR\sin(\omega t) \qquad \text{(Eq.3.10)}$$

And therefore the resonance frequency, ω_n, is

$$\omega_n^2 = \frac{k}{\mu} = k(\frac{1}{m_b} + \frac{1}{m_s}) \qquad \text{(Eq. 3.11)}$$

If the accelerometer is now mounted with perfect rigidity onto a structure which heavier than the total weight of the accelerometer then m_b becomes much larger than m_s; the last equation becomes:

$$\omega_m^2 = \frac{k}{m_s} \qquad \text{(Eq. 3.12)}$$

This is the natural frequency of the seismic mass-spring system is defined as the mounted resonance frequency of the accelerometer.

If the differential equation is solved considering the external force F_e, the frequency response of the accelerometer results

$$A = \frac{1}{1 - \left(\frac{\omega}{\omega_n}\right)^2} \qquad \text{(Eq. 3.13)}$$

This result shows that the displacement between the base and the seismic mass increases when the forcing frequency becomes comparable with the natural resonance frequency of the accelerometer. Consequently the force on the piezoelectric elements and the output from the accelerometer also increase.

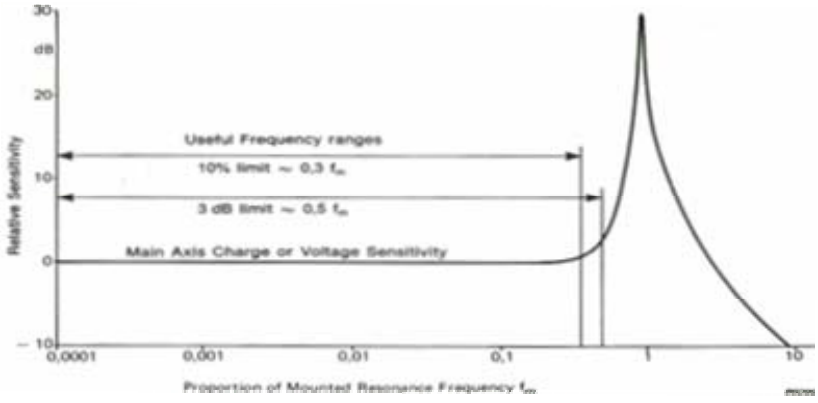

Fig. 3.23: Frequency response

The Fig. 3.23 shows that the mounted resonance frequency determines the frequency range over which the accelerometer can be used; the higher the mounted resonance frequency, the wider the operating frequency range. About lower frequency limit, piezoelectric accelerometers are not capable of a true DC response. The piezoelectric elements will only produce a charge when acted upon by dynamic forces. The low frequency limit is determined by the amplifier to which the accelerometer is connected as it is the preamplifier which determines the rate at which the charge leaks away from the accelerometer.

3.2.3 Accelerometer Sensitivity

The accelerometer is a device whose electrical output is proportional to the applied force; accelerometer sensitivity expresses the relationship between the input (acceleration) and output (charge or voltage). The piezoelectric accelerometer can be regarded as either a charge source or a voltage source. The piezoelectric element acts as a capacitor C_a in parallel with a very high internal leakage resistance, R_a, which, for practical purposes, can be ignored. It may be treated either as an ideal charge source, Q_a in parallel with C_a and the cable capacitance C_c or as an ideal voltage source V_a in series with C_a and loaded by C_c as shown in Fig. 3.24.

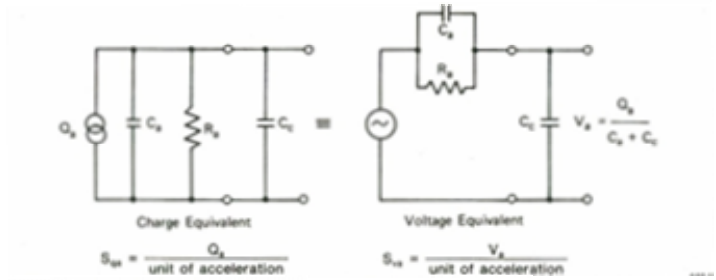

Fig 3.24: Equivalent electrical circuit for piezoelectric accelerometer and connection cable

The choice of accelerometer preamplifier depends on whether we want to detect charge or voltage as the electrical output from the accelerometer. The voltage produced by the accelerometer is divided between C_a and C_c; hence a change in the cable capacitance or a change in the length of the cable will cause a change in the voltage sensitivity. This is the major disadvantage that leads to prefer charge amplifier to voltage amplifier.

3.2.4 Transient response

We are interested in particular in the transient behaviour of the accelerometers due to the kind of measurement that will be performed for the robustness test of the collimator.

Piezoelectric accelerometers are extremely linear transducers and can reproduce a wide range of transients without problems. More often it is the preamplifier and any associate filter which cause the distortion of the signal; however, to ensure the accuracy of the measurement it is necessary to consider the following transient phenomena.

Leakage effects

This distortion is caused by the accelerometer and amplifier combination operating in the incorrect frequency range. When the accelerometer is subjected to a quasi-static acceleration a charge is developed on the piezoelectric elements; this charge is stored by the capacitor and prevented from "leaking away" by the very high leakage resistance. However, due to the finite leakage time constant of the accelerometer and the input impedance and lower limit frequency of the amplifier, some charge leaks away and all this results in a negative slope waveform; when the acceleration stops, the charge changes a corresponding amount and drops below the zero level before rising up to the zero level again. This effect causes errors in the measurement of the peak amplitude of the acceleration.

Ringing

This term is used to describe the distortion produced by an accelerometer which is being used to measure transient vibrations outside its useful frequency range (see Fig 3.25). The resonance of the accelerometer is excited with high frequency components and this should be avoided. The accelerometer resonance can be damped to reduce the ringing. This can be achieved using a mechanical filter for mounting the accelerometer or by applying the accelerometer signal to a low pass filter incorporated in the amplifier.

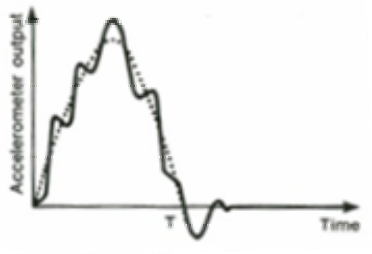

Fig. 3.25: Waveform distortion due to the ring

Zero shift

If the force on the piezoelectric element causes a transient vibration whose amplitude is very close to the maximum acceleration limit the zero shift phenomenon can occur. The piezoelectric elements are not perfectly elastic materials, then when the force is suddenly decreased the molecular domains may not all return to the state they were in before the shear fore was applied. Therefore, when the force is removed, the elements still produce a charge which slowly decays with time as the amplifier output returns to zero at a rate determined by the lower limit frequency. This phenomenon occurs seldom and with random sign.

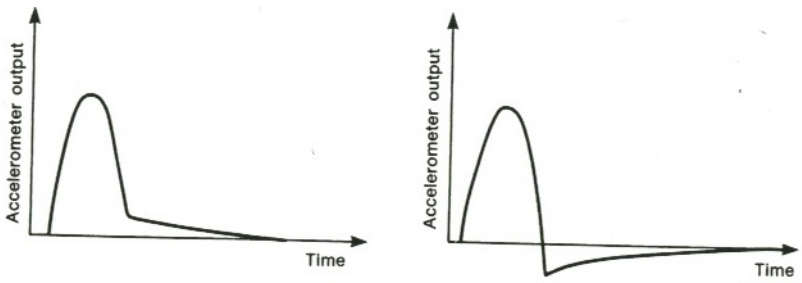

Fig. 3.26: Accelerometer and preamplifier output resulting from a half-sine pulse of such high level that "zero shift" has been introduced

3.3 Microphone

Every measurement grade microphone, regardless if it is classified as a free field, random incidence (diffuse), or pressure microphone, is fundamentally a pressure response microphone, where the dimension of the microphone is significant relative to the wavelength of sound. When sound waves arrive at the microphone head-on (0° incidence), the average sound pressure across the microphone diaphragm is amplified because the microphone changes the sound field as it diffracts and reflects the sound waves. The amount of amplification varies according to the physical dimensions of each individual microphone and the angle of incidence of the sound waves to the microphone. This amplification can result in significant error. For example if a 1/2 in. "pressure" response microphone with a flat pressure response up to 20 kHz is pointed directly at a 20 kHz noise source, the pressure across its diaphragm will be 10 dB higher than the actual pressure that would have existed if the microphone was not present (Fig. 3.27). The output of the microphone would then read 10 dB higher than the actual pressure.

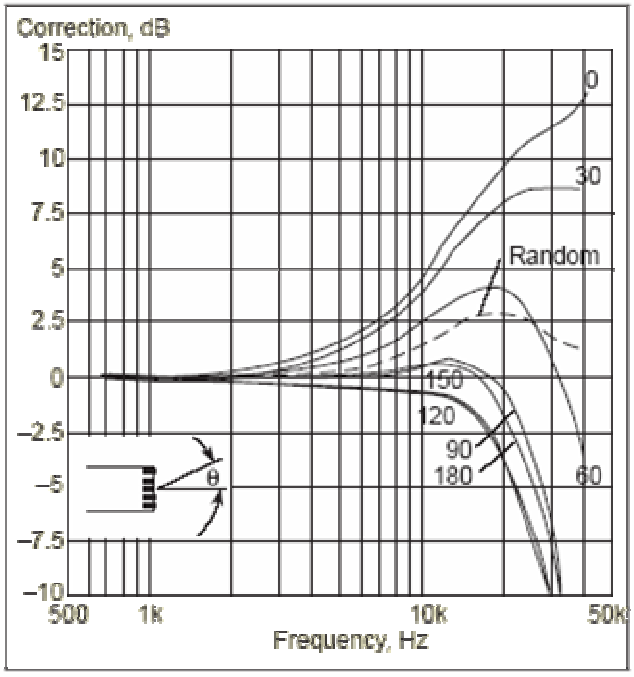

Fig. 3.27:Signal amplification as a function of the angle incidence

This leads us to the "free field" response microphone type. The "free field" response microphone is simply a pressure response microphone whose high frequency response is carefully rolled off to cancel out the pressure amplification that occurs with a 0° incidence sound wave. A "free field" response measurement microphone is supplied with a calibration

chart that has two curves on it, (see Fig. 3.28). The curve that attenuates at a fairly low frequency is the actual measured pressure response of the microphone and the curve that is flatter to a higher frequency is the calculated response of that microphone to 0° incidence sound in a “free field.”

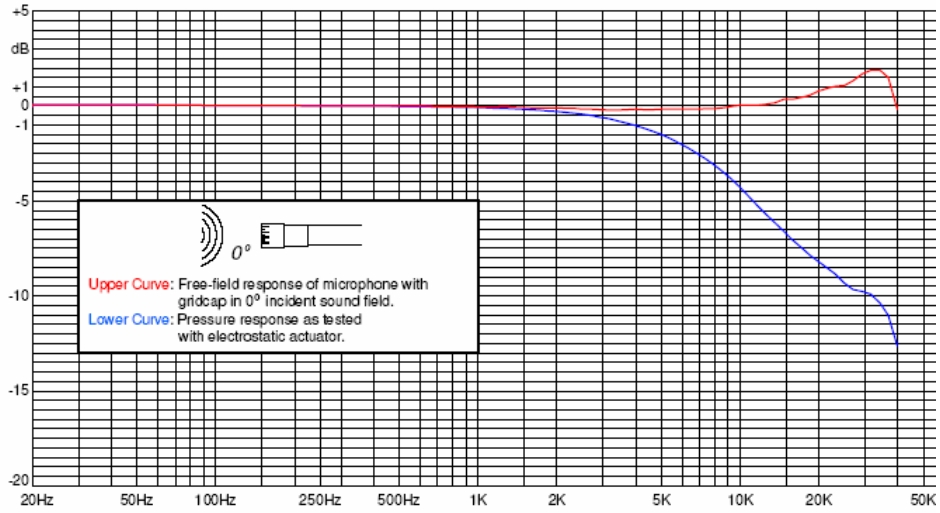

Fig. 3.28: Frequency response of the microphone

The B&K 4189 is a condenser microphone. Condenser (or capacitor) microphones use a lightweight membrane and a fixed plate that act as opposite sides of a capacitor. Sound pressure against this thin polymer film causes it to move. This movement changes the capacitance of the circuit, creating a changing electrical output. In many respects a condenser microphone functions in the same manner as an electrostatic tweeter, although on a much smaller scale and "in reverse." Condenser microphones are preferred for their very uniform frequency response and ability to respond with clarity to transient sounds. The low mass of the membrane diaphragm permits extended high-frequency response, while the nature of the design also ensures outstanding low-frequency pickup. The resulting sound is natural, clean and clear, with excellent transparency and detail. Condenser elements have two other design advantages that make them the ideal (or the only) choice for many applications: they weigh much less than dynamic elements and they can be much smaller. These characteristics make them the logical choice for line – or "shotgun" - microphones, lavaliers and miniature microphones of all types. The microphone is connected to the DeltaTron Microphone Preamplifier Type 2671 which enables to make acoustical measurements with a DeltaTron input module. The preamplifier’s low output impedance allows problem-free use of long extension cables. DeltaTron is a generic name for accelerometers and signal conditioning products from Brüel&Kjær. It identifies products that operate on a constant-current power

supply and give output signals in the form of voltage modulation on the power supply line. One of the advantages of this system is that it allows you to use inexpensive BNC coaxial cables. The preamplifier converts the DeltaTron or ICP constant current line drive (CCLD) supply, which must be between 2 and 20 mA (nominal 4mA), into a constant 12 V DC level. The output signal from the microphone swings around this DC level.

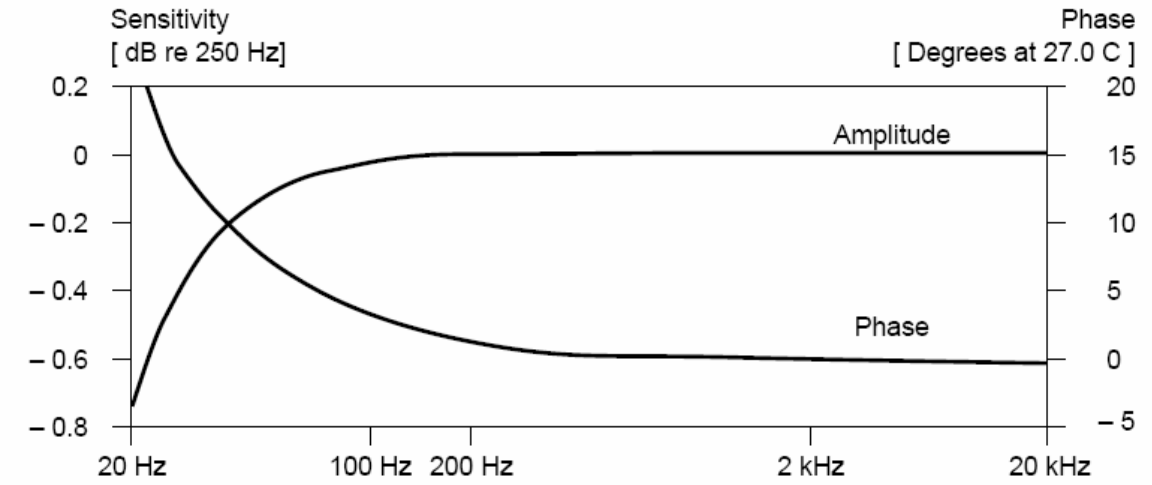

Fig. 3.29: Frequency response of the preamplifier 2671

3.4 Vibration preamplifiers

As described above, a NEXUS conditioning amplifier was used for the B&K accelerometers and the microphone; four line-drive amplifiers were used for the AP accelerometers. Vibration preamplifiers perform the essential role of converting the high impedance output of the piezoelectric accelerometer into a low impedance signal suitable to measuring and analyzing instrumentation.

The NEXUS conditioning a preamplifier can also perform the following roles:

1. Matching measuring instrumentation input sensitivity to that of the accelerometer output
2. Amplification of the vibration signal to obtain the desired overall system sensitivity.
3. Warning of overload at both the input and output to obtain the desired overall system sensitivity.
4. Low and high frequency filtering to reject unwanted signals.
5. Independent system to test if the accelerometer is well mounted on the basis support.

6. Setting of both input and output of the amplifier to float mode or single-ended-mode.
7. Remote control by RS 232.

In the tab. 3.5 are resumed the main features of the NEXUS preamplifier:

INPUT GROUNDING:	Single-ended or floating
MAX. INPUT Differential Charge	100 nC (peak)
INPUT PROTECTION: Differential Charge	300 nC (peak)
ACCEPTABLE TRANSDUCER SENSITIVITY RANGE	10^{-19} to 10^{-6}C/MU (MU = mechanical units: m/s2; g, N, lb., Pa)
LOW-PASS FILTER (–10%):	0.1, 1, 3, 10, 22.4, 30 or 100 kHz, attenuation slope 40 dB/decade
HIGH-PASS FILTER (–10%)	0.1, 1.0 or 20 Hz
OUTPUT GROUNDING	Single-ended or floating
MAX. OUTPUT (differential voltage):	10Vpeak (20V peak to peak)

Tab. 3.5: Features of the NEXUS preamplifier

In-line charge converter Type AP5000/10

Specifications:

Gain:	10 mV/pC Also available: AP5000/1 with 1mV/Pc AP5000/100 with 100 mV/pC
Dynamic range:	>120 dB
Frequency range:	0,1 Hz to 200 kHz (-3dB) Optional version for frequencies down to 0.016 Hz
Max. output	-5V to +5V (DC offset: 10 Volt nominal)
Transducer-capacity:	10pF to 10nF
Output noise:	< 10µVolt (0.6Hz to 10kHz)
Temperature range:	-25°C to +100°C
Power supply:	2-4 mA constant current, 10-30 Volt DC
Dimensions:	13 mm round 62 mm long (w.o. connectors)
Housing	Hermetically sealed stainless steel housing
Weight:	42 gram

Tab. 3.6: Characteristics of the line-drive AP5000

In the next paragraph the main features and the working principle of the amplifiers are described.

3.4.1 Charge amplifier

There are two basic types of preamplifiers which may be used with piezoelectric accelerometer.

1. Charge amplifier. It produces an output voltage proportional to the input charge. It does not amplify the charge.
2. Voltage amplifiers. It produces an output voltage proportional to the input voltage.
3. Line-drive preamplifier.

Charge amplifiers are generally used in preference to the voltage amplifiers. The distinct advantage of charge amplifier is that both very short and long cables can be used without changing the overall sensitivity of the system. However, the voltage amplifier requires a recalibration of the system sensitivity if a change in cable length will necessitate.

AP amplifiers and NEXUS amplifier operate both a charge conversion and in particular AP devices are line-drive systems.

They are miniature devices containing only the front end of a conventional amplifier in a form which is connected near to the accelerometer by special cables. They are fixed gain devices with no controls. The power for a line-drive system must be derived from an external DC supply through the coaxial cable for the transmission of the signal from the amplifier to the data acquisition system.

A charge amplifier uses an operational amplifier input stage. The configuration of the operational amplifier with the capacitor in the feed-back loop operates as an integration network and integrates the current at the input. This input current is the result of the charge developed across the high impedance piezoelectric elements inside the accelerometer. The amplifier works to nullify this current and in doing so produces an output voltage proportional to the charge.

Charge Sensitivity

The voltage output of a charge amplifier is the proportional to the charge at the input and therefore to the acceleration of the accelerometer. The gain is controlled by the feedback capacitance across the operational amplifier. The Fig. 3.30 shows an equivalent circuit for a piezoelectric accelerometer connected to a charge amplifier.

Q_a: charge generated by the piezoelectric elements (proportional to the applied acceleration)
C_a: capacitance of the accelerometer
R_a: resistance of the accelerometer

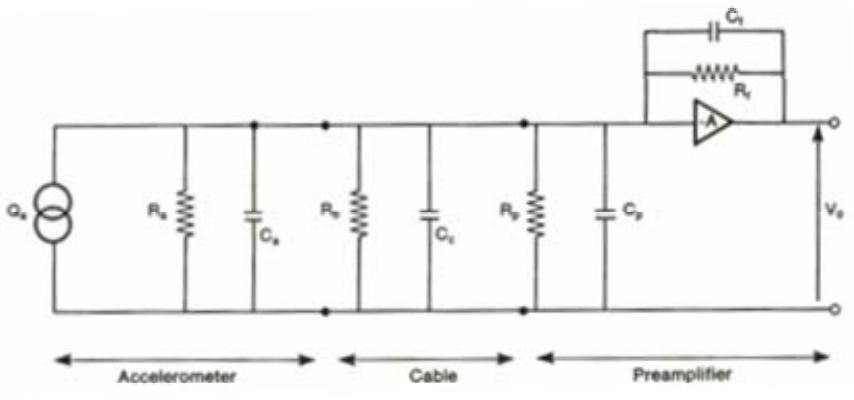

Fig. 3.30: Equivalent circuit for piezoelectric accelerometer

C_c: capacitance of cable and connectors

R_b: resistance between cable screen and centre conductor

C_p: capacitance of preamplifier input

R_p: resistance of preamplifier input

C_f: feedback capacitance

R_f: feedback resistance

A: gain of operational amplifier

V_o: voltage output of the preamplifier

Normally the resistances of the accelerometer, preamplifier input and feedback path are very high so the circuit can be reduced to the one shown in Fig. 3.31 where C_t is the total capacitance.

Considering an ideal amplifier, by analysing this circuit, we have:

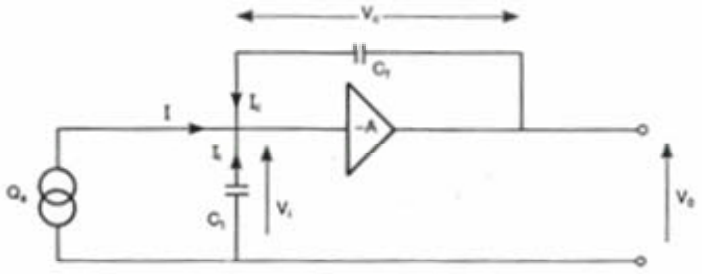

Fig. 3.31: Equivalent circuit without resistances

$$V_o = -AV_i \qquad \text{(Eq. 3.14)}$$

$$V_c = V_o - V_i = V_o - \frac{V_o}{-A} = \left(1 + \frac{1}{A}\right) V_o \qquad \text{(Eq. 3.15)}$$

$$I + I_i + I_c = 0 \qquad \text{(Eq. 3.16)}$$

$$I = \frac{dQ_a}{dt} \qquad \text{(Eq. 3.17)}$$

$$I_c = C_f \frac{dV_c}{dt} = \left(1 + \frac{1}{A}\right) C_f \frac{dV_o}{dt} \qquad \text{(Eq. 3.18)}$$

$$I_i = -C_t \frac{dV_i}{dt} = \frac{1}{A} C_t \frac{dV_o}{dt} \qquad \text{(Eq. 3.19)}$$

$$\frac{dQ_a}{dt} = -\left(1 + \frac{1}{A}\right) C_f \frac{dV_o}{dt} - \frac{1}{A} C_t \frac{dV_o}{dt} \qquad \text{(Eq. 3.20)}$$

This equation can be solved by integration: constants corresponding to any DC offset voltage initially present at the amplifier output are assumed to be zero. Such offsets will disappear rapidly as the amplifier is in use. The solution to the equation then becomes:

$$V_o = -\frac{Q_a}{\left(1 + \frac{1}{A}\right) C_f + \frac{1}{A} C_t} \qquad \text{(Eq. 3.21)}$$

If we consider that the magnitude A is normally 10^5 the solution can be reduced to the simple expression:

$$V_o = -\frac{Q_a}{C_f} \qquad \text{(Eq. 3.22)}$$

It is clear from this that the output voltage is proportional to the input charge and therefore to the acceleration of the accelerometer; the gain of the preamplifier is determined by the feedback capacitance. With the hypothesis of ideal amplifier and high gain A, the input voltage V_i is zero and the input capacitance has no effects on the resulting output voltage. Consequently the finite input resistance does not influence the output; this means that all the charge from the accelerometer flows to the feedback capacitor.

Considering the resistance R_a, R_b, R_p and R_f we have to analyse the following circuit

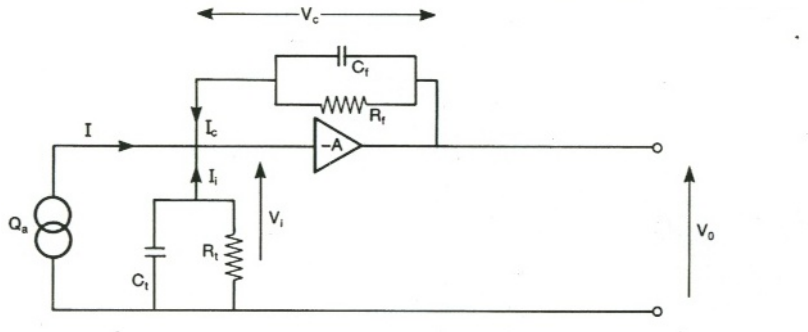

Fig 3.32: Equivalent circuit with the resistances R_a, R_b, R_p and R_f

where

$$\frac{1}{R_t} = \frac{1}{R_a} + \frac{1}{R_b} + \frac{1}{R_p} \qquad \text{(Eq. 3.23)}$$

By a similar analyse to the one showed above we obtain:

$$\frac{dQ_a}{dt} = -\left(1 + \frac{1}{A}\right)\left[C_f \frac{dV_o}{dt} + \frac{V_o}{R_f}\right] - \frac{1}{A}\left[C_t \frac{dV_o}{dt} + \frac{V_o}{R_t}\right] \qquad \text{(Eq. 3.24)}$$

Assuming that the voltage and current vary harmonically and that both R_t and A are very large the solution is

$$V_o = -\frac{Q_a}{C_f\left(1 + \frac{1}{j\omega R_f C_f}\right)} \qquad \text{(Eq. 3.25)}$$

Hence, with Q_a being proportional to the acceleration of the accelerometer, the overall sensitivity of the accelerometer-amplifier combination can be controlled by C_f.

Lower Frequency response

The low frequency response of a charge amplifier is determined by the time constant set by the feedback path around the operational amplifier and is unaffected by changes in the input load conditions as showed in the last equation.

Accelerometers are self-generating devices and therefore have no true DC response. A static force does not provide any input power. A constant force causes a charge that is stored on the capacitance; the storage charge leaks away and the voltage drops exponentially at a rate determinate by the time constant of the system. If R_f is large, the time constant is high and the DC response is better

Noise in charge amplifier

A model of the internal noise sources of an operational amplifier is shown in Fig. 3.33

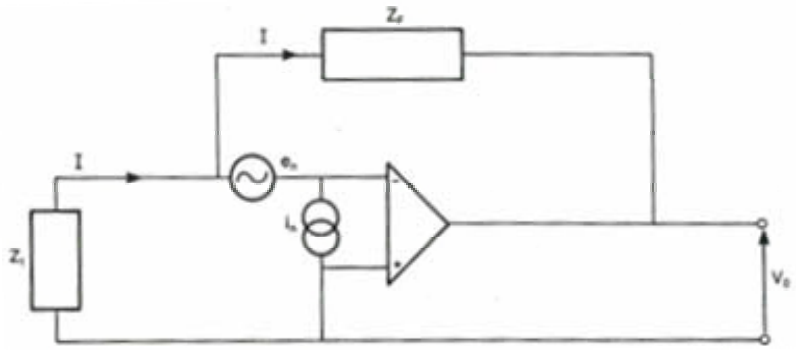

Fig. 3.33: Model of the internal noise sources

Z_t: equivalent impedance of the accelerometer

Z_f: equivalent impedance in the feedback path

e_n: noise voltage

i_n: noise current

V_o: output voltage

In the high impedance case of the piezoelectric source and mainly capacitive feedback the current noise is negligible; with the hypothesis of the virtual ground and no current flowing at the inverting input of the operational amplifier the analyse of the circuit shows:

$$I = \frac{-e_n}{Z_t} = \frac{e_n - V_o}{Z_f} \qquad \text{(Eq. 3.26)}$$

$$V_o = e_n\left(1 + \frac{Z_f}{Z_t}\right) \qquad \text{(Eq. 3.27)}$$

To convert this into an expression for the signal at the source it must be divided by the amplification factor:

$$e_s = -V_o \frac{Z_t}{Z_f} = -e_n \left(1 + \frac{Z_t}{Z_f} \right) \qquad \text{(Eq. 3.28)}$$

In the mid-frequency range the impedance at both the source and at the output are mainly capacitive so:

$$e_s = -e_n \left(1 + \frac{C_f}{C_t} \right) \qquad \text{(Eq. 3.29)}$$

The noise voltage e_s can be converted into an equivalent charge noise, q_t:

$$q_t = e_s \cdot C_t = -e_n \left(C_t + C_f \right) \qquad \text{(Eq. 3.30)}$$

From this it is seen that although the sensitivity and low limit frequency is not changed significantly by capacitive or resistive loading of the input the charge noise increases as C_t and C_f increase.

As C_f determines the gain of the preamplifier there will be higher noise at lower gain settings which require a higher feedback capacitance.

External noise

In the following analysis the noise at the input is assumed to be caused by the combination of two effects:

1. Triboelectric noise: All cables from the accelerometers to the preamplifier can generate a charge if their mechanical movement is not restricted or if they are not well mounted.
2. Ground loops: In large machines there is always the possibility the machinery housing may not be at the earth potential. Consequently the accelerometer case and the cable screen will not be at the same potential and a voltage drop will exist along the cable.
3. Electromagnetic interference (EMI): A typical situation, that may present the phenomenon EMI, is power lines running alongside signal lines over long distances.

The most important effect is the ground-loops that we analyze in more detail for different accelerometer-preamplifier configurations.

The Fig. 3.34 shows a grounded accelerometer and a charge amplifier combination in which the charge and voltage noise sources have been introduced and they are considered independent.

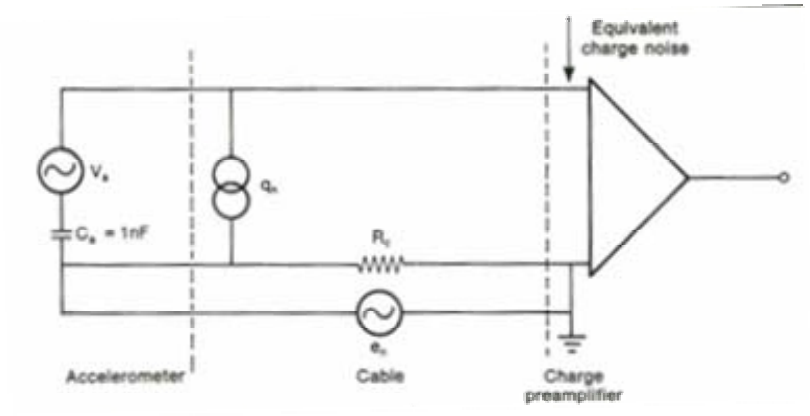

Fig. 3.34: Simplified equivalent circuit of normal grounded accelerometer connected to a normal grounded input charge amplifier

In this case the ground loop noise is the product of the noise voltage and the accelerometer capacitance: $e_n * C_a$.

The Fig. 3.35 shows a grounded accelerometer with a charge amplifier with floating input

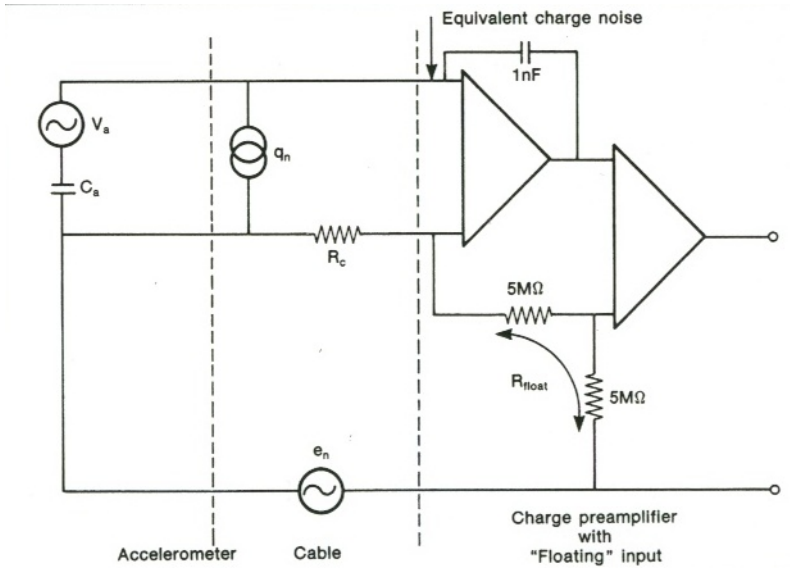

Fig. 3.35: Simplified equivalent circuit of normal grounded accelerometer connected to a charge amplifier with a floating point

The calculation of the ground loop noise involves the use of the common Mode rejection Ratio (CMRR) of the second operational amplifier:

$$C_a \frac{R_c}{R_{float} + R_c} \cdot e_n + \frac{CMRR}{1mv / pC} \cdot \frac{R_{float}}{R_{float} + R_c} e_n \qquad \text{(Eq. 3.31)}$$

Considering a typical value of CMRR (70 dB) and that R_c is about $0.05\ \Omega/m$ the ground loop noise is three time less than previous combination.

If the accelerometer is electrically insulated from the surface onto which is mounted, improvements in the ground loop noise can be obtained if the configuration with single ended input is used.

On the basis of the evaluations presented above about the external noise ground-loop, the following settings of the input and output mode have been chosen for the B&K accelerometers-preamplifier combination.

	Model	Type case	Input mode	Output mode
Accelerometer 1	B&K 2273AM	Insulated	Single mode	Floating
Accelerometer 2	B&K 2273A	Not insulated	Floating	Floating
Accelerometer 3	B&K 2273A	Not insulated	Floating	Floating

Tab. 3.7: Input and output configuration mode

3.5 Palmer

As described above, the position sensor is a Sylvac palmer which consists of a capacitive probe P50 and a display unit D90. The main advantage that this sensor provides is no active electronic is installed in the pick up sensor. This in prncipe ensures a correct functioning in a radioactive environment; the company could not guarantee the radiation hardness because tests were never performed.

The D90 unit displays the absolute displacement of the long-travel probe P50; highest resolution is 0.1 μm. It can also perform these integrated functions:

- Choice of the unit (mm or inch) and direct conversion mm/inch
- Choice of the resolution (0.1 mm to 0.0001 mm)
- Three measuring mode (continuous value, max value or min value)
- Introduction of a preset value.
- RS232 remote control of the commands

It is noted that he D90 acquisition box is not suitable for continuous data storage. This was carried out by the contr5ol remote software as described in the section 5.4.

In the Tab. 3.7 is shown the characteristics of measurement system D90+P50:

	D90	P50	Mean error
Accuracy	3µm	4µm	5µm
Repeatability	-	0.4µm	-
Total range	-	52.2mm	-
Zero shift	-	0.01µm	-

Tab. 3.8

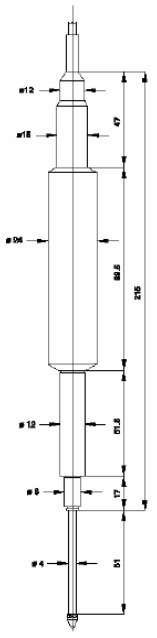

Fig. 3.36: Probe Dimension

Working principle

The simplest configuration of a capacitive position sensor is two close-spaced parallel plates. The capacitance of the sensor is proportional to the area of the electrodes and the dielectric constant, and inversely related to the space between the parallel plates. Therefore, capacitive sensors can be used for direct measurements of motion/distance.

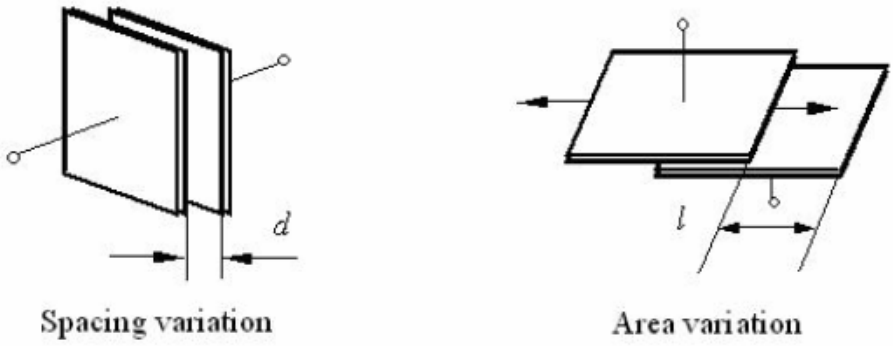

Fig. 3.37: Capacitive position/displacement sensors with two variations

The spacing variation of parallel plates is suitable for motion detection if the spacing change is less than the electrode size. The capacitance is inversely related to the space in this case. When displacement increases to the dimension of the electrodes, measurement accuracy of the spacing variation suffers from vanishing signal level. The area variation is then preferred. As the plates slide transversely, the capacitance of the area variation changes linearly with motion. The pick up sensors Sylvac is based on the measurement of the area variation and the plates present a cylindrical geometry. Using an Impedance-Voltage Converter (Fig. 3.38), the capacitance change can be converted into a voltage change for further signal processing.

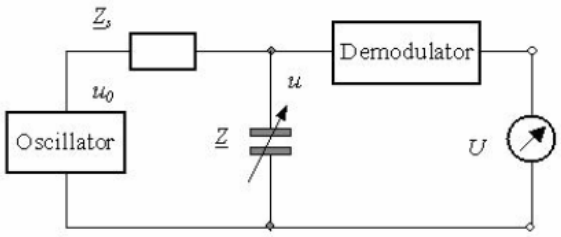

Fig. 3.38: Impedance-Voltage converter working nearby resonance frequency

Capacitive sensors should be excited by a high-oscillation frequency nearby the resonance frequency of the circuit so that electrode impedance is as low as possible and the sensitivity to displacement reaches the maximum. The resonance frequency of an impedance-voltage converter for capacitance sensors depends on the geometric sensor parameters and the serial impedance *Zs*. The serial impedance must be high enough in order to obtain a high sensitivity. The resonance frequency is determined by measuring the maximum output signal under using maximum space. After demodulating the output voltage *u* one obtains the output voltage *U* as function of the distance.

4 DATA ACQUISITION BOARD

The data acquisition board NI 4472 has been chosen because it is compatible with the output signals from the accelerometers and the microphone. This choice is due to the following considerations:

- Frequency range of the signals.
- Amplitude level of the signals.

The frequency response of the accelerometers is flat up to 7 kHz and the %deviation is acceptable up to approximately 20 kHz (see Fig.3.10). The B&K microphone has a range frequency from 6 Hz to 20 kHz (see Fig. 3.27); on the basis of these considerations a minimum sampling frequency of 40 kHz is required.

The amplitude level of the vibrations induced by the beam proton impact was not yet studied because there was no time to perform precise numerical estimates of the expected amplitude level of the accelerometer signal. Thanks to the remote control of the NEXUS preamplifier, the output sensitivity of the B&K accelerometers and of the microphone can be changed over a wide ranges from *100 μV/unit* up to *31.6 V/unit* (unit is ms^{-2} for the accelerometers and *Pa* for the microphone). For the AP accelerometers the output sensitivity is fixed and it is around 20 mV/ms^{-2} for that AP 40 and around 10 mV/ms^{-2} for the AP37. The data acquisition board has to ensure a very high resolution to avoid that the quantization noise is comparable with the signal level if the output sensitivity is set to a low value.

NI 4472 satisfies both these requirements because it presents 8 analog input channels which are simultaneously sampled at a maximum rate of 102.4 kS/s with 24-bit resolution.

In addition this board has an independent 4 mA current source for each input channel by which it is possible to polarize the 4 AP preamplifiers. The analog input circuitry uses oversampling delta-sigma modulating analog-to-digital converters which exhibit a good differential and integral linearity due to the linearity of the 1 bit quantizer and DAC circuit in the feedback path. Its principle working is shown in the following paragraph. The following table shows the main featues of the data board NI 4472 which will be described in more detail in the paragraph 4.2.

N° channels	8- simultaneously sampled
Sampling rate	102.4 kS/s down to 1.0 kS/s
ADC type	Sigma-delta converter
ADC modulator oversample rate	64 f_s for 51.2kS/s<fs≤102.4kS/s 128fs for 1.0 kS/s≤fs≤51.2kS/s
Idle channel noise	110 dB min 1.0 kS/s≤fs≤51.2kS/s 105 dB min for 51.2kS/s<fs≤102.4kS/s
Resolution	24 bit
Input Range	±10 Volt
Input Configuration	Pseudo-differential
Input Coupling	AC or DC software selectable
Input current source	0 or 4 mA each channel independently software-selectable

Tab. 4.1: Technical specifications of the data board NI 4472

4.1 Sigma-Delta Converter

The sigma-delta converter is composed by an analog side and a digital side.

The analog side of a sigma-delta converter (a 1-bit ADC) is very simple. The digital side, performs filtering and decimation. Its working is based on the concepts of oversampling, noise shaping, digital filtering, and decimation.

4.1.1 Oversampling

First, consider the frequency-domain transfer function of a traditional multi-bit ADC with a sine-wave input signal whose amplitude is wide to stress all the codes. This input is sampled at a frequency F_s. According to Nyquist theory, F_s must be at least twice the bandwidth of the input signal.

When observing the result of an FFT analysis on the digital output, we see a single tone and lots of random noise extending from DC to $F_s/2$ (Figure 4.1). Known as quantization noise, this effect results from the following consideration: the ADC input is a continuous signal with an infinite number of possible states, but the digital output is a discrete function

whose number of different states is determined by the converter's resolution. So, the conversion from analog to digital loses some information and introduces some distortion into the signal. The magnitude of this error is random, with values up to ±LSB. The quantization noise power is given by the following equation:

$$e^2{}_{RMS} = \frac{1}{q}\int_{-\frac{q}{2}}^{\frac{q}{2}} e^2 de = \frac{q^2}{12} \qquad \text{(Eq. 4.1)}$$

where q is $FS/2^N$.

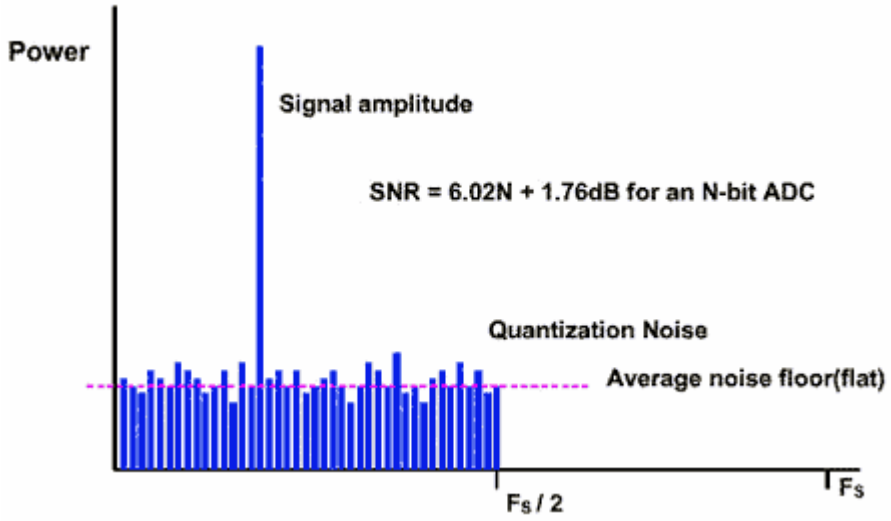

Fig 4.1: FFT diagram of a multi-bit ADC with a sampling frequency FS

If we divide the fundamental amplitude by the RMS sum of all the frequencies representing noise, we obtain the signal to noise ratio (SNR).

$$SNR = \frac{\frac{FS}{2\sqrt{2}}}{\frac{FS}{2^N\sqrt{12}}} = 2^N \frac{\sqrt{6}}{2} \qquad \text{(Eq.4.2)}$$

$$SNR_{dB} = 20\log\left(\frac{\frac{FS}{2\sqrt{2}}}{\frac{FS}{2^N\sqrt{12}}}\right) = 10\log 4^N + 10\log\left(\frac{3}{2}\right) = 6.02N + 1.76 \qquad \text{(Eq. 4.3)}$$

Consider again the above example, but with a sampling frequency increased by the oversampling ratio k, to kF_s. SNR is the same as before, but the noise energy has been spread over a wider frequency range. Sigma-delta converters exploit this effect by following the 1-bit ADC with a digital filter (Figure 4.2).

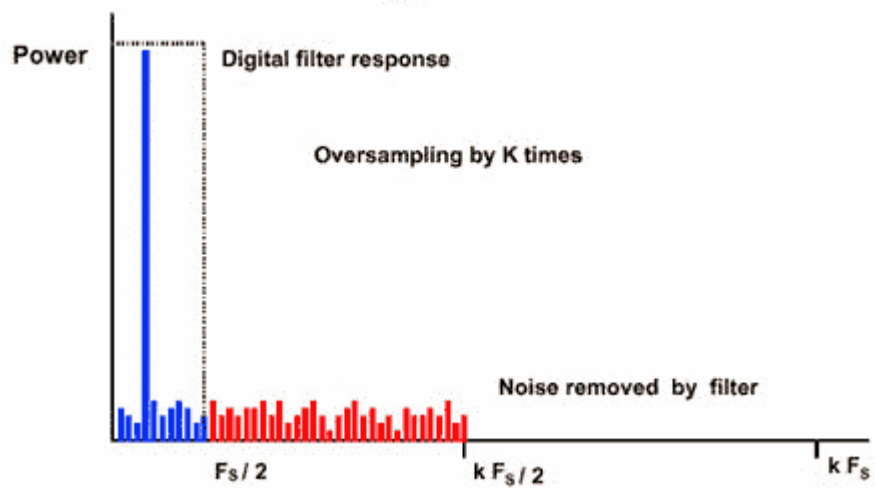

Fig. 4.2: Effect of the digital filter on the noise bandwidth

Assuming once again that the quantization noise is random, the spectral density of the noise is given by:

$$E(f) = e_{RMS}\left(\frac{2}{kF_s}\right)^{1/2} \qquad \text{(Eq. 4.4)}$$

Converting this to noise power by squaring it and integrating over the bandwidth of interest ($F_s/2$) the result is:

$$n_0^2 = \frac{e^2{}_{RMS}}{k} \qquad \text{(Eq. 4.5)}$$

The noise in the bandwidth of interest is decreased by the factor of oversampling k.

All this improve the SNR as shown in the following expression:

$$SNR_{dB} = 20\log\left(\frac{\frac{FS}{2\sqrt{2}}}{\frac{FS}{2^N\sqrt{12k}}}\right) = 6.02N + 1.76 + 10\log(k) \qquad \text{(Eq. 4.6)}$$

The SNR for a 1-bit ADC is 7.78dB (6.02 + 1.76). Each factor-of-4 oversampling increases the SNR by 6dB, and each 6dB increase is equivalent to gaining one bit. To achieve 16-bit resolution you must oversample be a factor of 4^{15}, which is not realizable. But, sigma-delta converters overcome this limitation with the technique of noise shaping, which enables a gain of more than 6dB for each factor of 4x oversampling.

4.1.2 Noise shaping

To understand noise shaping, consider the block diagram of a sigma-delta modulator of the first order (Fig. 4.3). It includes a difference amplifier, an integrator, and a comparator with feedback loop that contains a 1-bit DAC. This DAC is simply a switch that connects the negative input of the difference amplifier to a positive or a negative reference voltage. The purpose of the feedback DAC is to maintain the average output of the integrator near the comparator's reference level.

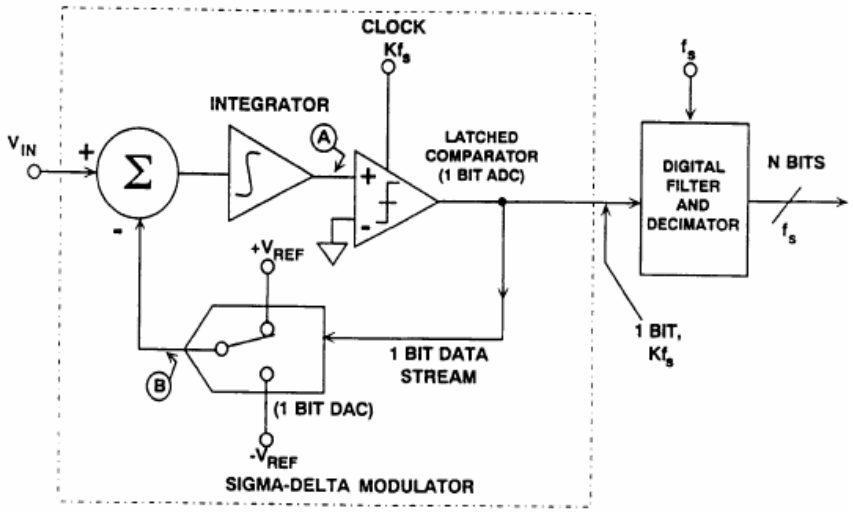

Fig. 4.3: Analog side of a sigma-delta converter

The density of "ones" at the modulator output is proportional to the input signal. For an increasing input the comparator generates a greater number of "ones," and vice versa for a decreasing input (Fig. 4.4).

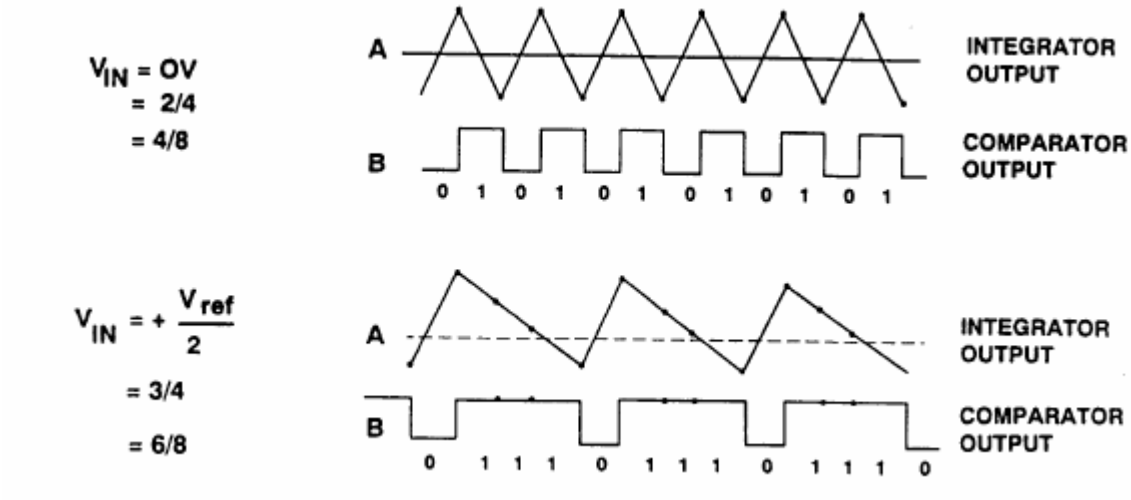

Fig. 4.4: Sigma-delta modulator waveform

By summing the error voltage, the integrator acts as a lowpass filter to the input signal and a highpass filter to the quantization noise. To show this effect we analyse in the Laplace domain the linearized model of 1st order sigma-delta modulator.

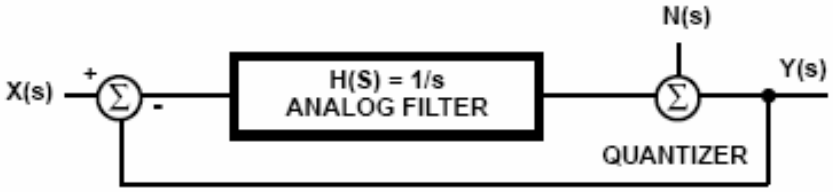

Fig. 4.5: Block diagram of the linearized model of the sigma-delta modulator

Considering N(s)=0:

$$\frac{Y(s)}{X(s)} = \frac{1/s}{1/s+1} = \frac{1}{1+s} \qquad \text{(Eq. 4.7)}$$

Considering X(s)=0:

$$\frac{Y(s)}{N(s)} = \frac{1}{1+1/s} = \frac{s}{s+1} \qquad \text{(Eq. 4.8)}$$

Thus, most of the quantization noise is pushed into higher frequencies (Figure 4.6). Oversampling has changed not the total noise power, but its distribution.

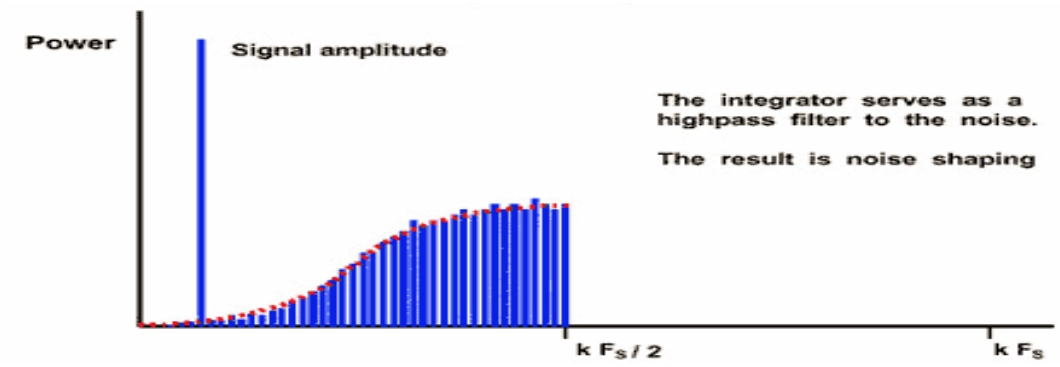

Fig. 4.6: Affect of the integrator in the sigma-delta modulator

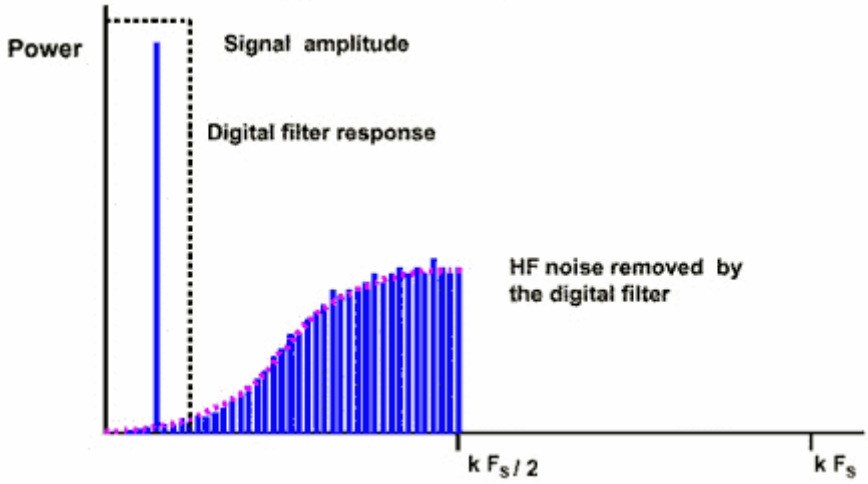

Fig. 4.7: Filter of the shaped noise

If we apply a digital filter to the noise-shaped delta-sigma modulator, it removes more noise than does simple oversampling (Figure 4.7).

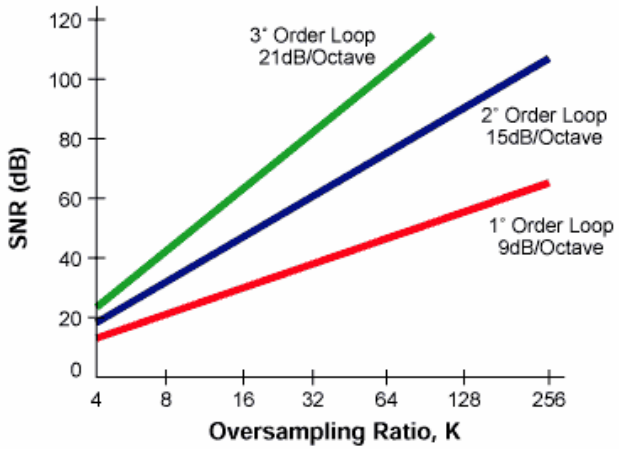

Fig. 4.8: Relationship between order of sigma-delta modulator and the amount of over-sampling necessary to achieve a particular SNR

This type of modulator (first-order) provides a 9dB improvement in SNR for every doubling of the sampling rate. For higher orders of quantization, we can achieve noise shaping by including more than one stage of integration and summing in the sigma-delta modulator. Fig. 4.8 shows the relationship between the order of the sigma-delta modulator and the amount of over-sampling necessary to achieve a particular SNR.

4.1.3 Digital and decimation filter

The output of the sigma-delta modulator is a 1-bit data stream at the sampling rate, which can be in the megahertz range. The purpose of the digital-and-decimation filter (Fig. 4.9) is to extract information from this data stream and reduce the data rate to a more useful value. In a sigma-delta ADC, the digital filter averages the 1-bit data stream, improves the ADC resolution, and removes quantization noise that is outside the band of interest. Because bandwidth is reduced by the digital output filter, the output data rate can satisfy the Nyquist criterion even though it is lower than the original sampling rate. This can be accomplished by preserving certain input samples and

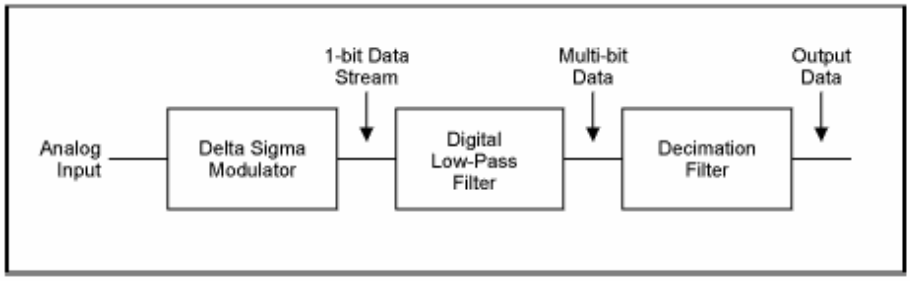

Fig. 4.9 Digital side of sigma-delta modulator

discarding the rest. This process is known as decimation by a factor of M (the decimation ratio). M can have any integer value, provided that the output data rate is more than twice the signal bandwidth (Fig. 4.10). If the input has been sampled at f_s, the filtered-output data rate can therefore be reduced to f_s/M without loss of information.

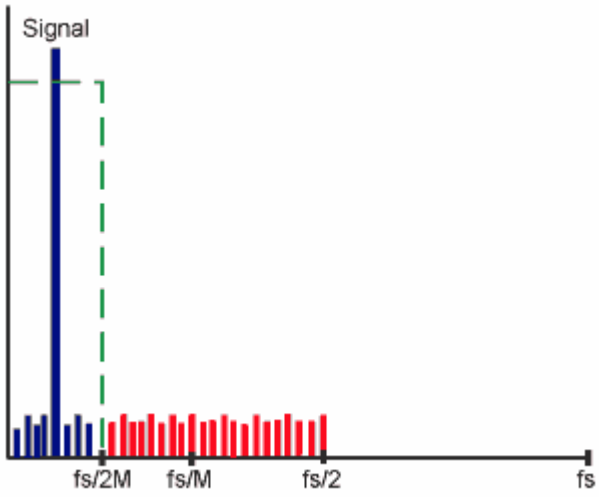

Fig. 4.10: Decimation does not cause any loss of information

4.2 Features of the data board NI 4472

4.2.1 Signal sources

Fig. 4.11 shows the input configurations for floating and grounded signal sources.

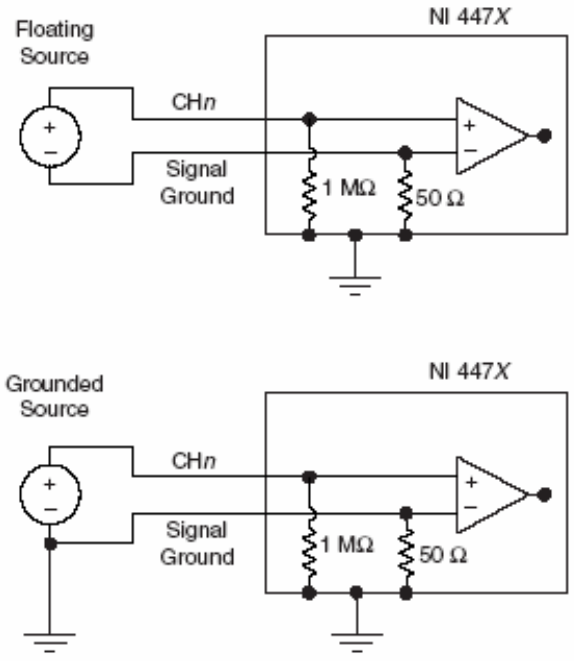

Fig. 4.11: Input Configurations for the NI 4472

A floating signal source does not connect in any way to the building ground system but instead has an isolated ground-reference point. A ground-referenced signal source connects in some way to the building system ground and is, therefore, already connected to a common-ground point with respect to the NI 4472. The output signals from the accelerometers and the microphone are floating sources; it is important to tie the ground reference of a floating signal to the ground to establish a local reference for the signal. Otherwise, the measured input signal varies as the source floats out of the common-mode input range. With the NI 4472, you tie the signal ground to the ground simply by attaching the signal cable to any of the AI channel SMB connectors. Hence, all floating signals fed to the NI 4472 are automatically ground referenced. This configuration (floating sources) has been chosen because it allows connecting signal floating sources to a ground reference, provided by the data acquisition board, so to avoid any current-loop due to the possible potential difference between two points connected to the earth potential.

4.2.2 Generating onboard current excitation with ICP circuitry

As anticipated above, this board has an independent software-switchable 4 mA current source for each channel. This current source has been set to the ON value by the software developed for the data acquisition, for the channels 5 to 8 on which the AP accelerometers are connected; this ICP circuitry gives a DC voltage around 11 Volts enough to polarize the preamplifiers. When ICP signal conditioning is enabled, large DC-offset voltages can occur on signal inputs due to the output bias voltage requirements of the ICP transducer you are using. On this board it is possible to configure each channels to be AC or DC coupled by software; to remove the offset, due to the ICP circuitry, it is enough to set the AC-coupled mode on the channels 5 to 8.

4.2.3 Input range

The NI 4472 analog inputs are bipolar; that is, the input voltage range is centered on 0 V. The input voltage range is ±10 V with 1.19 μV resolution (LSB), and is always at a gain of 1.0 (0 dB). If the gain was variable it would be possible to adjust it to have an input signal

with a such amplitude level to stress all the input range and then to have always the minimum quantization noise that leads to this percentual error:

$$e = \frac{1.19\mu V}{20V} = 0.06\,ppm \qquad \text{(Eq. 4.9)}$$

If the input signal has a 20 V_{pp} amplitude (peak-to peak) the quantization error is maximum 0.06 ppm, but if the input signal has a 20mV_{pp} amplitude the quantization error becomes 60 ppm.

However, as shown in the numerical example, the fix gain is not so severe matter because the NI 4472 has 24-bit resolution which guarantees a good resolution even if the signal has an amplitude level les than input range. In addition, since the NI 4472 does not have hardware to adjust the input gain, the component count in the input signal path is reduced, resulting in less noise and distortion. If the input signal has amplitude greater than 10 Volt, it is clipped and introduces large errors that can be easily identified in the frequency spectrum.

All data read from the ADC are interpreted as two's complement format. In two's complement mode, digital data values read from the analog input channel are either positive or negative.

4.2.4 Analog input signal conditioning

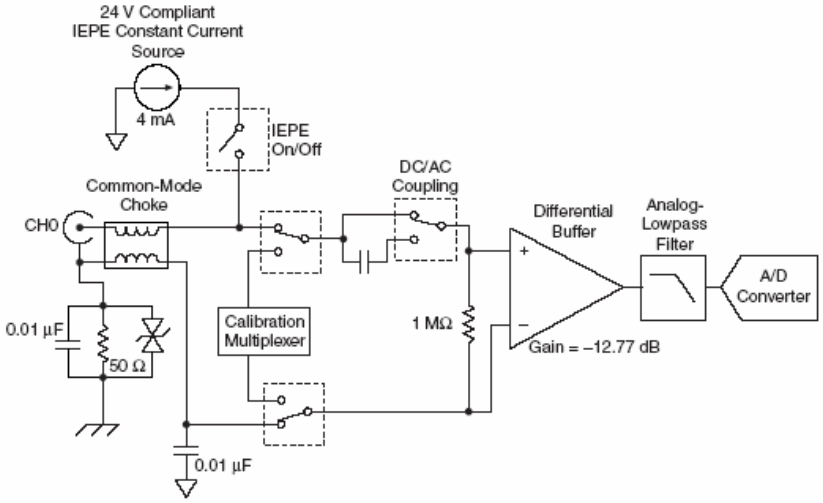

Fig. 4.12 Input stage of NI 4472

The AI stage presents high-input impedance to the AI signals connected to the NI 447*2*. Signals are routed to the positive inputs of the AI stage, and their returns are routed to AIGND through a common-mode choke. The NI 447*2* ADCs measure these signals when they perform A/D conversions.

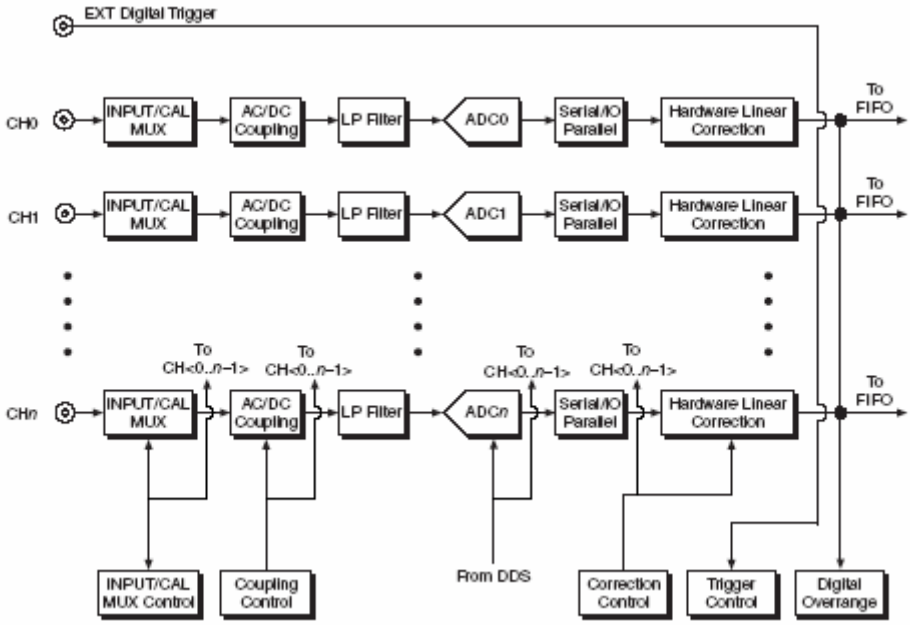

Fig. 4.13 Analog function block diagram

4.2.5 Digital stage

These input channels have 24-bit resolution and are simultaneously sampled at software programmable rates from 102.4 kS/s down to 1.0 kS/s in 190.7 μS/s increments for *f*s > 51.2 kS/s or 95.37 μS/s increments for *F*s < 51.2 kS/s.

The NI 4472, as a sampling system, can only represent signals with a maximum frequency of *F*s/2, if F_s is the sampling rate. This maximum frequency is known as the *Nyquist frequency*. The bandwidth from 0 Hz to the Nyquist frequency is the *Nyquist bandwidth*. If a signal is input to the sampling system with components that exceed the Nyquist frequency, the sampler can not distinguish these parts of the signal from some signals with frequency components less than the Nyquist frequency; the process by which the sampler

modulates these frequency signal, higher than $f_s/2$, back into the 0 to $f_s/2$ baseband is called aliasing.

To avoid aliasing, it is important to input to the sampler only those signals that can be accurately represented and then a low-pass filter is applied to the signals before they reach the sampler.

The NI 4472 includes two pole anti-alias low pass filter for each input channel. This filter has a cut-off frequency of about 400kHz and an extremely flat frequency response in the bandwidth of interest.

The analog filter precedes the analog sampler. In the NI 4472 the analog sampler operates at 64 times the selected sample rate for rates above 51.2 kS/s, and at 128 times the selected rates for rates at and below 51.2 kS/s. the analog sampler is a 1-bit. The 1-bit oversampled data that the analog sampler produces is passed onto a digital antialiasing filter that is built into the ADC chip. This filter also has extremely flat frequency response and no phase error, but its roll-off near the cut-off frequency (about 0.4863 times the sample rate) is extremely sharp, and the rejection above 0.5465 times the sample rate is greater than 110 dB. The output stage of the digital filter resamples the higher frequency data stream at the output data rate producing 24-bit digital samples.

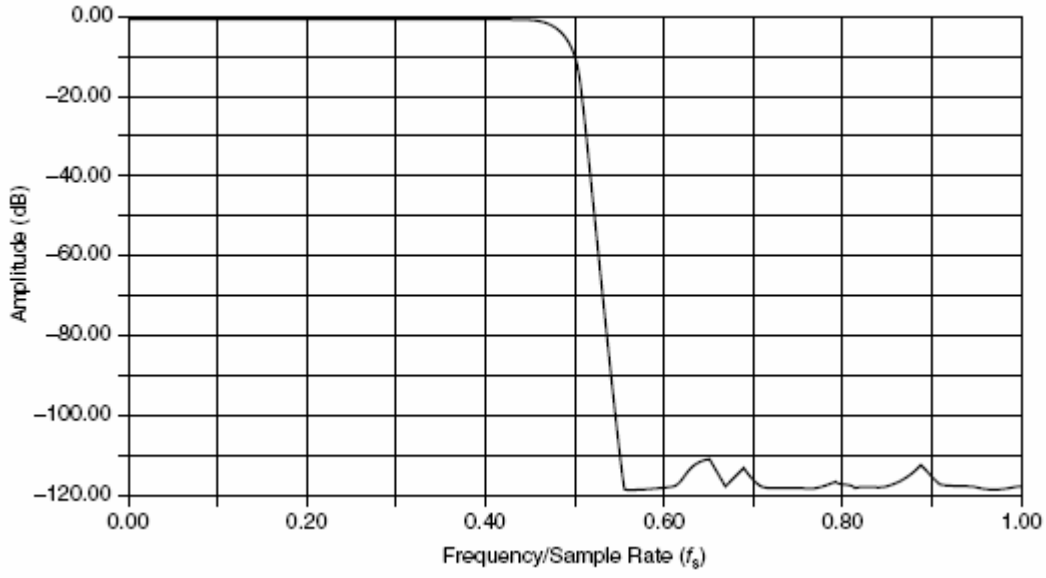

Fig.4.14: Input frequency response

However, the digital filter can do nothing about components that lie close to integer multiples of the oversampling rates (64 for f_s>51.2 kS/s and 128 at and for f_s<51.2 kS/s) because it can not distinguish these components from components in the baseband. If for

instance, the sample rate is 50 kS/s and a signal component lies within the range 6.4 MHz-6.425 MHz, this signal is aliased into the baseband because of the oversampling at 128*50kS/s=6.4 MS/s. The purpose of the analog filter is to remove these higher frequency components near multiplies of the oversampling rate before they get to the sampler and the digital filter. Because the frequency response of the analog filter is fixed and it is a second-filter order with a roll-off rather slow, it presents a good alias rejection at high sample rates (Fig. 4.15).

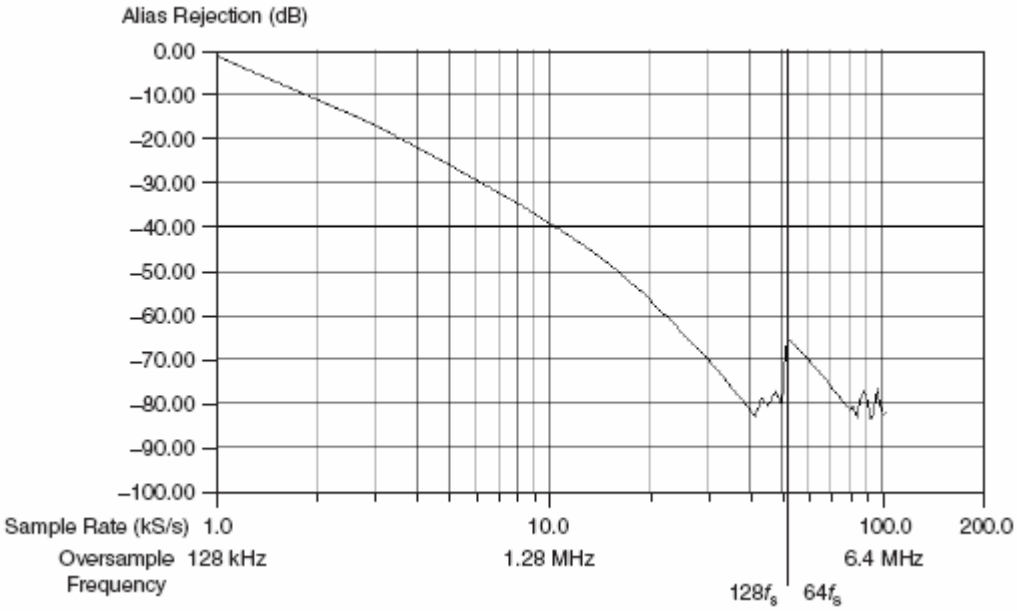

Fig. 4.15: Alias rejection at the oversample rate

No filter can prevent a type of aliasing caused by a clipped or over-range waveform, that is, one that exceeds the voltage range of the ADC. When clipping occurs, the ADC assumes the closest value in tits digital range to the actual value of the signal, which is always +8388607(2^{23}-1) or -833608 (-2^{23}). Clipping causes a corruption the corrupted digital data to have high frequency energy which is spread throughout the frequency spectrum and is aliased back into the baseband.

4.3 Characterization of the board

During the development of the software for the remote data acquisition, some tests were performed to characterize the NI4472 board. A function generator PHILIPS was used to

analyse the behaviour of the board for an input sinusoidal signal. Thanks to an automatic testing programme, developed in collaboration with my colleagues Greco G., Guerriero P. and Toticone F. of Naples, it was enough to read the data from a file, previously acquired to analyse the signal in the time and frequency domain.

We were interested in understanding the effective noise level, to compare it with the noise level of the accelerometers and microphone, and the effective number bit (ENB) of the board as during the developing of the software for the data acquisition, it was noted that the routine for the acquisition was based on an array of *short int* (16 bit) as we will describe in more details in the following chapter; that was not completely clear because the NI4472 has a 24-bit resolution.

However a complete characterization of the board was not possible because the function generator should have a very high performing DAC, more precise than the board, to not influence the test.

The analysis is based on the IEEE standard for digitizing waveform recorders 1057-1994. A sine wave is applied in input to the board with a specified frequency and amplitude set on the generator, to calculate the signal-to-noise ratio by Fast Fourier Transform (FFT). The signal-to-noise ratio (SNR) is defined as

$$SNR_{dB} = 10\log\left(\frac{V_s^{\,2}}{V_n^{\,2}}\right) \qquad \text{(Eq. 4.10)}$$

where V_s, and V_n are the rms amplitudes of the signal and noise, respectively.

You can think of an FFT as a set of parallel filters, each $\Delta f=F_s/N$ (N is the number of points acquired) in bandwidth. Because of the spreading effect of a window, each window increases the effective bandwidth of an FFT bin by an amount known as the equivalent noise-power bandwidth of the window. The power of a given frequency peak is computed by adding the adjacent frequency bins around a peak and is inflated by the bandwidth of the window.

$$EstimatedPower = V_s^{\,2} = \frac{\sum_{i=j-n}^{j+n} Power(i)}{noise\_powerbandwidth\_of\_Window} \qquad \text{(Eq. 4.11)}$$

where *j* is the the index of the peak and *n* depends by the window applied in the FFT algorithm.

The broadband noise level is computing in V_{rms}^2 by summing all the power spectrum bins, excluding any peaks and the DC component, and dividing the sum by the equivalent noise bandwidth of the window. In the programme the SNR has been computing as explained above.

Because of noise-level scaling with Δf, spectra for noise measurement are often displayed in a normalized format called power or amplitude spectral density. This normalizes the power or amplitude spectrum to the spectrum that would be measured by a 1 Hz-wide square filter, a convention for noise-level measurements. The level at each frequency line then reads as if it were measured through a 1 Hz filter centred at that frequency line. Power spectral density is computed as

$$Power\_spectral\_density = \frac{Power\_spectrum\_in\_V_{rms}^2}{\Delta f * noise\_power\_bandwidthofwindow} \qquad \text{(Eq. 4.12)}$$

The units are then in V^2/Hz; the amplitude spectral density is computed as

$$Amplitude\_spectral\_density = \frac{Amplitude\_spectrum\_in\_V_{rms}}{\sqrt{\Delta f * noise\_power\_bandwidthofwindow}} \qquad \text{(Eq. 4.13)}$$

the units are in V/√Hz.

Window	Scaling Factor (Coherent Gain)	Noise Power Bandwidth	Worst-Case Amplitude Error (dB)
Uniform (none)	1.00	1.00	3.92
Hann	0.50	1.50	1.42
Hamming	0.54	1.36	1.75
Blackman-Harris	0.42	1.71	1.13
Exact Blackman	0.43	1.69	1.15
Blackman	0.42	1.73	1.10
Flat Top	0.22	3.77	< 0.01

Tab. 4.2 : Correction Factors and Worst-Case Amplitude Errors for Windows

Analyisis

The following pictures show the panel for the automatic test of ADC.

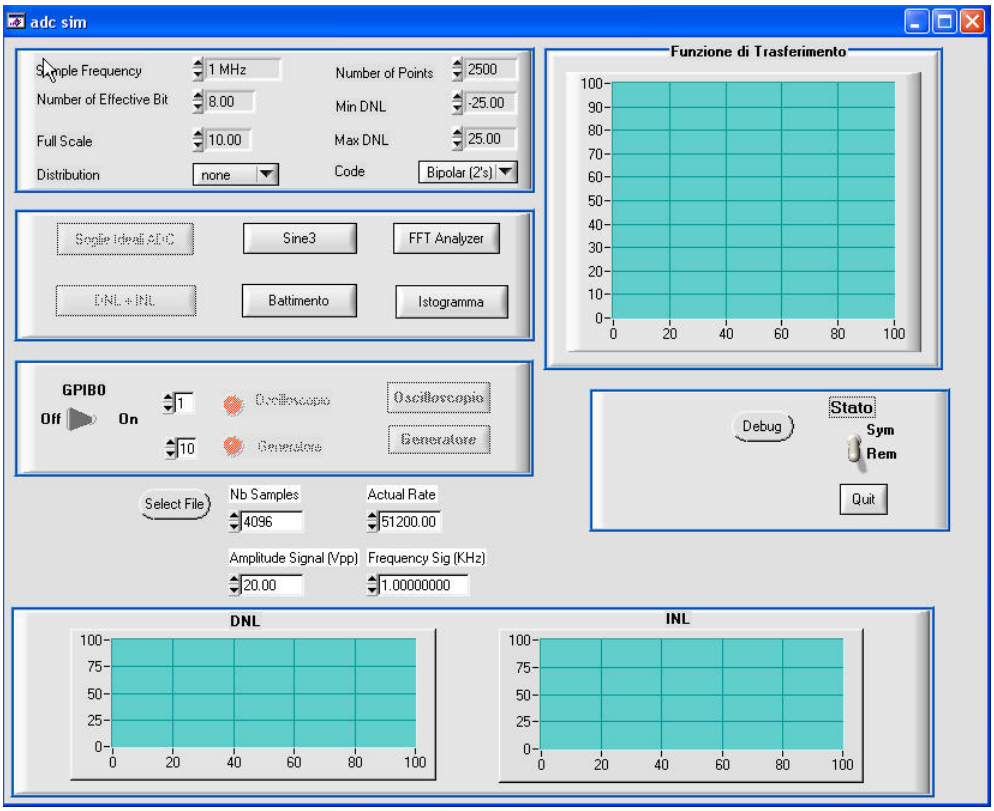

Fig. 4.16: Main panel of the automatic programme for ADC test

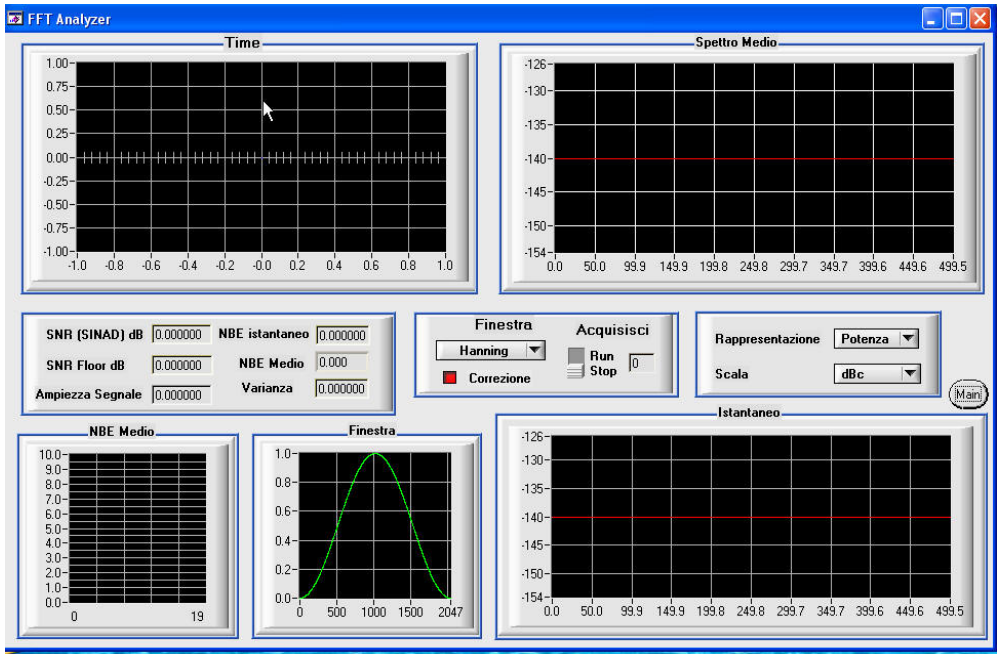

Fig. 4.17: FFT analyzer panel

To load the file, we have to specify the sampling frequency, the number of points acquired, the amplitude and the frequency of the input sine wave. By pushing the command button FFT analyzer we can see the result of the analysis in the domain frequency which is described above.

We show the FFT of sine wave at different frequency at the maximum sampling frequency 102.4 kS/s; the amplitude is always 9 Volt to cover up a wide amount of the range input without causing saturation due to the over-range.

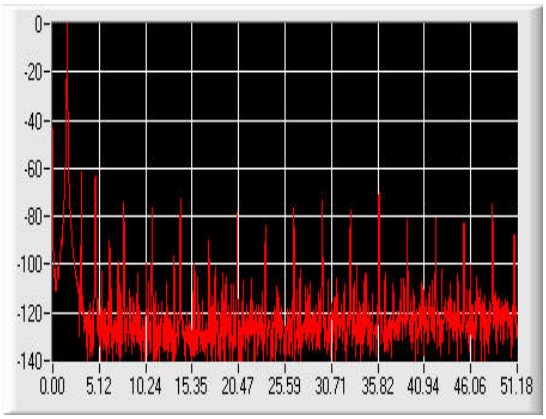

Fig. 4.18: Sine wave at 1.5625 kHz

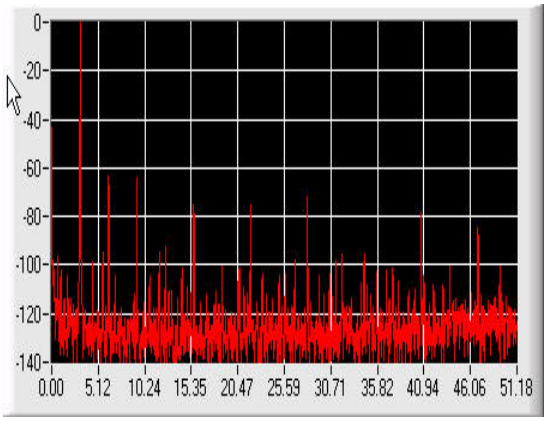

Fig. 4.19: Sine wave at 3.125 kHz

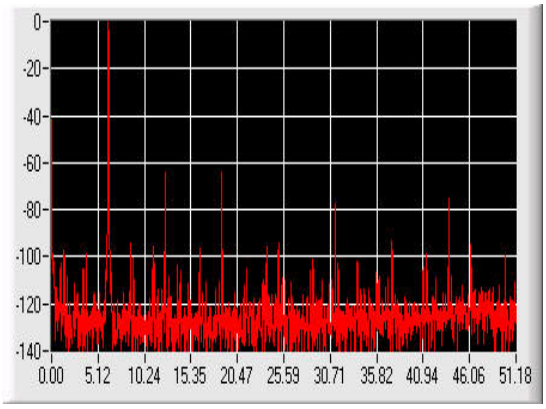

Fig. 4.20: Sinewaveat6.25kHz

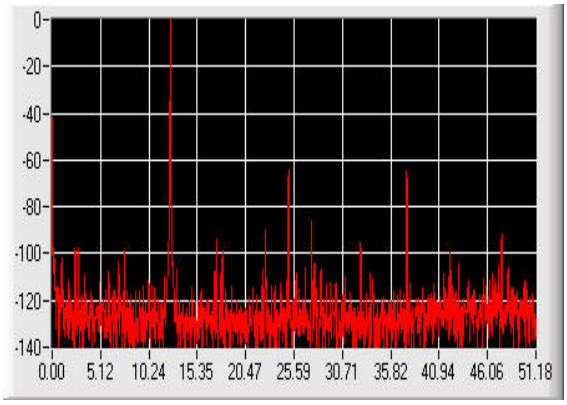

Fig. 4.21: Sine wave at 12.5 kHz

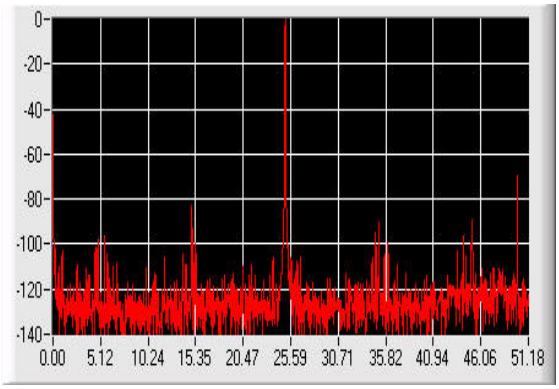

Fig. 4.22: Sine wave at 25 kHz

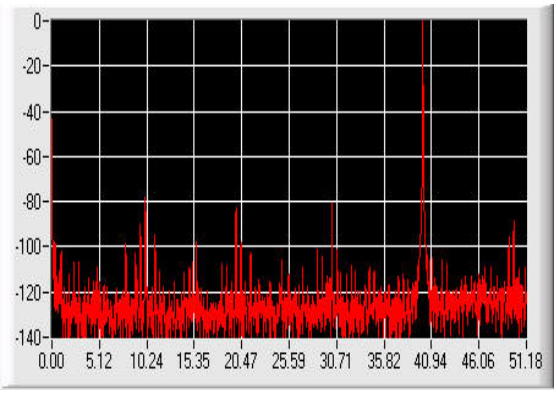

Fig. 4.23 : Sine wave at 40 kHz

The last sine wave is not at 50 kHz because this frequency would be attenuated by the digital filter of the board whose cut-off frquency is at 0.4863 times the sampling rate. The FFT is plotted by normalizing the power spectrum to the maximum peak. The noise level is around 120 dB below the maximum peak which represents the V_s^2 of the input signal. The noise RMS level V_n^2 is evaluated by summing all the power spectrum bins, excluding any peaks and the DC component; from these values, V_n^2 and V_s^2, we can calculate the signal-to noise ratio which is called SNR floor; it is around -109 dB for F_s<51.2kS/s and around -104 dB for F_s>51.2kS/s, due to the reduction of the oversampling factor from 128 to 64. The plot below represents the SNR floor computing for acquisitions at F_s equal to 25 kHz, 51.2 kHz, 75 kHz and 102.4 kHz.

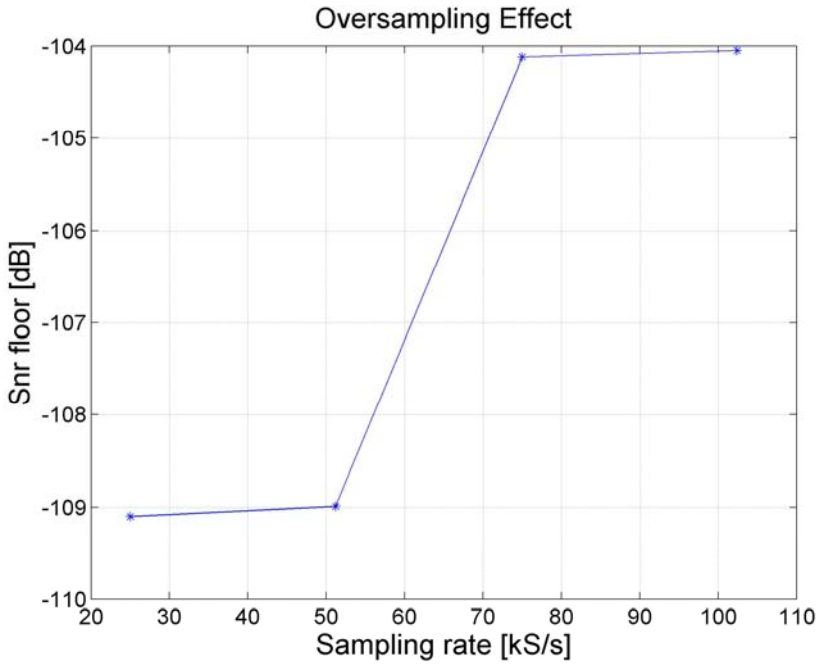

Fig. 4.24: Change in the noise level at 51.2 kHz

These values are in according with the idle channel noise specified in the data-sheet of the board (Tab. 4.1).

The SNR floor is computed without including the peaks at the multiple frequency of the frequency signal because through this parameter we want to compute the signal-to-noise ratio and the effective number bit (ENB) without including any kind of distorsion which are introduced by the generator as we discuss in more details after.

$$ENB = \frac{SNR\_floor_{dB} - 1.76}{6.02} \qquad \text{(Eq. 4.14)}$$

The value is much less than 24 bit which is the nominal bit number of the board and in besides it was evalueted considering only the quantization noise; to understand what this result means we have to do some considerations.

If we consider that the board has 24-bit resolution and that the amplitude sine wave is 9 Volt, the quantization noise of the board, which should be the only noise source in the computing of the SNR floor, leads to this pecentual error

$$error = \frac{1.19\mu V}{18V} = 0.065\,ppm \qquad \text{(Eq. 4.15)}$$

This percentual error is very low and then if we want to individuate it, the other instruments which we use to test the board, should assure a percentual error less than the one of the board. The function generator PHILIPS does not have this precision and so a complete characterization of the board is not possible by a dinamic test based on the computing of the SNR. By considering the peaks at multiple frequencies of the input signal, which indicate other kind of distorsion not due to the quantization error, the SNR is around 60 dB.

We realized an active filter to demonstrate that this value of SNR is prevalently the result of the distorsions introduced by the function generator.

We used the MAXIM 8th-order Continuous-Time Active Filter MAX 274 which is composed of four 2nd order filter sections connected in series. Any section (A, B, C, D) can implement any all-pole bandpass or lowpass filter response and is programmed by four resistors(Fig. 4.25).

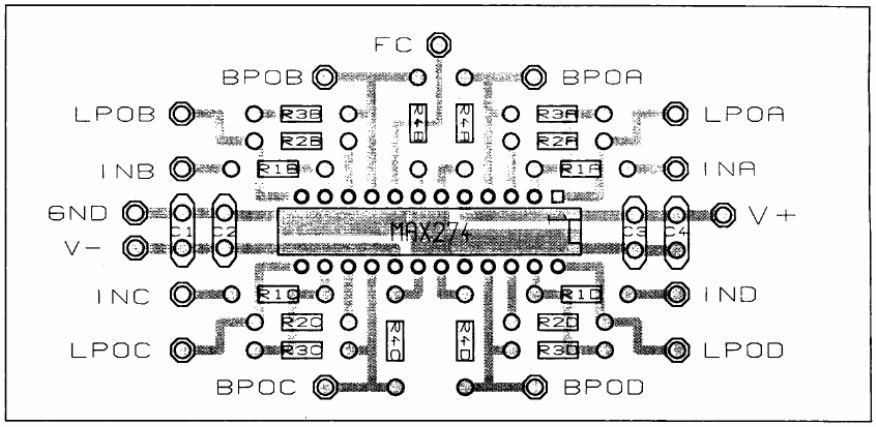

Fig. 4.25: External stage of the circuit of MAX 274

The external components (resistors) have been chosen by using a software kit, to realise a Chebyshev pass-band filter 8th order whose features are resumed in the following tab. 4.3

Center frequency [Hz]	Pass bandwidth [Hz]		Stop bandwidth [Hz]	
20000	200		4000	
	Lower limit	Upper limit	Lower limit	Upper limit
	19900	20100	18100	22100

Tab. 4.3

The resistances computed by software have been modified to obtain standard values. The following figures represent the FFT of a sine wave in input to the NI 4472 with the filter and without the filter, at two different sampling frequency.

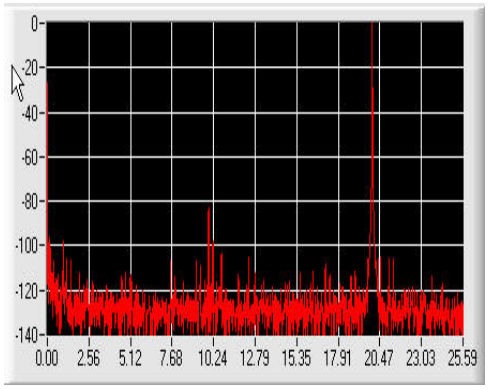

Fig. 4.26: Acquisition at 51.2 kHz without the filter

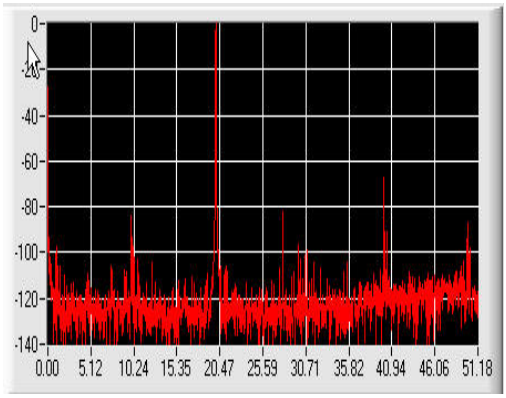

Fig. 4.27:Acquisition at 102.4 kS/s without the filter

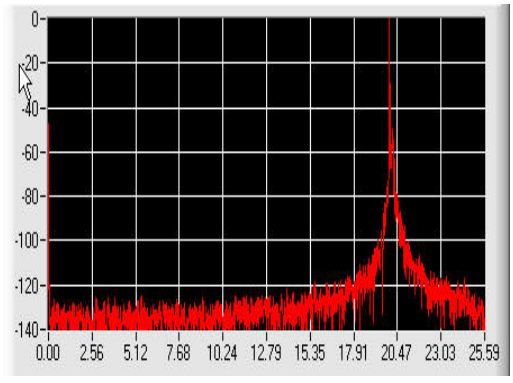

Fig. 4.28: Acquisition at 51.2 kHz with the filter

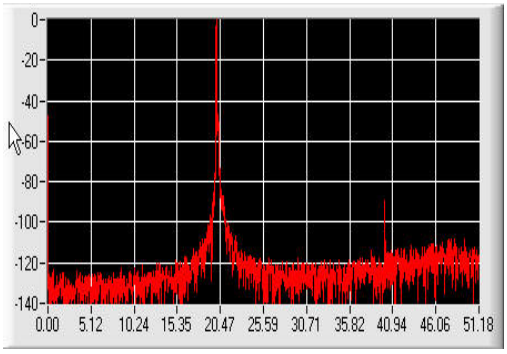

Fig. 4.29: Acquisition at 102.4 kS/s with the filter

As we explained above, the peaks at the multiple frequencies of the frequency signal are due to the function generator and not to the data acquisition board; they are not anymore present, or attenuated for the acquisitions performed with the filter mounted at the output of the generator. By analysing the filtered signal we can note the frequency repsonse of the filter whose features are not exactly equal to the ones defined in the design phase; this changing is due to the choice of standard resistors and capacitors whose values are different from the ones computed by software. After these measurements we can only adfirm that the channel noise due to the quantization error is comparable with the specifics of the data board (Tab. 4.1) because a complete characterization of an ADC with 24-bit resolution should be performed with a static test which we could not do before installing the NI 4472 in the tunnel.

Channel noise		
Sampling rate	Expected value	Measured value
1.0 kS/s<fs≤51.2 kS/s	-110 dB (min)	-109 dB
51.2 kS/s<fs≤102.4 kS/s	-105 dB (min)	-104dB

Tab. 4.4: Evaluation of the Channel noise

The broadband noise level is at least -130 dB, less of the noise level due to the sensors. The next figures represent the analysis in the frequency domain of the signals acquired by the different kinds of sensors. The channel 1, 2, 4, 6 and 7 represent respectively the sensors B&K 2273AM1, B&K 2273A, NEXUS microphone 4189 and AP40. The FFT is computed with sampling rate 50 kS/s on 4096 points and the figures represent the medium spectrum obtained by performing 150 averages for the channels 1, 2 and 4 and 10 averages for the channel 6.

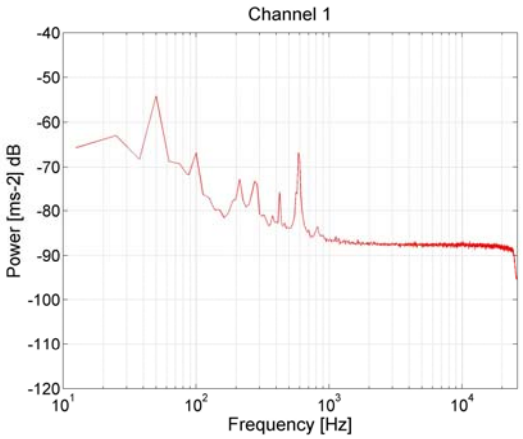

Fig. 4.30: B&K 2273AM1

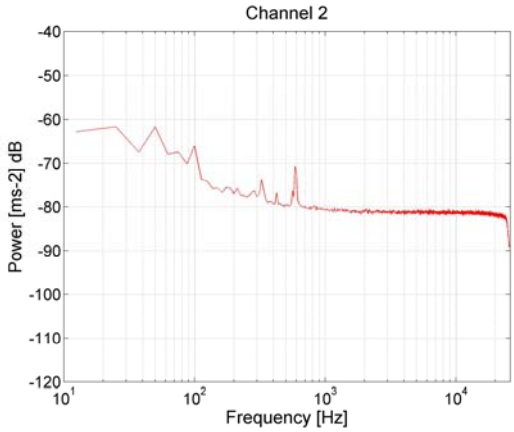

Fig. 4.31: B&K 2273A

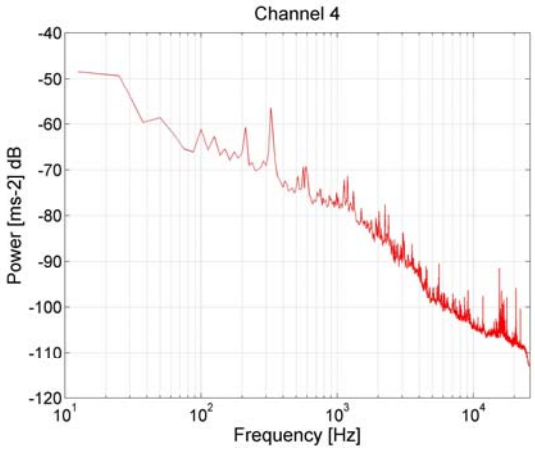

Fig. 4.32: B&K microphone

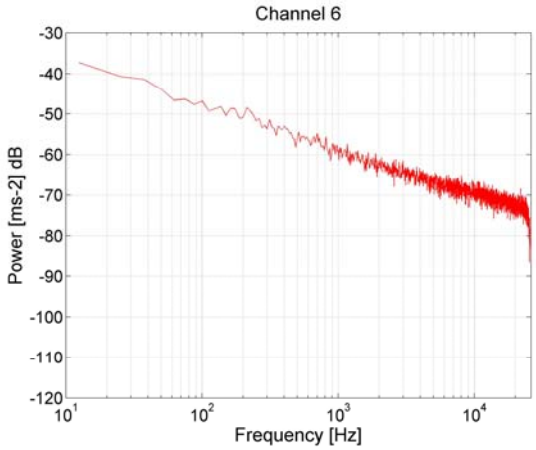

Fig. 4.33: AP40

The noise spectrum of the sensors decreases at high frequency and it is much higher than the channel noise of the board. The following table represents the values of the noise level of the sensors.

	Noise level
Data board	-100 dB
B&K2273AM1	-46 dB
B&K 2273A	-39 dB
Microphone 4189	-40 dB
AP 40	-25 dB

Tab. 4.5: Noise level

5 SOFTWARE FOR REMOTE CONTROL

In this chapter the software for the remote control of the data acquisition system with LabWindows 7.0 is presented. The different sections are:

- Acquisition and saving of the output signal of the accelerometers and of the microphone.
- First analysis.
- Remote control of the NEXUS preamplifier.

These three sections allow to perform the following functions which we list below.

First section

1. Setting of the software selectable parameters of the board (ICP circuit, Input coupling and sampling rate)
2. Choosing of the disk unit where the data will be saved in binary format (unit 1, unit 2, unit C).
3. Check of the writing operations on the disk(Back log).
4. Active control of the data acquisition (Start, Stop).
5. Conversion operations from binary to text format.
6. Reproduction of the microphone data.
7. Setting for an automatic continuous acquisition.

Second section

1. Reading data from file
2. Graphs of the acquired signals
3. Analysis in the frequency domain (FFT)

The reading is performed by scanning at regular time interval the file selected.

Third section

1. Setting of the parameters for the RS232 remote control

2. Setting of both input and output parameters of the 4 channels of the Nexus preamplifier (sensitivity, gain, low pass and high pass filter, single ended or floating point configuration).
3. Check the status of the device by reading the overload conditions.
4. Resonance test can be executed to establish if the piezoelectric accelerometers are correctly mounted.
5. Setting of the current source to provide the polarization of the microphone

The functions developed in these three sections will be described in detail in the following paragraphs.

An independent software was developed for the remote control of the palmer which allows:

1. The setting of the RS232 parameters for the remote control
2. The data acquisition
3. The setting of the main parameters of the unit display.

Another application was developed for the analysis off line of the data; its main goal is the studying of the acceleration of the collimator in three dimensions. The main functions are:

1. Loading of the data
2. Saving and analysis of a selected time interval
3. Filtering operations
4. Composition of the accelerometer data along different directions.

5.1 Data Acquisition System

The following picture shows the Main Panel of the software. From this panel it is possible to check the data acquisition and to set the main parameters of the board NI4472. There is a switch to enable the *ICP*, that is, the 4 mA current source that the board can supply independently for each channel; the *Input Mode Coupling* of the channels board is set by 8 ring slides.

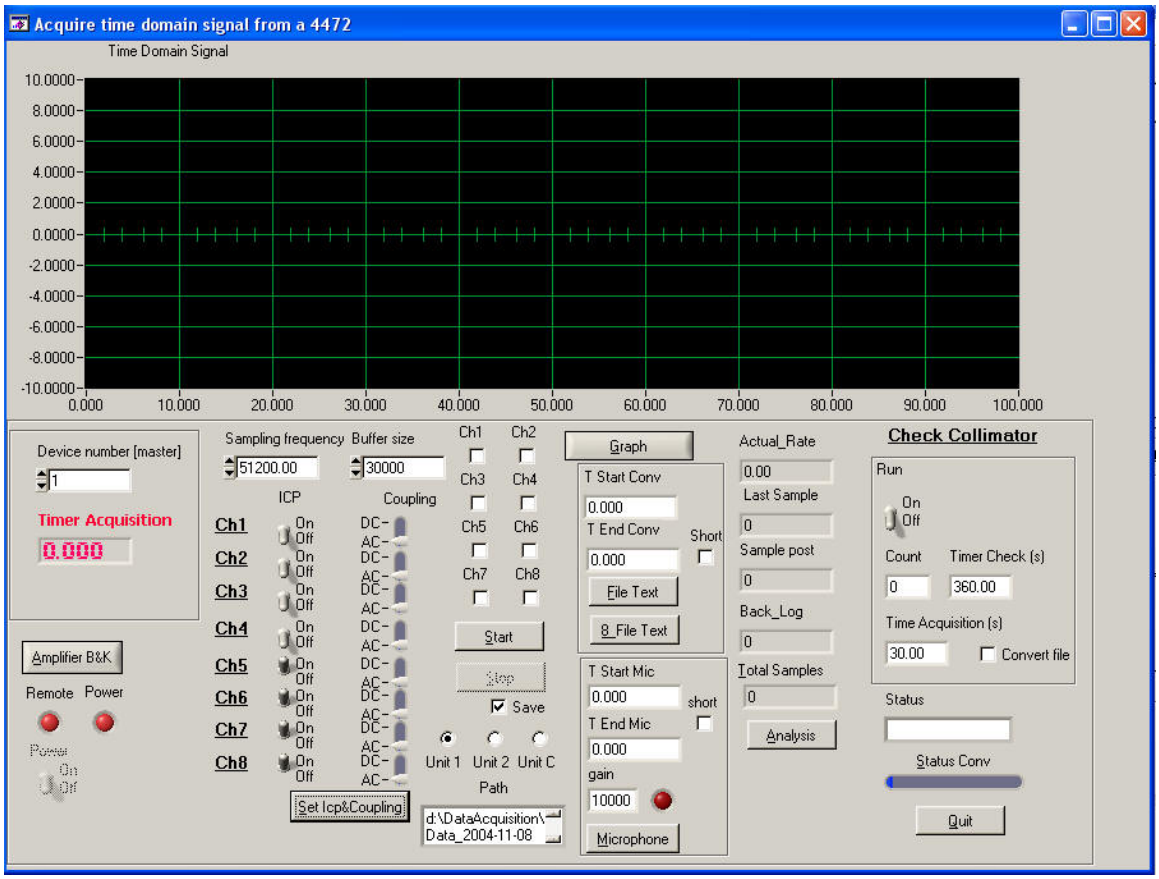

Fig. 5.1: Main panel

These options are set every time that the acquisition starts; when the acquisition is not running the ICP source is automatically switched off without changing any setting. We remind that the ICP circuit is used only for the channels 5, 6, 7 and 8 on which the AP accelerometers are connected.

The acquisition, based on the Traditional NI-Daq library, must be performed continuously at the sampling rate indicated in the numeric button *Sampling frequency*. Beginning and end of data taking are manually set with the Start/stop buttons. A scanned data acquisition is performed. The data are stored as *short int* in a big *ring_buffer* whose size is *10*nb_channel*nb_samples* ; the value of the parameter *nb_samples* can be set by panel (*Buffer size* numeric button) and nb_channel is 8. While the data are stored in the *ring_buffer*, they are converted in *double* and stored in the *Volt_Buffer* and then saved in a file in binary format every time that the size of the *ring_buffer* increases of an amount equal to 8**nb_samples.* This technique allows to empty the *ring _buffer* to avoid an overwrite error: for running the continuous acquisition without error, the element *i* of the buffer must be

empty when the sample *n*10*8*nb_samples+i* has to be stored, where *n* can be equal or greater than 1. The overwrite condition can occur if the sampling rate is high because of the saving of the data on the Disk. The performance are influenced by the reading time and the buffer size of the Disk too. For the acquisition at sampling rate greater than 51.2 kS/s nb_samples has been chosen 30000.

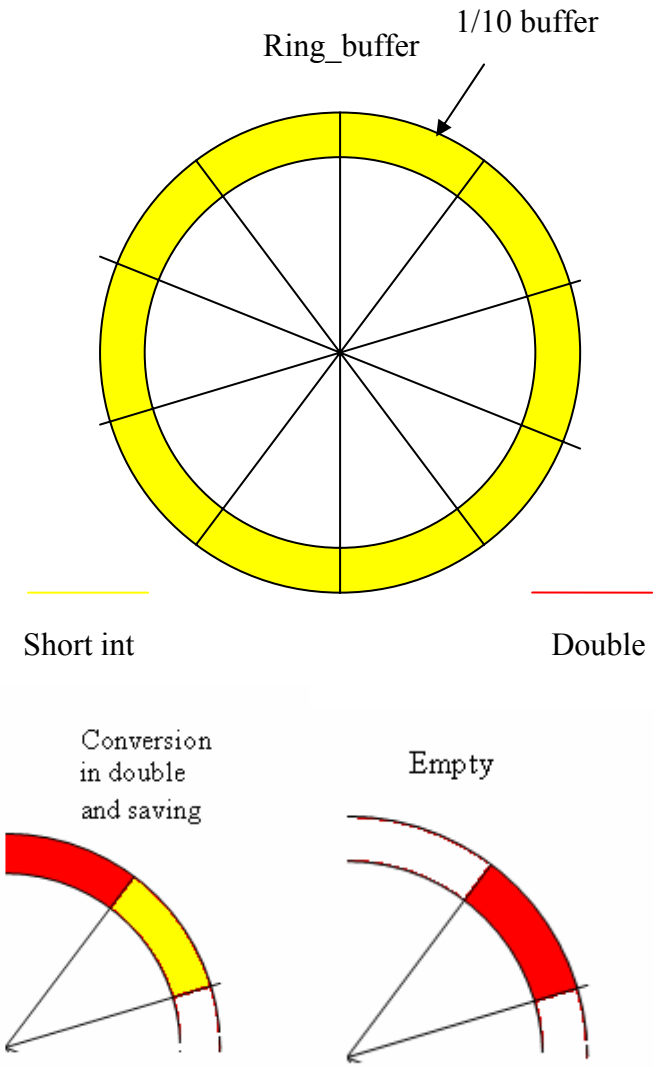

Fig. 5.2: Continuous acquisition based on a dynamic buffer

While the acquisition is running, the data stored in the *Volt_Buffer* are separated for channel and stored in 8 different arrays which are used to plot the data; on the *Time Domain Graph* the channels enabled by the *check (ch1, ch2, ch3,ch4, ch4, ch5, ch6, ch7, ch8)* are displayed on the graph. By pushing the button *graph* another panel appears where it is possible to display the 8 channels on 8 different graphs.

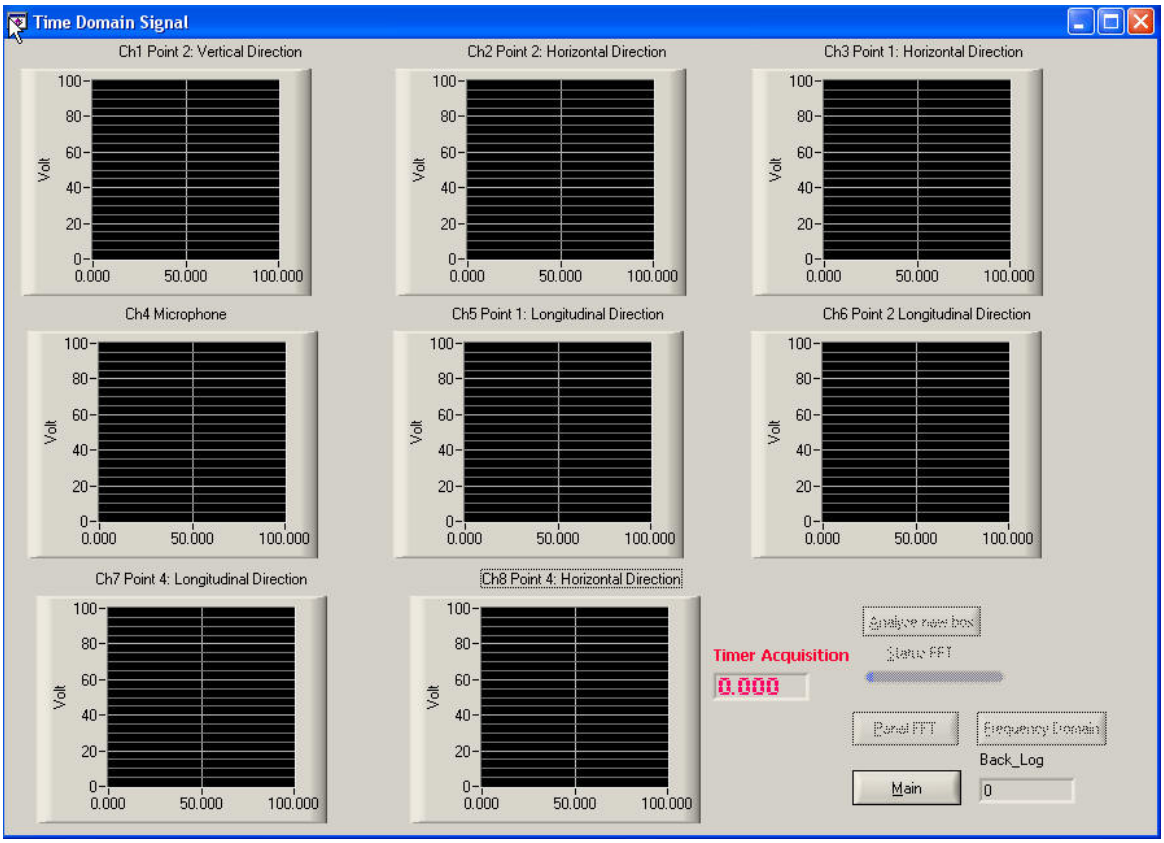

Fig. 5.3: This panel shows the signals of the 8 channels while the acquisition is running

By selecting the check *save* it is possible to save the data on the disk; if there is no check the acquisition is performed without saving data; The data can be saved in *unit 1* or *unit 2* or *unitC*, which indicates the three disk installed in the pc of the tunnel, in the folder typed in the text box *Path*. We decided to install more than one disk to have a dedicated memory mass for the data. The amount of data acquired is some GB/minute with sampling rate 50kHz; here it is presented a numerical example: by considering that a double size is 8 bytes, if the acquisition is running for 1 minute at the sampling frequency 51.2 kS/s, we have:

$$Total\_samples = F_s * \Delta t * n\_channels = 51200 * 60 * 8 = 24576000 \qquad \text{(Eq. 5.1)}$$

$$size = total\_samples * n\_byte = 196.608MB \qquad \text{(Eq. 5.2)}$$

In the main panel there is the numeric button Back-log that indicates the samples acquired while the *nb_samples*8* samples are converted plotted plot and saved (if the check is enabled); it is computed by doing the difference between the *sample post* and the *Last sample* which indicates respectively the index of the sample acquired at the end of the saving of the *Volt_Buffer* converted and the index of the sample acquired when the size of the ring_buffer is

multiple of *nb_samples*8.* If Back-log increases constantly the overwrite error will happen. This is a parameter to check if the *Buffer size* parameter is adequate.

The data are saved in binary format during the acquisition because it takes less time; by pushing the command button *File Text* it is possible to select a binary file previously acquired and convert it an ASCII; if the check *short* is enabled the conversion of the file is executed only for those samples acquired in the time interval specified by *T start Conv* and *T end Conv*; this feature was added to have a quick file convertion to ASCII, around the signal of interest, for a fast transmission to control room (fast feedback acquired data). The command button *8_File Text* operates as the command *File text* but it generates an ASCII file for each channel. The command button *Microphone* allows to listen to off-line the sound acquired with the amplification factor specified in *gain*; the check *short* and the numeric buttons *T start* and *T end* allow to listen to only the specified time interval.

The section ***Check Collimator*** consents to run an automatic acquisition for the time interval specified by *Time Acquisition*; the acquisition is then repeated each Δt indicated in *Timer check; count* indicates the number of acquisitions effectuated. The check *convert file* enables also the conversion of the data from binary format to ASCII. This section was used to perform repeated acquisitions for 24 hours.

From this panel it is possible to switch on the NEXUS preamplifier whose status is indicated by the led *Remote* and *Power*; by pushing the command button Amplifier the *Amplifier panel* is displayed and then it is possible to read the settings of the device; this operation can be done even when the acquisition is running, in particular it is interesting to read the overload conditions of the preamplifier.

5.2 First analysis

After the acquisition, it is possible to do a first analysis of the data acquired; by pushing the button *Analysis* the panel in Fig. 5.4 will be displayed; the button *SelectFile_to analyse* permits to choose the ASCII file to load; in the numeric button *Window time to analyse* the time interval to read must be indicated; then it is possible to push the button *FFT* to compute the FFT for the signal of each channel. The FFT panel is shown in the Fig. 5.5. The graph *Time* and the graph *Spectrum* are referred to the signal of the channel selected on the ring slide *Channel to view*. By pushing the button *Analyse new box* the following time interval Δt of the file selected before in the panel *Analysis* will be uploaded and the computing of the FFT of the new section is executed; the graph *Time* and *Spectrum* are updated; the graph

Medium Spectrum will display the average of the FFT computed for this section and for the previous ones.

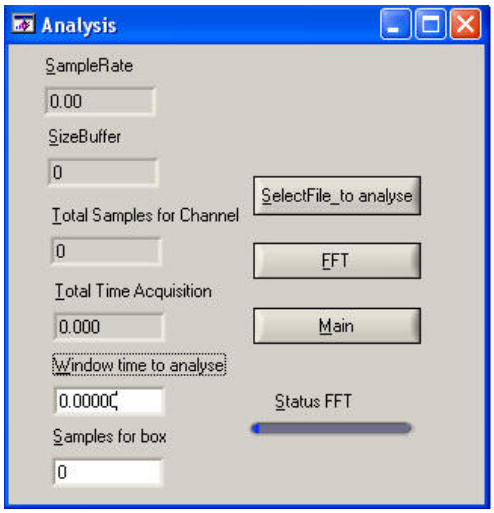

Fig. 5.4: Analysis panel allows to select the binary file to read

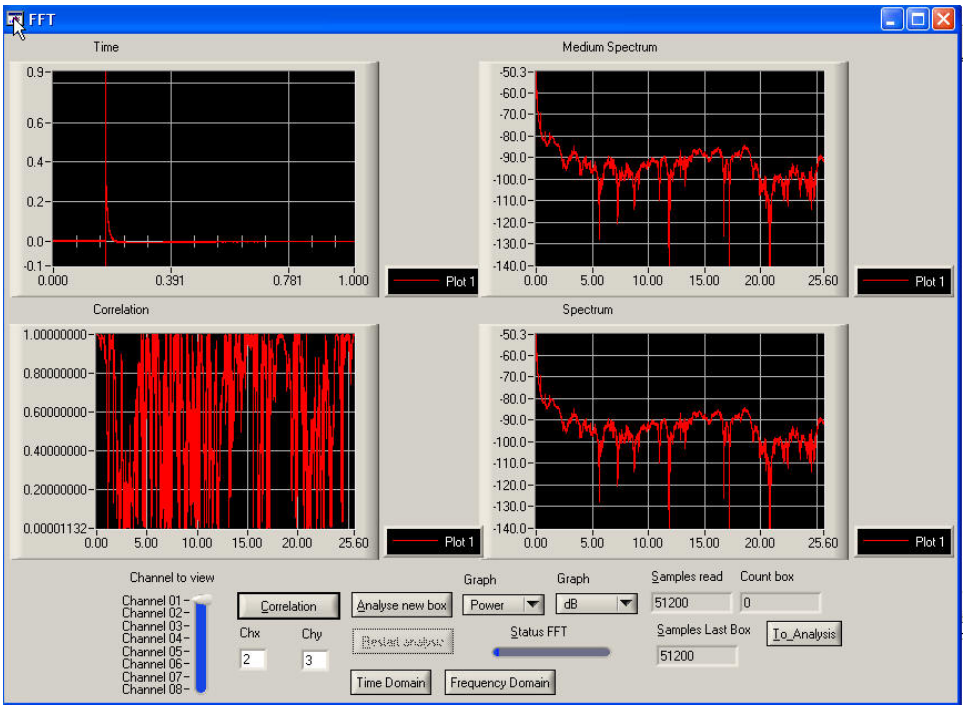

Fig. 5.5: FFT panel controls the reading of the selected file

By pushing the button Correlation the real part of the normalized mutual power spectrum of the channels indicated in *Chx* and *Chy* will appear on the graph Correlation.

$$Correlation = \mathrm{Re}\left[\frac{FFT(Chx) * FFT^{*}(Chy)}{|FFT(Chx)||FFT(Chy)|}\right] \qquad \text{(Eq. 5.3)}$$

When the end of file is reached a message of EOF will appear on the panel and then it is possible to repeat the analysis by pressing on the button Restart_analysis.

The buttons *Time Domain* and *Frequency Domain* allow to display the panels shown in the figures below where there is a graph for each channel.

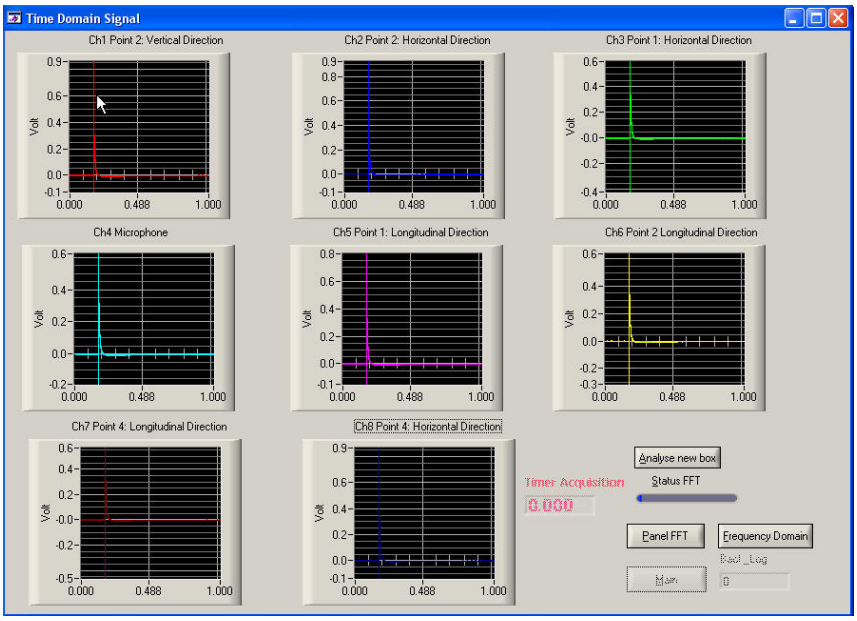

Fig. 5.6:The read data are plotted on the Time domain panel

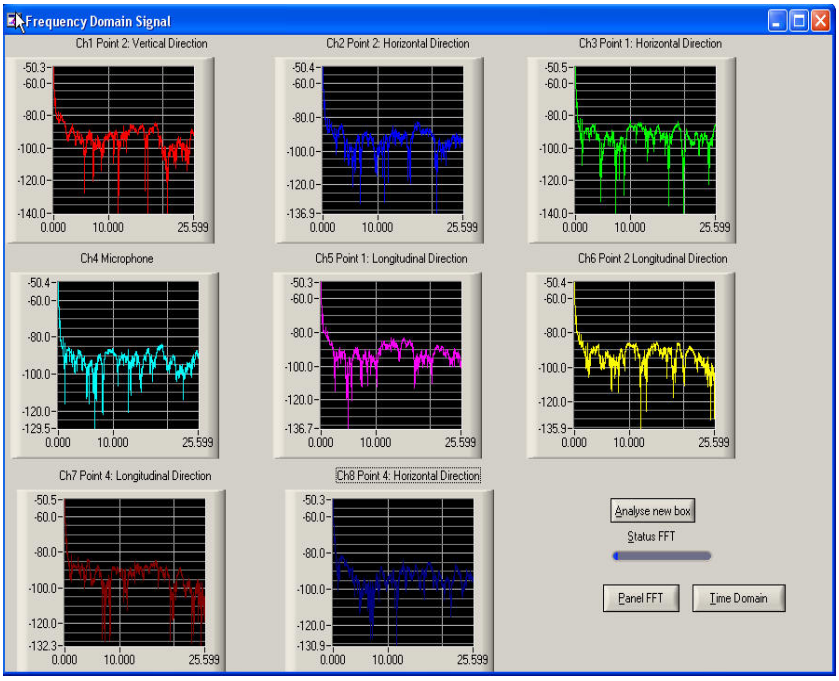

Fig. 5.7:FFT of the 8 channels

The panel *Time domain* is useful because it permits to plot the data and to check the maximum amplitude of each channel; by considering those peaks, a change in the setting of the NEXUS preamplifier may be required to avoid to acquire saturated signals.

5.3 Remote control of B&K Amplifier

As we described in the chapter three, it is possible to have a remote control of the NEXUS preamplifier via RS 232. the figure below shows the panel to programme the amplifier.

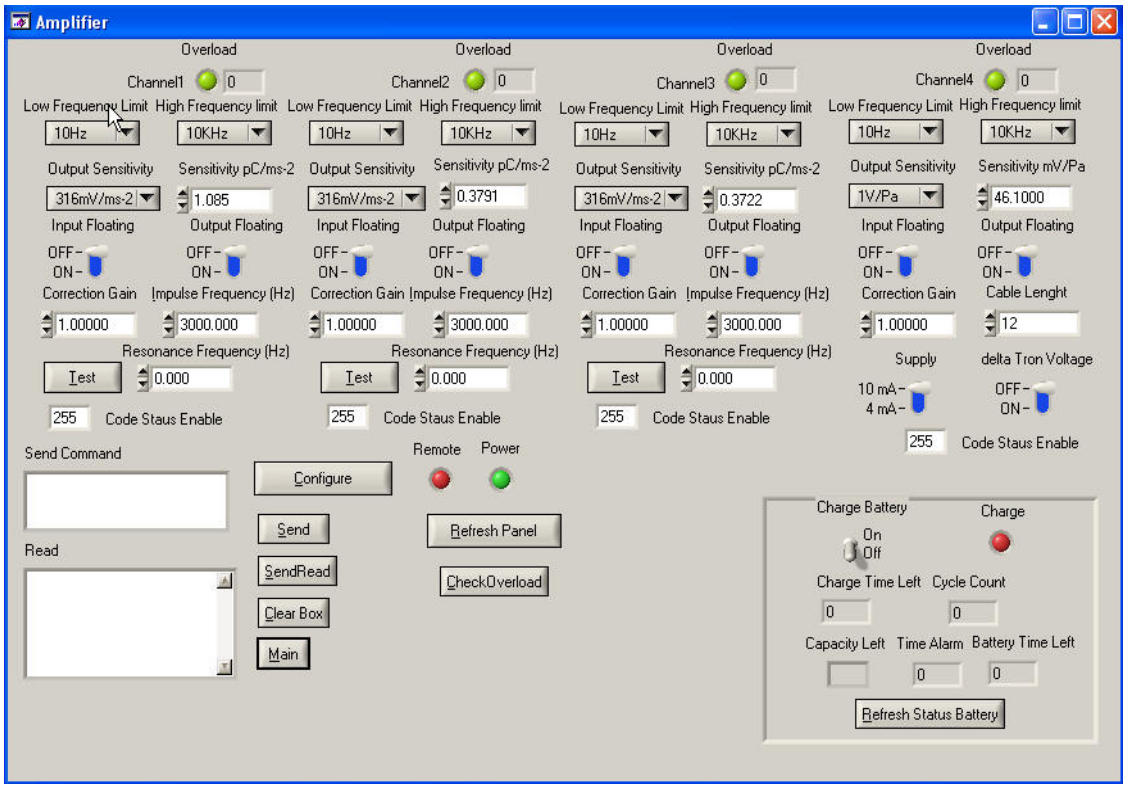

Fig. 5.8: Amplifier panel allows the control of the NEXUS preamplifier

On this panel we can see all the functions that the remote control allows to set. First sending a command to the amplifier, the parameters for the serial communication have to be chosen; pushing the command button *Configure* another panel appears where it is possible to set the number of the COM port to which the device is connected, the parity bit (for the

control of the integrity of the data), the data bits (word length), the stop bits, the time out limit for the I/O operations before to send an error message, the CTS mode and X mode, the size of the input and output queue for sending and reading operations. If *X mode* is not active the software handshaking is disabled. If *CTS mode* is not active hardware handshaking is disabled and then CTS line is ignored and both RTS and DTR are raised. The option *CTS/RTS/DTR* enables the hardware handshaking and the library monitors CTS line to determine when it is safe to send characters to the receiver and uses the RTS and DTR lines for handshaking; the *option CTS/RTS* enables the software handshaking but the library uses only the RTS line which is raised only when there is space in the input queue to receive additional characters; DTR line is raised if the port is open. The settings saved are shown in the following picture of the panel for the RS 232 configuration.

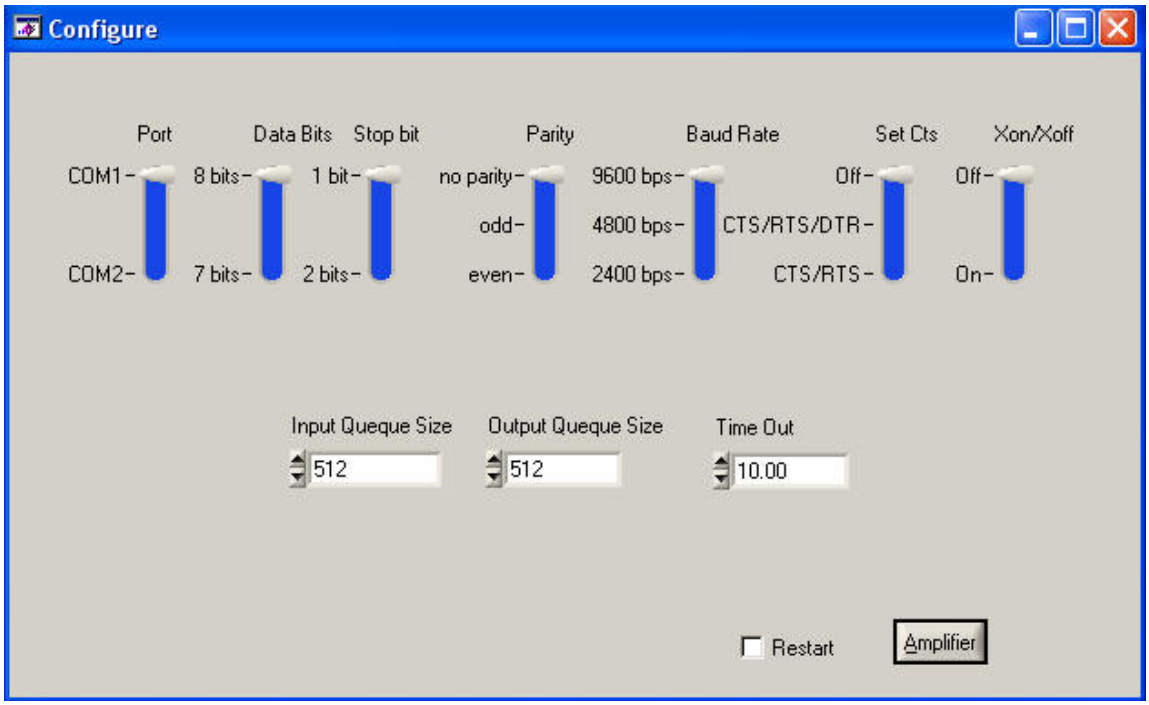

Fig. 5.9:Settings of the RS 232 parameters for the remote control

The option *Restart* allows to send a command to switch the amplifier; this command is executed by pushing the command button *Amplifier*; This command sets the RS 232 parameters, activates the reading of the amplifier status and its settings and displays the Amplifier panel.

On this panel the led *remote* and *power* indicates the state of the device and the other numeric buttons, which we will explain in more details, indicate its settings.

For each channel it is possible to specify the *sensitivity* of the connected sensor and the desired *output sensitivity*; it is the amplifier that operate an automatic setting of the gain of the operational amplifier of both input and output stage to perform the realise the transduction that is set.

For each channel it is possible to set the cut-off frequency of the low-pass and high-pass filter that act on the input signals.

The options *Input floating* and *Output Floating* allow to choose the single ended or the floating mode for the both the input and output of the preamplifier; the options *Correction* allows to set a factor to correct by software the gain of the channel. These commands are possible for each channel.

For the first three channel, on which the accelerometers are connected, an automatic test is possible to decide if the sensor is well mounted. The preamplifier excites the accelerometers with a vibration signal at a frequency which is possible to indicate with the numeric button *Impulse frequency.* The test determines the resonance frequency of the combination accelerometer-base onto the device is mounted. The parameter *impulse frequency* is chosen equal to the mounted frequency of the accelerometer so that if the accelerometer is well mounted the *resonance frequency* computing by the automatic test should coincide with the mounted frequency as explained in the paragraph 3.1.2. If the impulse frequency and the resonance frequency are very far, the mounting of the accelerometer is not good.

The channel 4 is for the microphone; this is a delta Tron channel, that is, the preamplifier can supply the device connected on it. The supply can be a current source or a voltage source and it is possible to set it by the options *Supply* and *Delta Tron Voltage*; for the preamplifier 2671 the supply is a 4 mA current source without Delta Tron voltage; for this channel it is possible to set the length of the cable (*cable length*) used to connect the device to the preamplifier to establish if the current source chosen is enough; an eventual problem is indicated with an overload condition.

The selection of each option described above generate a call to the routine to send the specified command or setting to the preamplifier.

For each channel there is an indication of the *overload* conditions whose check is enabled; the *code status enable* indicates which bit of the status word has to be checked when a control of the status amplifier is required. The code *255* enables the check of all the bits of the word. The tab. 5.1 shows the word status and the code for each overload condition.

Word	Control condition	Code
00000000	No control	0
00000001	Input common mode	1
00000010	Output common mode	2
00000100	Transducer Voltage	4
00001000	Signal overload	16
11111111	All	255

Tab. 5.1: Status word

- Input/Output common mode overload: if the input and/or output floating mode is selected, the potential difference between the ground of the preamplifier and the ground of the device, to which it is connected, must not exceed ±5 Volt. This overload condition does not mean that a distortion of the signal occurred if the maximum amplitude signal is less than 10 Volt.
- Transducer voltage overload: this is an indication for the Delta Tron channel; for this channel the signal oscillates around a DC offset of 12 Volt due to the polarization supplied by the preamplifier. If the signal is not limited in the range 3V-21V, the overload indication occurs.
- Transducer current overload: This is an overload indication for the Delta Tron channel; it indicates that the current source is not enough for the selected length cable.
- Internal Signal overload: It indicates a signal overload occurred in the internal stages of the preamplifier.

By pushing the command button *Check overload* with the *code status enable255* all the overload condition are controlled and it is possible to read the status of the preamplifier through the led and the code overload independently for each channel. If the led is *green*, no overload condition occur and the displayed code is *0* ; vice-versa the led is red and the code number indicates the overload conditions; i.e. the code number 17 means that both an internal signal and input common mode overload happened. The command *Refresh panel* generates a call to a routine to read the status and the settings of the preamplifier to check if the commands, previously sent, were correctly actuated.

The button *Send* sends the command typed in the text box *Send Command;* it can be used to send to the preamplifier those commands for which there is not a direct call associated to a dedicated button. The command *SendRead* has the same function but it is used for the query; it sends a query to the devices and wait for the answer which appears in the text box *Read*; the button *ClearBox* deletes the content of the text box *Read.*

On the right of the panel there is a section dedicated to the check of the battery of the device.

It is possible to switch on the circuit for the charging of the battery and then the led becomes *green;*

Charge Time Left indicates the remaining time to complete the charge and *Cycle count* indicates the number of times that the battery was charged. When the battery is charged, *Capacity Left, Battery time left* and T*ime Alarm* indicate the status of the battery, which is updated by pushing the command button *Refresh Status Battery.*

5.4 Remote Control of Sylvac capacitive gauge

The remote control is also possible for the Display unit D90 too; it is noted that an independent software was developed for this device because, as anticipated in the chapter 3, it performs a measurement of the jaw position that is not strictly correlated with the vibration measurement executed to study the impact of the beam proton on the collimator.

In the Fig. 5.10 is shown the panel to control the data taking and the settings of the device. As for the remote control of the B&K preamplifier, the first operation to do is the setting of the RS232 parameters; by pushing the command button Configure the panel in the Fig. 5.11is displayed where it is possible to set the COM port, the baud rate of the communication, the parity control, the stop bits, the length of the data, the size of the input and output queue, the timeout limit for I/O operations, the CTS mode and the X mode; for the description of this parameters see the paragraph 5.3. By pushing the command button *Close* the parameters for the RS 232 communication are saved, the acquisition of the settings of the device starts and the main panel is displayed. Form this panel it is possible to lock the keyboard of the device, to select the resolution (from 0.0001 mm to 0.1 mm), the unit of measurement, the mode of measurement, (Norm: display the current value; Max: display the value acquired only if it is the maximum; Min: display the value if it is the minimum.

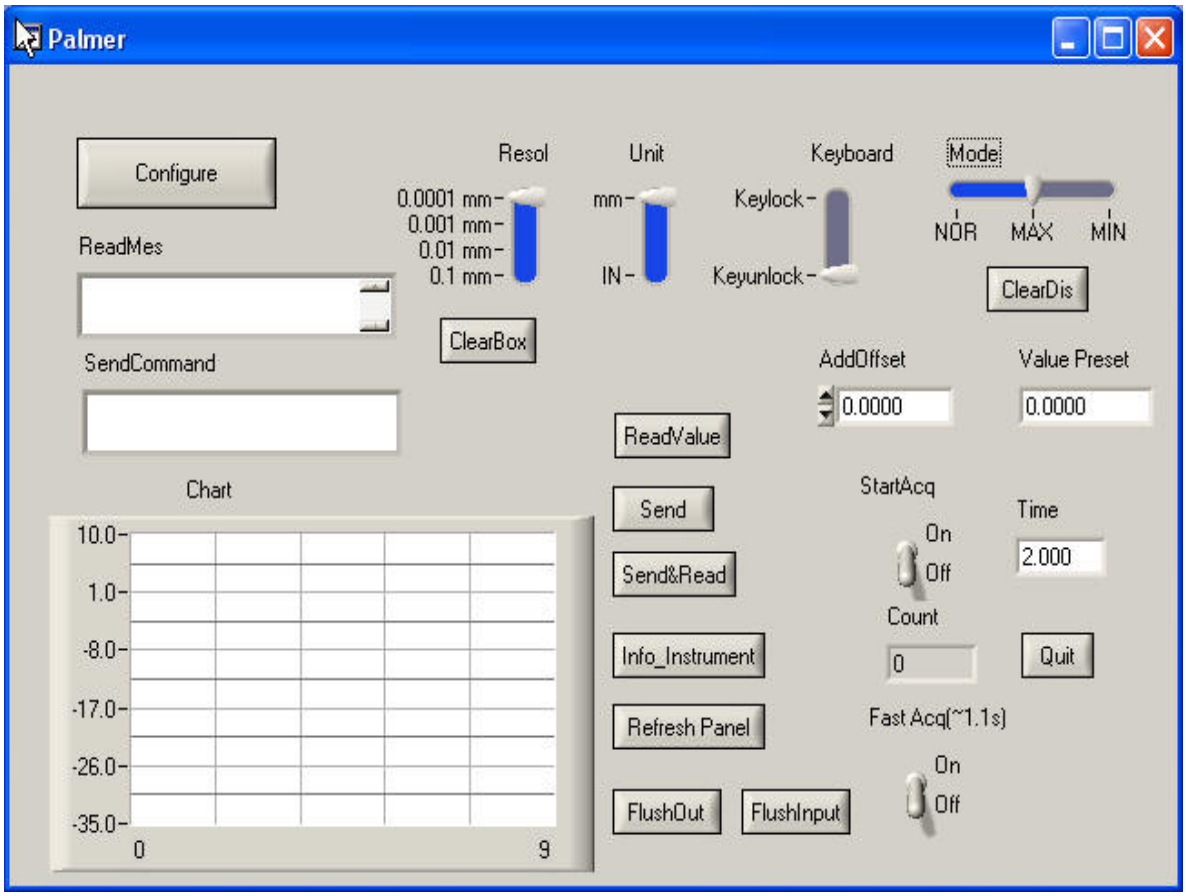

Fig. 5.10:Panel for the data taking and acquisition settings of the palmer

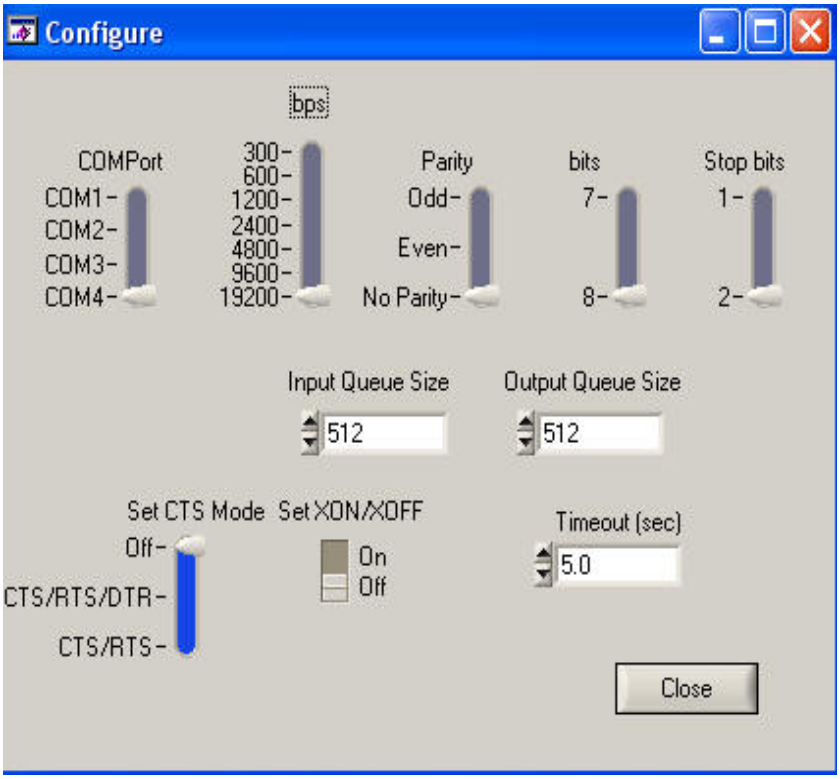

Fig. 5.11: Configure panel for the RS232 remote control

The command *Clear Dis* reinitializes the registers when the unit is in *max* or *min* measurement mode. By using the numeric button *Value preset* it is possible to memorize a preset value; this option may be used for zeroing operation. For the commands described above, the changing of any settings generates a routine to send the commands to the device. The numeric button *Addoffset* permits to correct the acquired value by adding an offset.

The command button *ReadValue* operates the printing of the read value and saves it in a file; the switch *Start Acquisition* activates a continuous reading of the data each Δt time interval specified in *Time*; the box *count* memorizes the number of readings executed; the switch *Fast Acq* performs a continuous acquisition at maximum speed allowed by the resolution selected. The button *Send* sends the command typed in the text box *SendCommand;* the button *Send&Read* is used for sending a query to the unit. The command button *Info_Instrument* reads the settings of the device and shows them in the text box Read Message; the button *Refresh Panel* executes the same operation and updates the panel; they are useful to check if the commands, previously sent to the device, did not fail. *Clear box* deletes the content of the text box *ReadMes*. The command button *FlushOut* and *FlushInput* empty the output and the input queue respectively.

5.5 Analysis 3D

This software application was developed to compose in three dimensions the signals in output from the accelerometers mounted on the same point along different directions. It allows individuating the vibration directions due to the beam impact. If the measurements show a repeatability of the vibration directions, this analysing method may be the right way to follow to study the acquired data. First the signals must be properly filtered to delete the frequency components which are not interesting. The figure below is the main panel where it is possible to select the files (*Select File*) of each channel mounted in the same point and the file of the microphone data to compare the time interval of the phenomenon. The command button *Scale* with the numeric buttons *Xmin, Xmax, Ymin* and *Ymax* allows to zoom on the interesting part of the signals. For each graph the number of the channel and the correspondent sensitivity(V/ms^{-2}) are indicated. By pushing the button *Save* the data acquired referred to the time interval specified by *T_start and T_end* are saved in new short files for the following analysis.

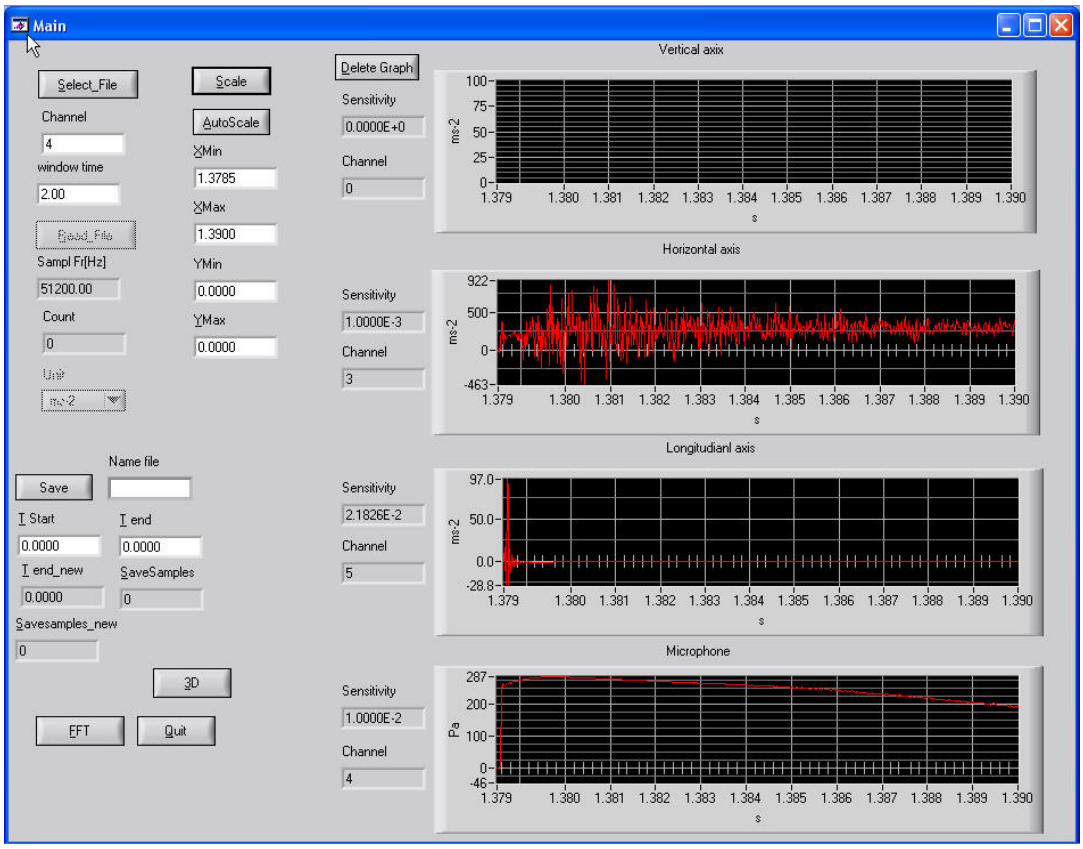

Fig. 5.12: Main panel

By pushing the button FFT the panel shown in the Fig. 6.56 is displayed; on this panel it is possible to modify the signals; in particular the signals is filtered in according with low frequency limit and the high frequency limit selected by panel (*Low limit-High limit*). The command button IFFT computes the filtering operation specified and the graph InvFFT shows the plot of the original signal and the filtered signal. The filtering operation allows to isolate the frequency components that are not interesting to delete them. Indeed, it is possible to save the modified signal. In the example in figure, the filtered signal represents the low frequency harmonics of the original data to delete their effect on the waveform in the time domain. The button *Compare Channel* allows to display (Fig. 6.57) more channels on the same graph to study a possible correlation between the accelerometers mounted along the same directions but in different points. By pushing the button 3D on the Main panel, the following panel is displayed (Fig.); here it is possible to load the data which have been modified in the previous section to study the vibration in 3 dimensions. The data are quantized and plotted on the 3Dgraph; the *colorscale* is based on the maximum level of the accelerometer mounted along the vertical position. The text box *Info* shows the main information for the data loaded. The 3D plot can show the vibration directions induced by the beam impact.

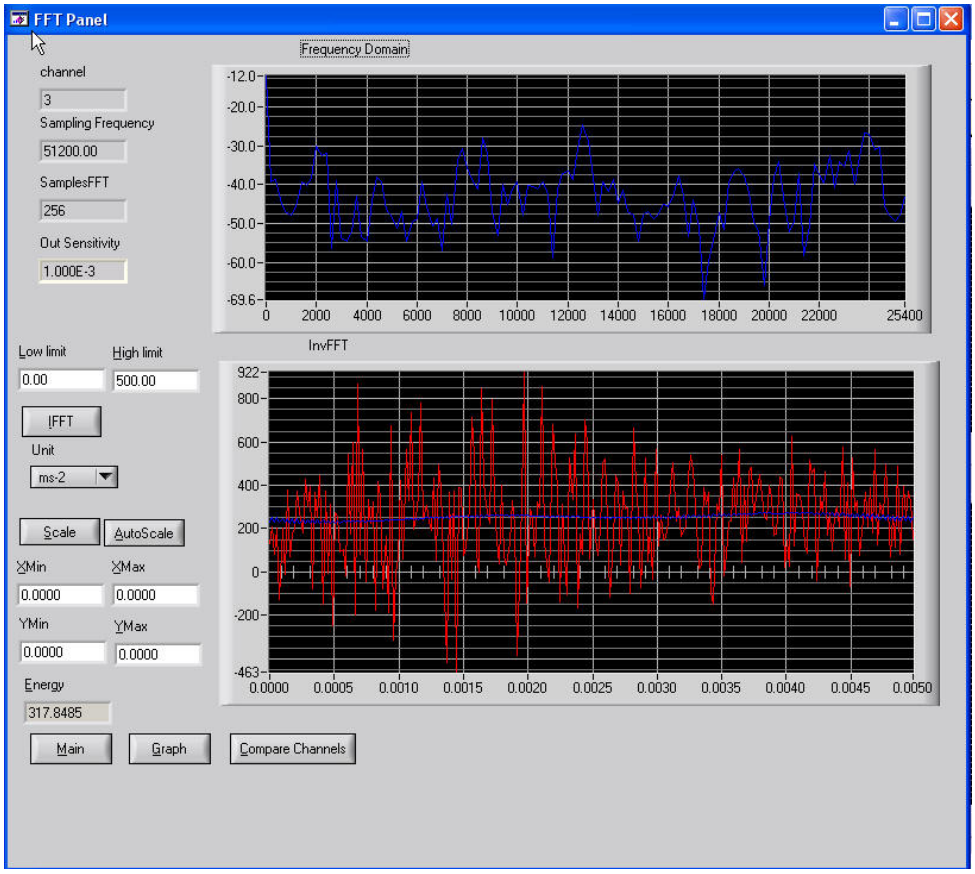

Fig. 5.13: Original signal and filtered signal

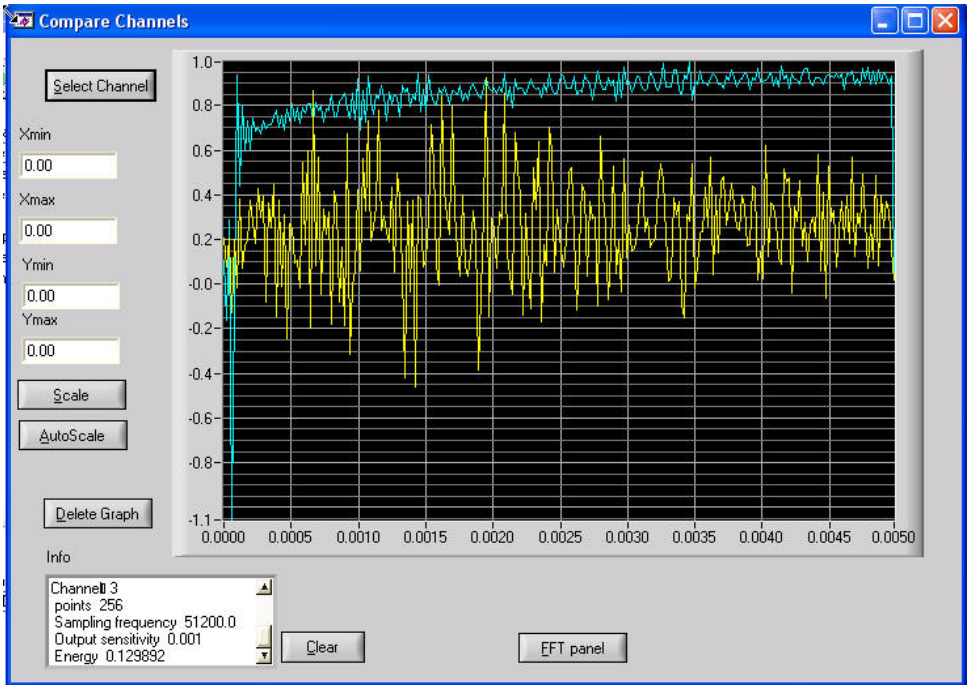

Fig. 5.14: Compare Channel Panel

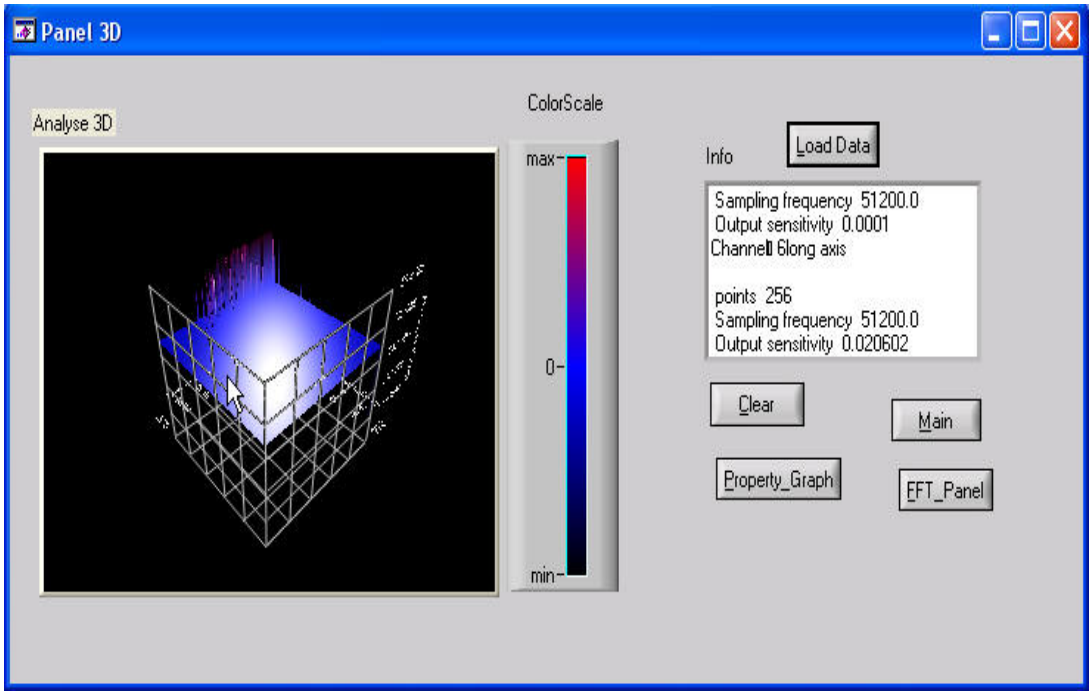

Fig. 5.15: 3D view of the accelerometer data

6 ROBUSTNESS TEST AND ANALYSIS DATA

The robustness test was planned on the 25th October 2004 but it was interrupted because of a technical problem occurred in the system for the extraction kicker of the beam from SPS ring to the line TT40. The test was repeated successfully on the 8th November 2004; on the 7th November 2004 we performed a set of measurements at low intensity. In the following paragraph we describe in more detail the acquisitions executed during these three nights.

6.1 1st Robustness test

Noise analysis without beam

Before starting the test, we executed some acquisitions at the sampling rate 25kS/s to test the remote control of the preamplifier and the data acquisition system. The figures below show the waveform of the signal acquired that is mainly noise. In the legend the last abbreviation indicates the position of the accelerometer: first letter is the jaw, L for left and R for right; the second letter is the side, D for downstream and U for upstream; the third letter is the direction, L for longitudinal, H for Horizontal and V for vertical (see tab. 3.1 and fig. 3.2 for the installing scheme of the sensors).

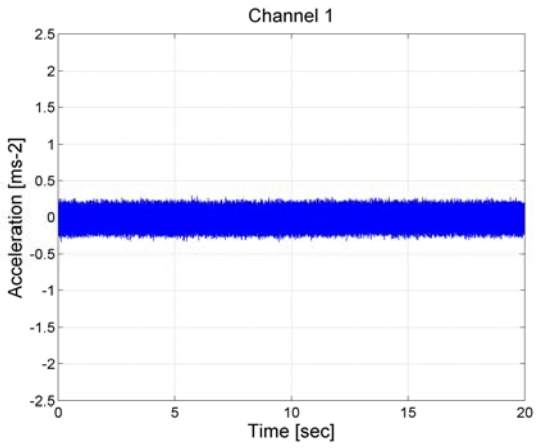

Fig. 6.1: B&K 2273AM1 LDV

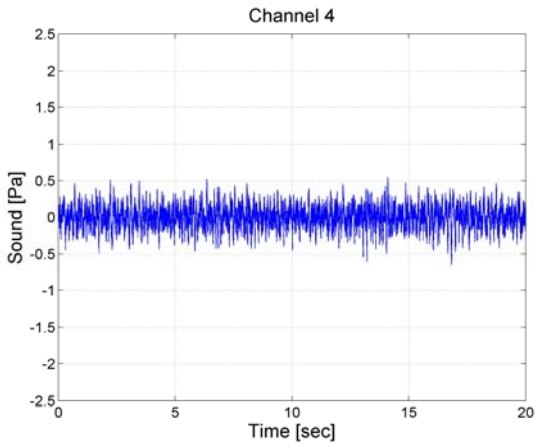

Fig. 6.2: Microphone

During this acquisition, the extraction of the proton beam in TT40 was not executed but the magnet of the extraction line were powered like if the beam was extracted.

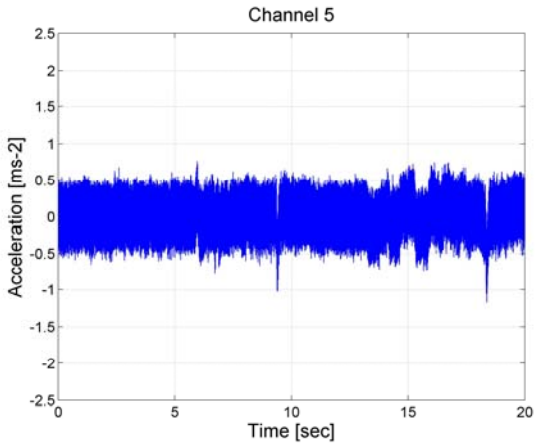

Fig. 6.3: AP40 LUL

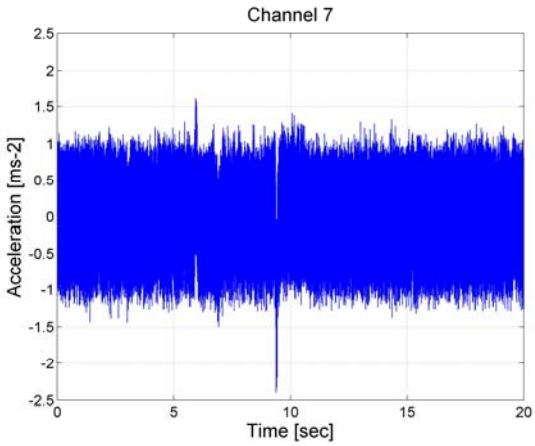

Fig. 6.4: AP37 RDL

The output signal waveforms of the accelerometers B&K are very similar. The output signal waveform of the AP accelerometers presents a strange peak every regular time interval of 28.8 sec. which corresponds to the SPS cycle time. This feature is strange and it is perhaps due to the influence of the current supply for the quadrupole magnets in TT40, which are activated even if there is no extraction in the transfer line. These signals have been analysed in the frequency domain. The FFT is computed with sampling rate 25 kS/s on 4096 points and the figures represents the medium spectrum obtained by performing 120 averages. The power spectrum density is referred to the signal converted in ms^{-2}. It is noted the noise level of the sensors is increased after the installation. The peaks are regularly present at the frequency n*50 Hz as we can note in the figures below which represent the medium spectrum of the channels 1, 4, 5, 7. The output signal of the microphone (Fig. 6.6) is less affected by the noise of the power supply; this is interesting above all if we note that both the microphone and the accelerometer 1 are connected to the same amplifier but with two different kind of cable: a special cable for piezoelectric sensor was used for the accelerometer 1 and a coaxial cable was used for the microphone. The special cable that connects the accelerometer to the charge converter does not provide a valid shield to the external noise. This is only a hypothesis that we could not demonstrate.

Beam on TED

The first operation to do on the collimator is the set-up and optimization of the collimation system which is based on the measurements from Beam Loss Monitors (BLM) which will be installed near the collimator.

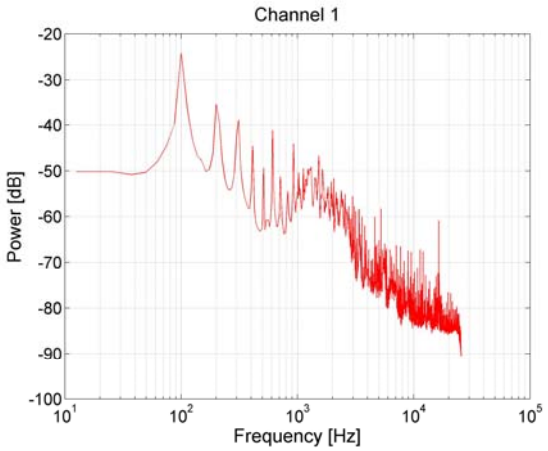

Fig. 6.5

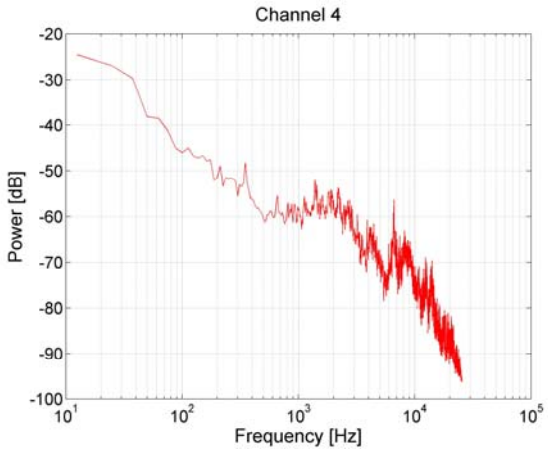

Fig. 6.6

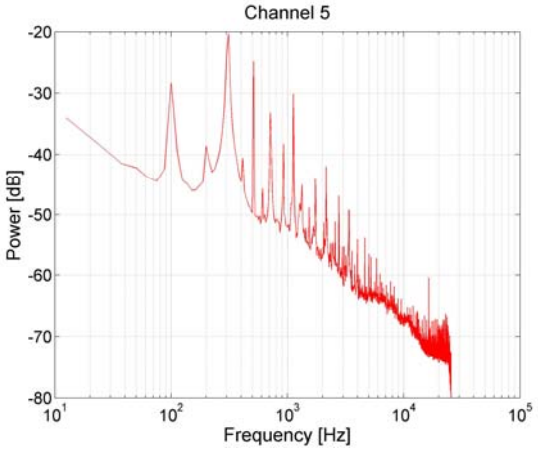

Fig. 6.7

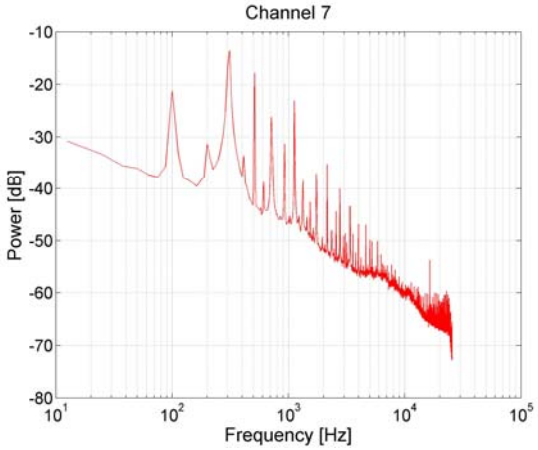

Fig. 6.8

The two ends of each collimator jaw are moved until the beam edge is touched (witnessed by a downstream beam loss signal). This step defines an absolute reference position and angle for each jaw. To perform this setting the proton beam is extracted in TT40, goes through the collimator and then it hits the TED, a target 5 metre downstream of the collimator. We performed different acquisitions for which the microphone registered the sound due to the beam impact on the TED; the beam is composed of 1 x 48 bunches ~ $8x10^{12}$ # p; it is not high intensity.

The output of the accelerometers also presents a peak which is coherent in time with the one of the output microphone. It is due to the vibration induced on the accelerometer by the wave sound; the level of the peaks is not equal because of the different installing position of the accelerometers. The figures below show the output waveform of different kind of accelerometers.

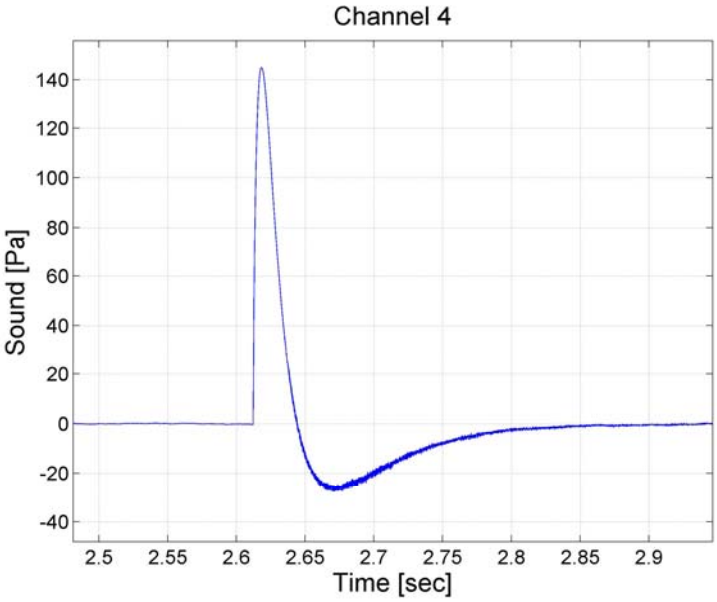

Fig. 6.9: Microphone: Beam on TED

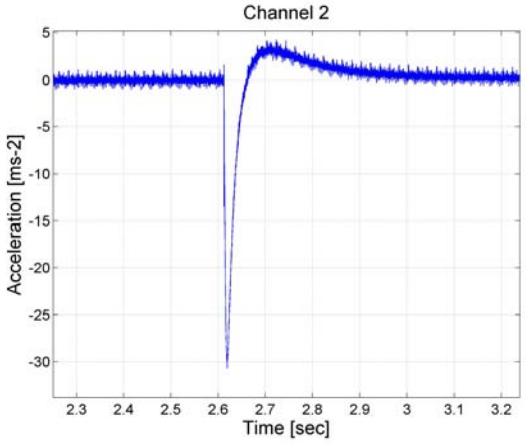

Fig.6.10

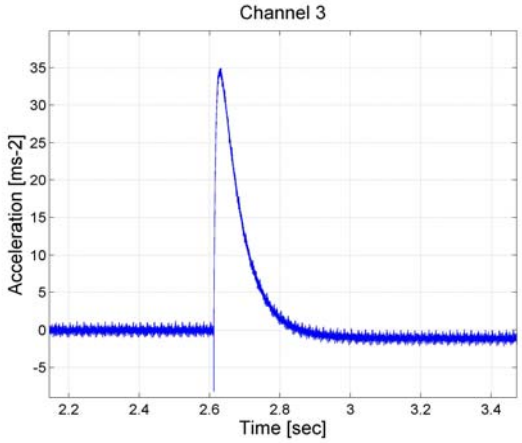

Fig. 6.11

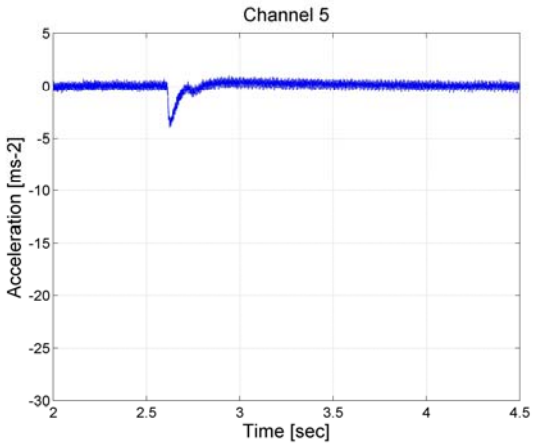

Fig. 6.12

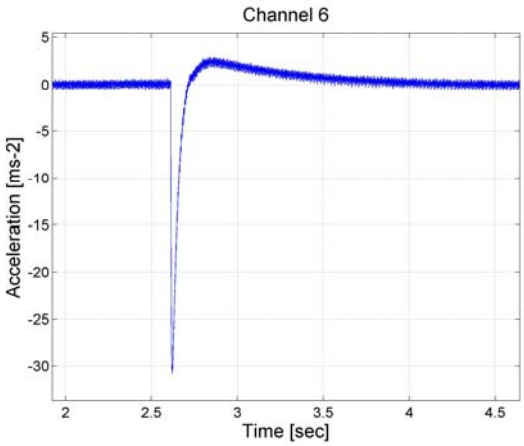

Fig. 6.13

The absolute value of the channels 2 and 3 are nearly the same; we expected that the channel 5 and 6 would have presented a similar behaviour because of their installing position (see sec. 3.1.2). However, the output signal of the accelerometer connected to the channel 5 (Fig.6.12) presents a waveform with a level peak less high than the others. The lower peak level of the channel 5 may be due to its installing position but it is more probable that it is not properly connected to the cable. Similar problem with this sensor were found during the test-bench.

As we anticipated above at 11:30 PM a technical problem occurred. The proton beam is extracted from SPS to TT40 thanks to a magnet which produces a field that modifies the trajectory of the particles; during an extraction operation the power supply of the magnet decreased its maximum value for around 5 ms; due to this defection, the trajectory of the beam was not properly deviated and it created a hall in the vacuum tank. The damage was such that it was not anymore possible to perform the test.

6.2 Low intensity test

On the 7th November, a test at low intensity was executed; the proton beam is extracted from SPS, goes through the collimator and then it goes away in the transfer line. The goal of this test, performed by another team of the collimation group, was to study another technique for the alignment operation of the collimator, based on the measurements of the deviation angle of the jaws. We participated to this test to acquire data at low intensity. We performed more than 20 acquisitions and a huge amount of data has been saved. Now we show the results of two acquisitions which respectively represent the waveform of the signals when the proton beam hits the right jaw and the left jaw. The figures below are referred to the impact of the beam on the right jaw (Fig. 6.14-6.17).

In this case the estimated impact parameter is less than 1 mm and the beam intensity is around 3.4 x 10^{10} #p. The accelerometers of the left side do not present any peak except the B&K 2273AM1 (Fig. 6.14) and the AP40 (Fig. 6.16), both mounted onto downstream side; the peak level of these two sensors is much less than the peak level of the waveform of the output signal of the AP37 accelerometers (Fig. 6.17) which are installed on the right downstream side. The waveforms are affected by an exponential decay. When the beam hits the left jaw, even if the intensity beam is not high (4 x 10^{10} #p), the estimated impact parameter is 3 mm

and thus this value is significant as we can see from the waveform of the output signals of the sensors.

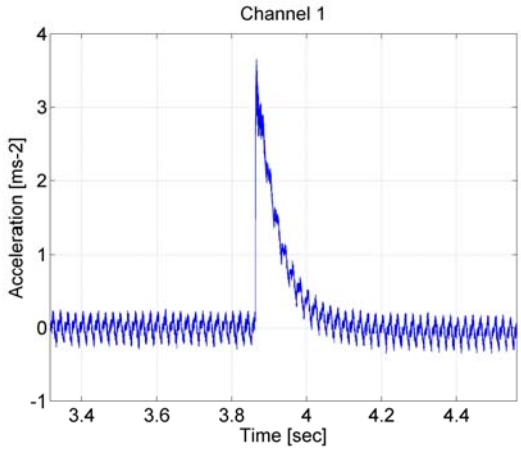

Fig. 6.14

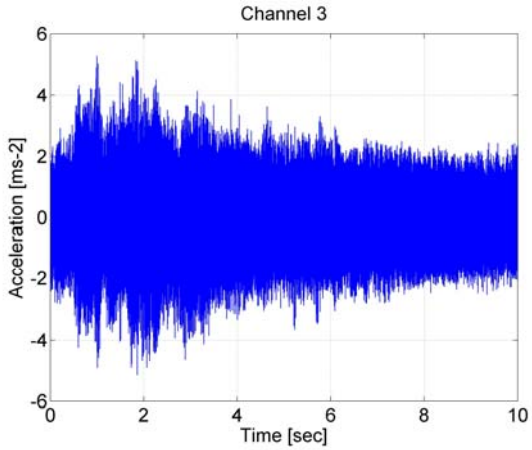

Fig. 6.15

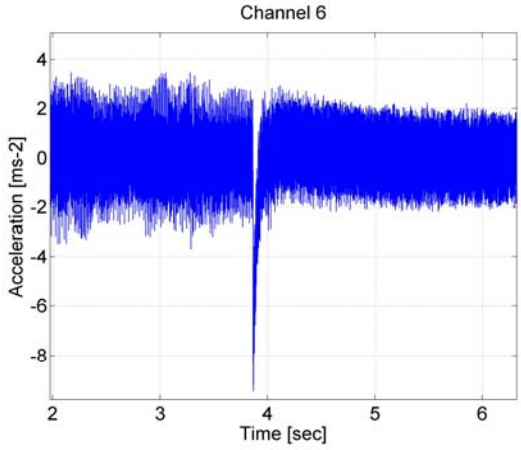

Fig. 6.16

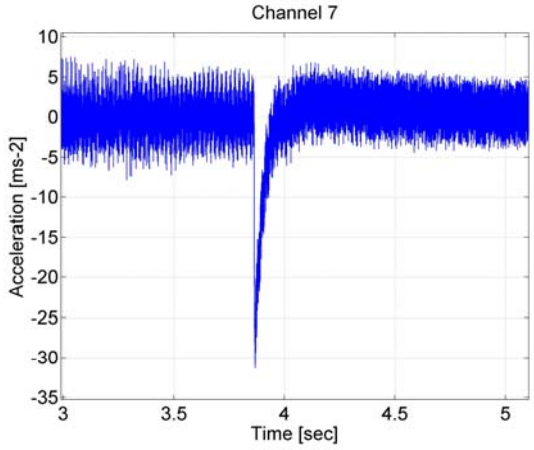

Fig. 6.17

Even if the AP37 accelerometers were mounted onto the right side and the proton beam hit the left jaw, they registered a high peak level (Fig. 6.22, 6.23). This is not so strange if we consider the accelerometers are not directly installed onto the jaw but on a steal block which is mounted onto the table moved by the stepper motors, via a roller screw/nut. About the accelerometers of the left side, it is interesting to note the peak level of the sensors installed on the downstream side is regularly higher than the ones presented by the accelerometers on the upstream side (compare Fig. 6.18 with 6.19 and Fig. 6.20 with 6.21). By comparing the figures of these two acquisitions, we can note a dependence of the peak level of the waveform with the impact parameter; however the meaning of the waveform and of the exponential decay, which is always present in the second acquisition, is not clear (see paragraph 6.3).

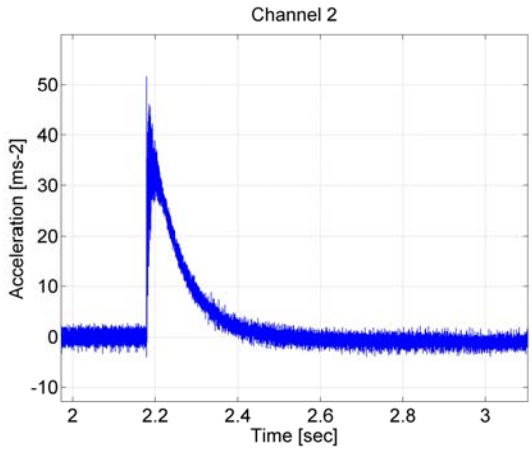

Fig. 6.18

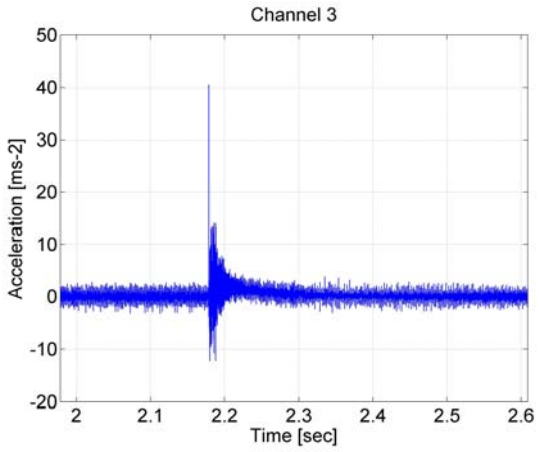

Fig. 6.19

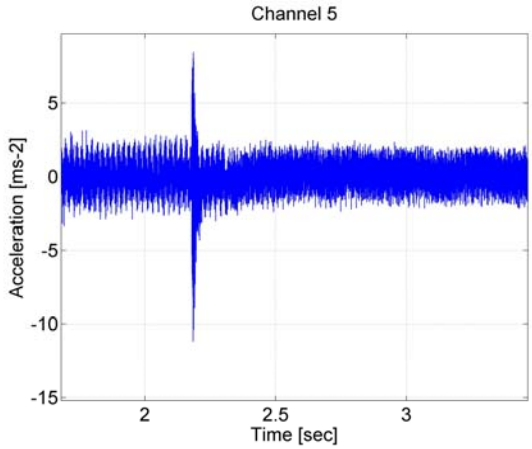

Fig. 6.20

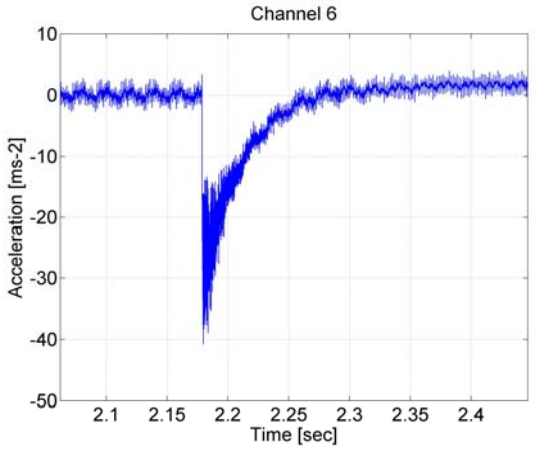

Fig. 6.21

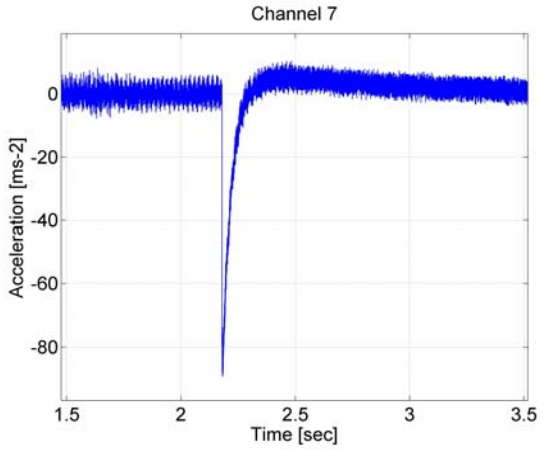

Fig. 6.22

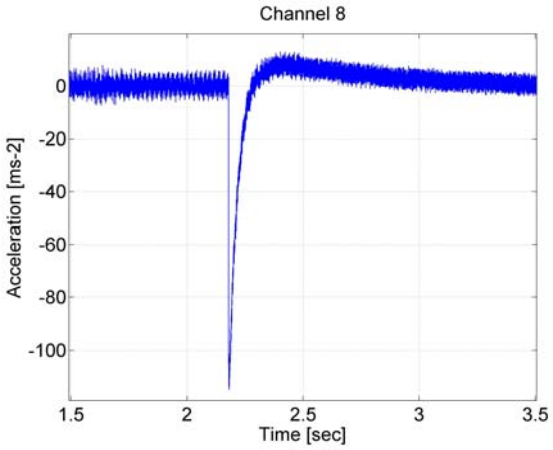

Fig. 6.23

6.3 2nd Robustness test

The robustness test was performed between the 8th and the 9th November; the Tab. 3.4 (Chap 3) remembers the most important acquisitions performed. The sampling rate is 51.2kS/s; this value has been chosen in according with the frequency response of the accelerometers (flat frequency response up to 20 kHz Fig. 3.10) and with the cut off frequency of the filters selected on the NEXUS preamplifier (0.1 Hz for the high pass filter and 22.4 kHz for the low pass filter).

Microphone

The figures below represent the waveform of the output signals of the microphone when the beam hits the jaws at the maximum intensity (4 x 72 bunches ~ 3 x 10^{13}# p). The transverse impact parameter is 4 mm; when the beam hits the right jaw with 5 mm impact parameter the signal is saturated due to the gain 100 mV/Pa which resulted too high, thus the Fig. 6.25 shows the output signal for 4 mm impact parameter, obtained by setting the gain 10mV/Pa. The waveforms are similar and the peak levels are close.

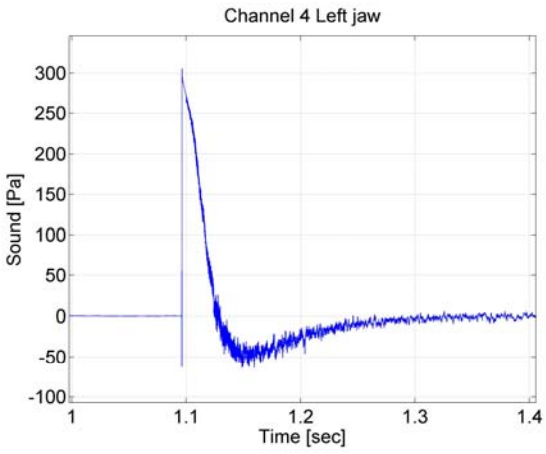

Fig. 6.24: Beam onto left jaw 4mm impact

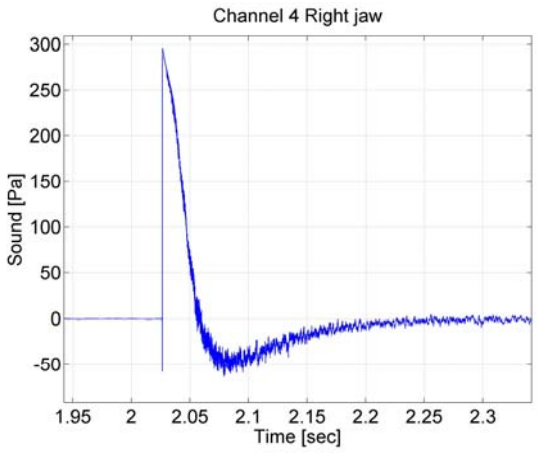

Fig. 6.25: Beam onto right jaw 4mm impact

The Fig. 6.26 and 6.27 represent the microphone signal when the beam hits the TED; it is noted that the amplitude signal is less in respect to the beam impact with one jaw of the collimator.

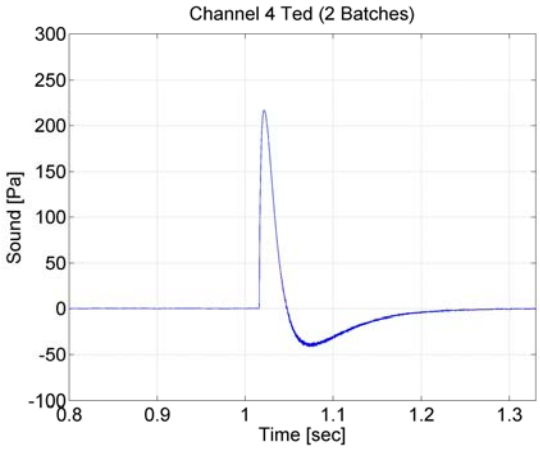

Fig. 6.26: Beam onto TED 2 x 72 bunches

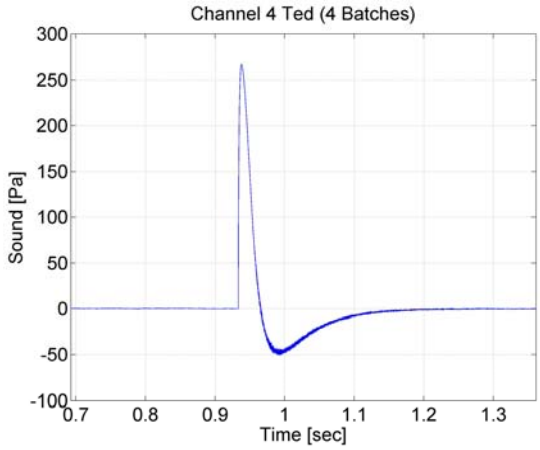

Fig. 6.27: Beam onto TED 4 x 72 bunches

The volume (loudness) is determined by the sound pressure p (Pa) and expressed as sound pressure level L_p in dB-SPL (Tab. 6.3).

$$L_p(dBSPL) = 20 * \log \frac{p}{p_0} \qquad \text{(Eq. 6.1)}$$

where p_0 corresponds to 0.00002 Pa.

Description	Sound pressure (Pa)	Sound pressure level (dB)
TED 2 x 72 bunches	222	140.9
TED 4 x 72 bunches	267	142.5
Right jaw 4 x 72 bunches 4 mm impact parameter	295	143.4
Left jaw 4 x 72 bunches 4 mm impact parameter	305	143.7
Left jaw 4 x 72 bunches 5 mm impact parameter	315	143.9

Tab. 6.1:Conversion sound pressure to Sound pressure level (dB)

The following graphs are significant; they show the increasing of the peak amplitude signal of the microphone as a function of the impact parameter when the beam is put on the jaws of the collimator. There is a strange behaviour only for the collision on the left jaw with

6 mm impact parameter; this abnormal condition is shown by the accelerometers and by the temperature sensors too (see next section).

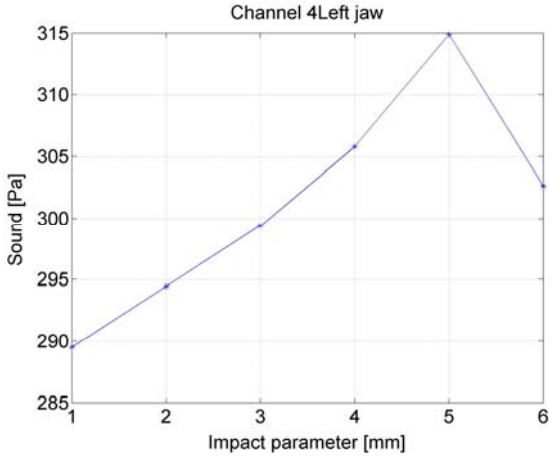

Fig. 6.28

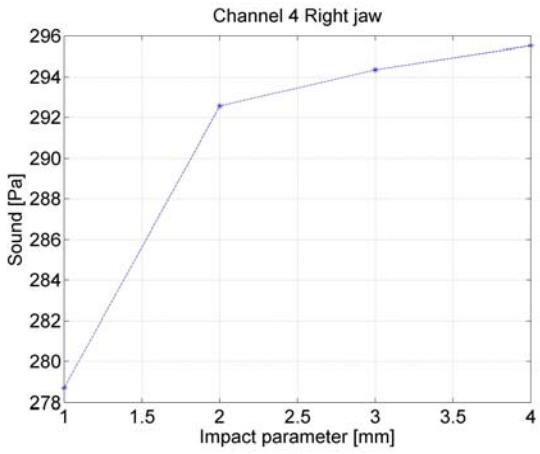

Fig. 6.29

Accelerometers

The accelerometer signals present a waveform similar to the one of the signals acquired at low intensity. When the proton beam hits one jaw, the signals present an oscillation which may be seen as a vibration of the collimator structure (Fig. 6.36). However this oscillation is not centred on the zero because of the sharp going up and the exponential dump. As for the microphone, the figures below show the absolute value of the peak levels due to the beam impact on the left jaw of the collimator.

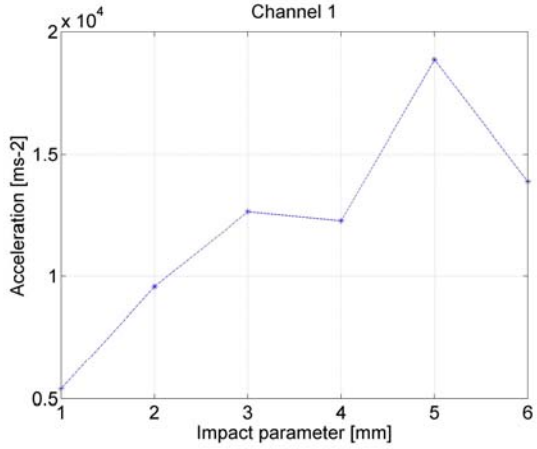

Fig. 6.30: Absolute value of the peak level (Left jaw impact) [LDV]

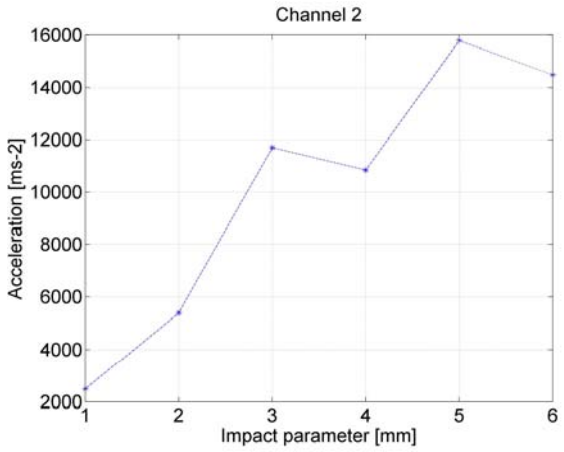

Fig. 6.31: Absolute value of the peak level (Left jaw impact) [LDH]

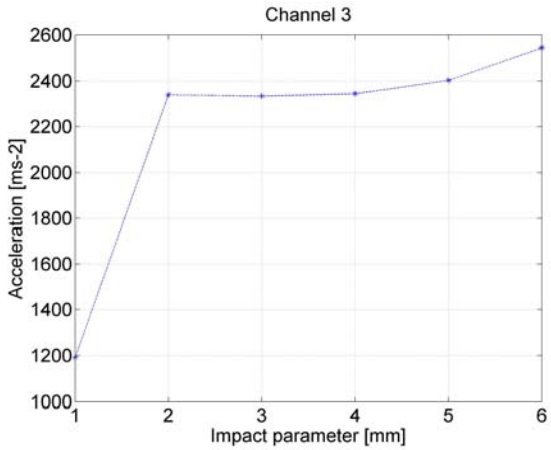

Fig. 6.32: Absolute value of the peak level (Left jaw impact) [LUH]

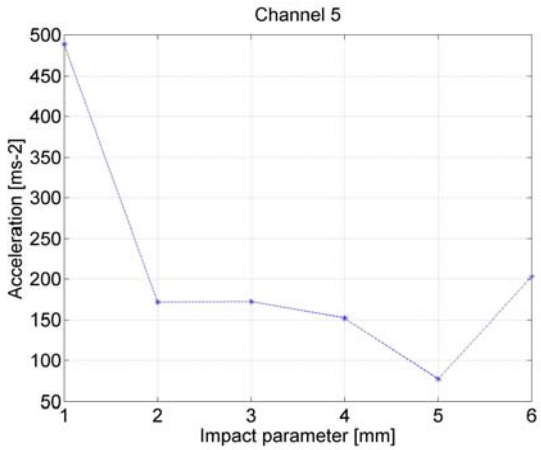

Fig. 6.33: Absolute value of the peak level (Left jaw impact) [LUL]

By analysing these graphs, in same case the peak levels are not strongly correlated with the transverse impact parameter, there is not a regular trend, above all for the AP accelerometers. This stuff is not completely clear because we expected an increasing of the peak level in according with the increasing of the impact parameter. However, the temperature sensors show a similar phenomenon; the following figure shows the local increasing of temperature of the left jaw due to the beam bump. In particular this sensor was installed on the upstream side of the left jaw. This is the only temperature sensor which survived at the test at the intensity of 4 x 72 bunches. It is noted that the temperature variation for 6 mm impact is less than the one for 5 mm impact. This abnormal condition is presented by both the accelerometers 1 and 2, and by the microphone too (see Fig. 6.28).

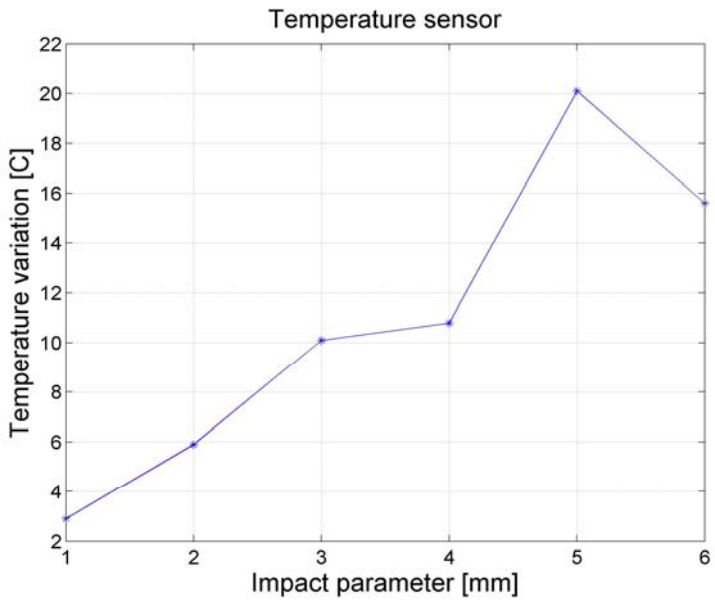

Fig. 6.34

If we compare the output signals of the channels 2 and 3 onto which are connected the same kind of accelerometer (B&K 2273A), mounted along the same directions but one on the downstream side (channel 2) and the other (channel 3) on the upstream side, we can note the going up of the channel 2 (Fig. 6.35) gets to an amplitude around ten times higher than the one of the channel 3 (Fig. 6.36). It is noted that this characteristic is common to all the acquisitions performed. This may indicate that the peak level is not only induced by the mechanical vibration of the jaws, but it is also due to external factors (i.e. charges produced by the impact) correlated to the radioactive environment as the influence of peak level on the waveform of the signals is stronger on the downstream side where the concentration of the loss charges is higher (Fig. 6.37).

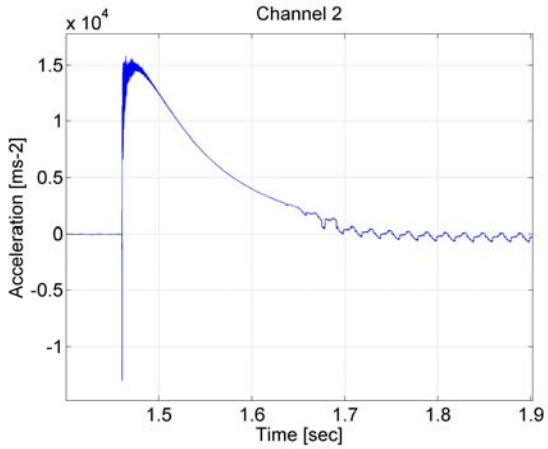

Fig. 6.35: Beam on left jaw; 5 mm impact parameter; intensity 4 x 72 bunches

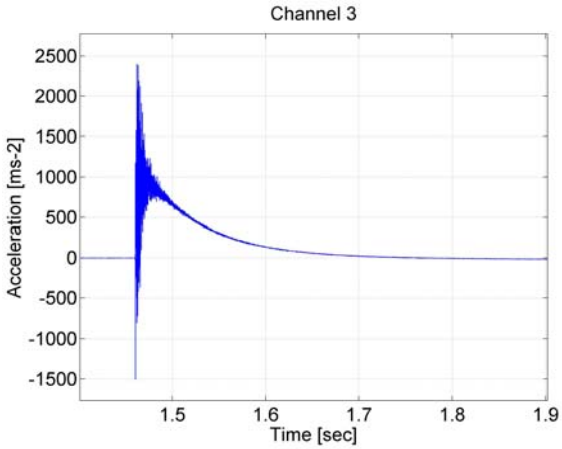

Fig. 6.36: Beam on left jaw; 5 mm impact parameter; intensity 4 x 72 bunches

The numerical evaluation of the radiation influence is not a simple matter. The following Fig. 6.37, presented by the team focused on the measurements by Beam Loss Monitor, shows the distribution of the loss charges in TT40 in the zone of the collimator.

About the exponential dump the hypothesis are two. The first hypothesis is that the exponential decay, which is around 300ms, is the consequence of a saturation condition occurred to the sensor or to the preamplifiers. This supposition is based on the following consideration: because of the sharp going up and the exponential decay the waveform is not alternating and then if we integrated twice the signal, we would obtain a net displacement of the structure which is not physically possible. The second hypothesis considers the time interval of the exponential decay the result of a mechanical time constant of the collimator

structure; it is again noted the accelerometers are not directly in contact with the jaws and between them there are other mechanical parts (clamping springs, roller screw/nut system);

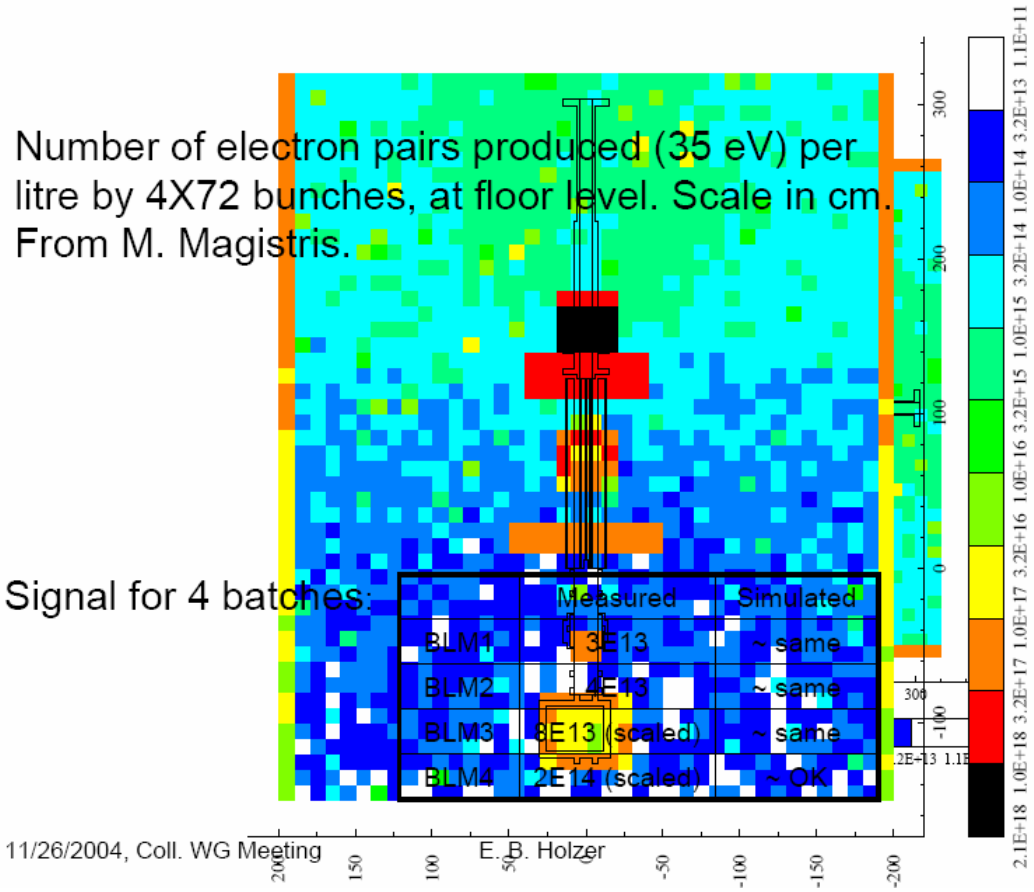

Fig. 6.37: Distribution of the loss charges measured by the BLM

thus, to establish if the exponential dump is due to the mechanical structure it is important to have a check cross with the team who is focused on the design of the collimator and above all it should be clear the influence of the radiation on the amplitude of the signal otherwise the displacement which results from the double integration of the acceleration is too higher to be physically acceptable.

Even if we consider the worst case, that is, the exponential dump is the result of a saturated signal, which seems to be the most probable consideration, we have to understand the meaning of the oscillation that we note before the decay. Such oscillation may be the structural vibration induced by the beam impact. The analysis in time domain to study the compositions of the vibration signals in 3D is not easy to perform because the AP accelerometers present a strongly saturated signal. The analysis in the frequency domain of such oscillations has been performed to understand if the frequency spectrum of such structural vibrations presents any significant change after the beam bumps onto collimator at

high intensity. The following figures show the signals in the time domain and the power density spectrum in output from the accelerometers B&K 2273A when the proton beam hits the left jaw at the intensity 1 x 72 bunches ~ 7.6 x 10^{12} # p and at the maximum intensity 4 x 72 bunches ~ 3 x 10^{13} # p.

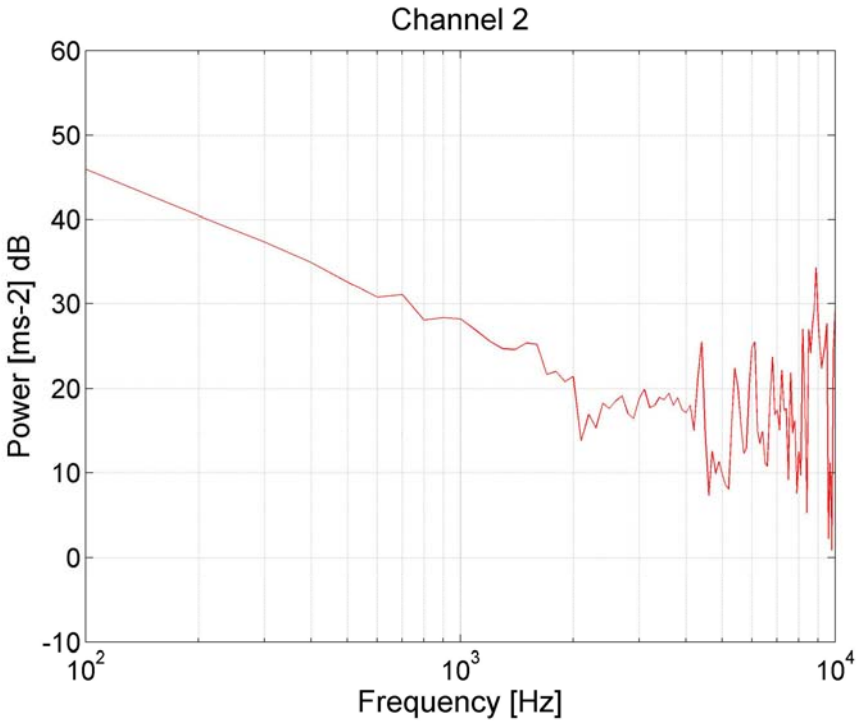

Fig. 6.38: Intensity 1 x 72 bunches 5mm impact parameter

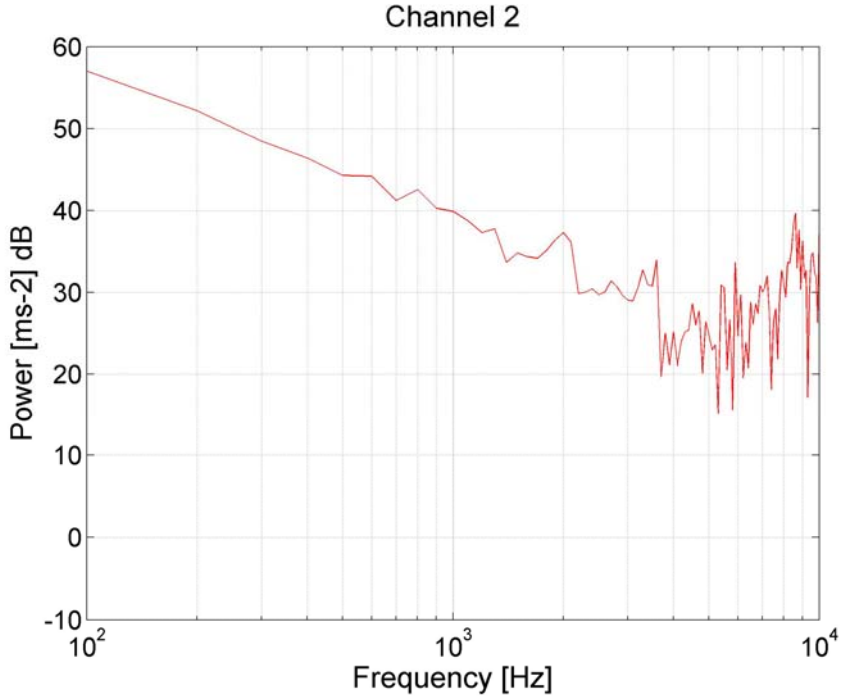

Fig. 6.39: Intensity 4 x 72 bunches 5mm impact parameter

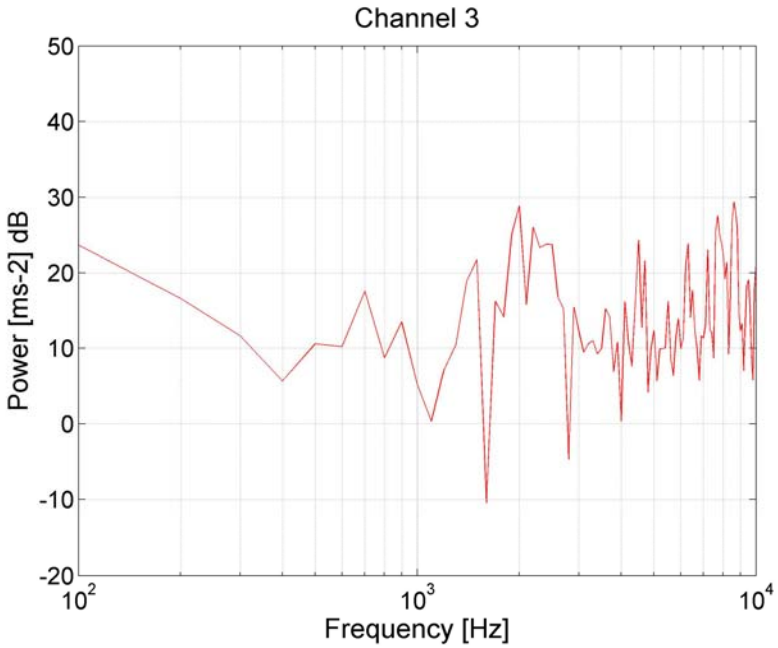

Fig. 6.40: Intensity 1 x 72 bunches 5 mm impact parameter

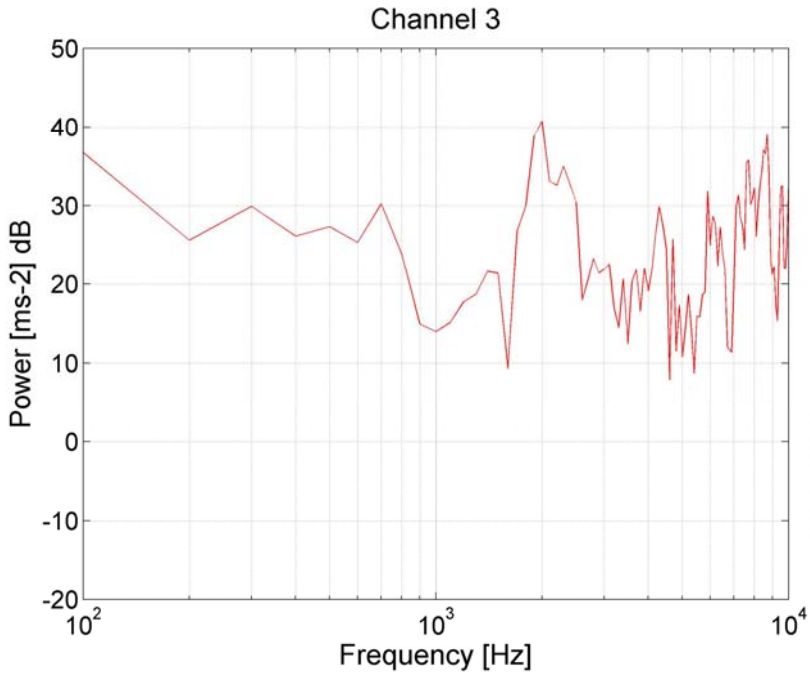

Fig. 6.41: Intensity 4 x 72 bunches 5 mm impact parameter

The decreasing trend of the power density spectrum at low frequency which is particularly evident for the channel 2 is the consequence of the exponential dump which is overlapped to the oscillation. Except the amplitude level, the FFT does not show any important change in the power density spectrum of the signals acquired after the bumps at high intensity; the main harmonics of the signal are nearly localized at the same frequency in

both the cases (1 x 72 bunches and 4 x 72 bunches). This is in according with the results of the inspection of the jaws that do not point out any significant damage of the structure. This result is important because it may demonstrate this measurement system is able to detect the mechanical conditions of the collimator. Comparisons with finite element models of the collimator will be carried out to verify if the measured vibration frequencies can have a physical origin.

Eventually the sensors installed on the collimator (accelerometers and microphone) did not have any damage. The Fig. 6.42 and 6.43 show the output signals of the accelerometers B&K 2273AM1 when the motors of the left side of the collimators have been acted; in particular the signal in the Fig. 6.42 is referred to an acquisition performed before the robustness test and the signal of the Fig. 6.43 was acquired after the test at high intensity.

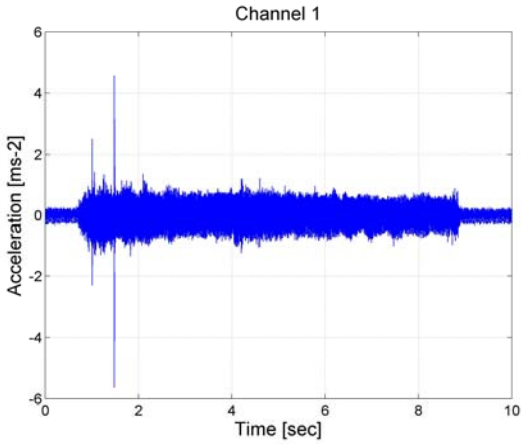

Fig. 6.42: Acquisition before the robustness test

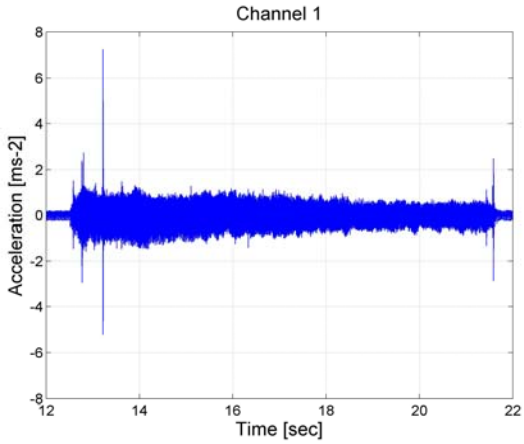

Fig. 6.43: Acquisition after the robustness test

The waveform in time domain and the FFT also are very similar. Thus, the radioactive environment did not damage the sensors and then its effect on the measurement is only a signal distortion.

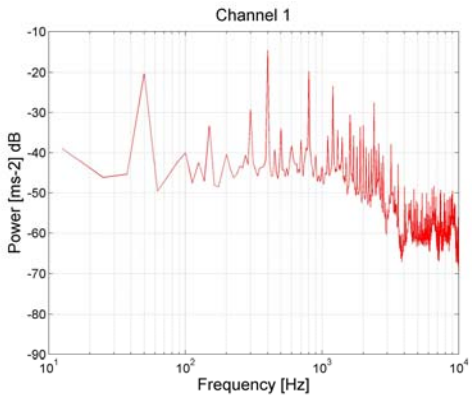

Fig. 6.44: Acquisition before robustness test

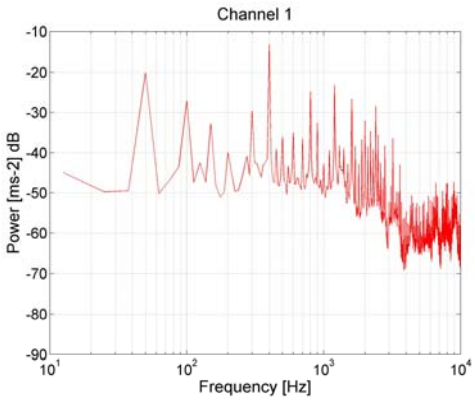

Fig. 6.45: Acquisition before robustness test

7 CONCLUSIONS

A remote data acquisition system, designed for operating in a high radiation environment, has been setup for measuring sound and mechanical vibrations induced in the LHC collimator by high-energy, high intensity proton beams. The system consisted of 7 high precision, piezoelectric accelerometers, a free field microphone, conditioning preamplifiers and a data acquisition board, 8 channels simultaneously sampled up to a maximum sample rate of 102.4 kHz. The system has worked as expected, ensuring a continuous data taking throughout the various performed measurement campaign at the TT40 transfer line. It has been demonstrate that the measurement system can detect on line the proton beam impact into the collimator. The output signal of the accelerometer show clearly when a load condition of the jaws occurred. However, for the test at high intensity or at deep impact parameter, it was not possible to individuate which jaw was involved by the bump. This depends on the fact that the accelerometers are not directly mounted on the jaws but are connected to them through a complex mechanical structure. The beam impacts are also detected by the microphone by recording the shock wave due to the impact; the waveform of the sound signal shows a trend which is in according with the increasing of the intensity beam and with the increasing of the transverse impact parameter which characterized the test performed. Following these encouraging results, the possibility of installing accelerometers to detect the beam impacts in all the LHC collimators is presently being discussed. The preliminary analysis in the frequency domain showed an encouraging result: the power density spectrum of the accelerometer signals acquired for the test at the maximum intensity (4 x 72 bunches) beam does not present any significant change if compared with the power density spectrum of the vibration signals acquired at the intensity 1 x 72 bunches. This suggests that no damage is induced by beam of this intensities and energies. This has also been confirmed by inspection of the collimator jaws, which show no apparent damage of these components. Future studies shall be focused on comparisons with the finite-element model of the collimator will have been carried out to verify if the measured vibration frequencies can have a physical origin. The effect of the radiation on the measurements of the accelerometers remains to investigate in detail.

The thesis work has also included the setup of the data acquisition system for an high resolution capacitive gauge for measuring the position of the collimator jaw. The proposed solution was based on a remote control of the sensor via RS232 connection. The system

proved to work well in the high radiation environment and ensured reliable measurements of the jaw position. The possibility of using this kind of system in the LHC is being investigated.

Bibliography

[1] O. Brüning, P. Coliier, P. Lebrun, S. Myers, R. Ostojic, J. Poole, P. Proudlock, " LHC Design Report", Volume I, "The LHC main ring" CERN-2004-003 (2004).

[2] P. Bryant and E. Klein. CERN-SL-92-40-AP (1992).

[3] L. Burnod and J.B. Jeanneret. CERN-SL-91-39-EA. LHC-Note-167 (1991).

[4] J.B. Jeanneret, "Optics of a two-stage collimation system". CERN-LHC-Project-Report-243 (1998).

[5] I.L. Azhgirey, I.S. Baishev, N. Catalan-Lasheras, J.B. Jeanneret, "Cascade Simulations for the LHC Betatron Cleaning Insertion". LHC-Project-Report-184 (1998).

[6]. Ajguirei, I. Baichev, J.B. Jeanneret, I.A. Kourotchkine and G.R. Stevenson. CERN-LHC-Project-Note-263 (2001).

[7] Instruction de securite, Safety instructions, CERN IS 23 (Rev. 2), Edms 335745.

[8] M. Brugger, S. Roesler, "Accumulated Doses during Interventions on the Vacuum System in the LHC Beam Cleaning Insertions", CERN-TIS-2003-027-RP-TN, (2003).

[9] T. Pieloni, "A scaling law for sextupole and decapole decay and snapback compensation in Large Hadron Collider ", Diploma thesis, University of Milan, (2003)

[10] R. Graham, Stevenson and Helmut Vincke, "Studies of the Dose Rate in ECA4 due to Beam Losses in TT40" CERN–TIS–2002–034–RP–TN (2002)

[11] Bruel&Kiaer "Vibration measurements" (1998)

[12] D. Formenti, T. Norsworthy, "Sound and vibration" (1999)

[13] Sylvac SA "Manual D90" (2001)

[14] National Instrument “User Manual Dynamic Signal Acquisition Device” (2001)

[15] M. Cerna, Audrey F. Harvey, “The Fundamentals of FFT-Based Signal Analysis and Measurement” National Instrument (2000)

[16] MAXIM “A/D and D/A Conversion, Sampling Circuit” (2003)

[17] ANALOG DEVICES “Sigma-Delta ADCs and DACs” (1991)

[18] D. Jarman, “A Brief Introduction to Sigma Delta Conversion” (1995)

[19] IEEE, “Standard for Terminology and Test Methods for Analog to Digital Converters”, IEEE Std 1241-2000, (2000)

[20] R. M. Gray “Quantization Noise Spectra”, IEEE Transf. Inform. Theory (1990)

[21] J. Blair, T.E. Linnenbrink, “Corrected RMS error and effective number of bits sinewave test” EWADC (2002)

[22] K. Hein, A. Pacut, “Effective Resolution of Analog to Digital Converters” IEEE Instrumentation Measurement Magazine (2003)

[23] S. Redaelli, “Calibration of the collimator motors for the SPS and TT40 prototypes” LCWG Collimation Working Group

[24] S. Redaelli, “An high resolution gauge for measuring the collimator jaw position with micrometer precision Results of TT40 measurement” LCWG Collimation Working Group

[25] S. Redaelli “Stabilization of Nanometer-Size Particle Beams in the Final Focus System of the Compact Linear (CLIC)” (2003)

[26] http://www.chenyang-ism.com/CapaSensorPosi.htm

[27] http://www.ni.com

[28] http://www.bksv.com

[29] http://www.sylvac.ch

[30] http://www.aptechnology.nl

ACKNOWLEDGMENTS

I want to sincerely acknowledge Prof. Felice Cennamo who gave me the opportunity to make my thesis work at CERN, one of the most important research centres. I would also like to thank Dr. Ralph Aβmann, chairman of the Collimation project, who supported my internship.

I want to thank very much my supervisor Dr. Stefano Redaelli. His guide always helped me and the enthusiasm, he expressed for his supervision, encouraged me a lot providing a strong motivation to do well my work. I would also like to thank Ing. Alessandro Masi for his strict collaboration; his clever suggestion and his technical support have been very precious.

I want to thank Tatiana Pieloni and Federico Roncarolo from AB/ABP group, Marco Calvi, Mirco Coccoli and Pierpaolo Granieri from AT/ATM group; they all helped me and they have been colleagues and above all friends.

I would like to thank Gabriele Greco; we start this internship together and it was very encouraging to have a friend during this new experience.

I would also like to acknowledge friends from Naples, Pierluigi, Sebastiano, Annalisa Franceso T., Francesco B., Sabatino, Dario, Luigi, Carlo, Serena, Luca, Rosario who encouraged me a lot to start this experience.

I would like to thank Gianni who has been friend for a life time.

My family always supported me during my studies, showing their deep affect. I want to thank very much my father Giuseppe, my mother Concetta and my brother Onofrio. I can always feel and appreciate their joy and approval for what I am doing. They were and will be always precious for me.

Appendix A

Successful test of the Sylvac capacitive gauge

The robustness was the occasion to verify the working of the capacitive gauge Sylvac equipped with the unit display D90. By the measuring performed, this sensor worked well.

In this section we present a significant measure performed on the 7th November, during the test at low intensity. The palmer was useful because the data acquired, by the remote software, allowed the measuring the position of the right jaw, on the upstream side, providing a check cross with the position sensors of the motors installed for the moving of the jaw.

Before starting the measurement operations the right jaw has been moved in the position of maximum opening gap; the measured value by the capacitive probe was -0.01 mm. This value represents an offset in the zero; it is noted no calibration was performed for this sensor. After executing the zeroing operation of the device, we added by software an offset of -30.585 mm which corresponds to the maximum displacement of the jaw; therefore the value 0.00 mm indicates that the right jaw is at the most internal position which is allowed.

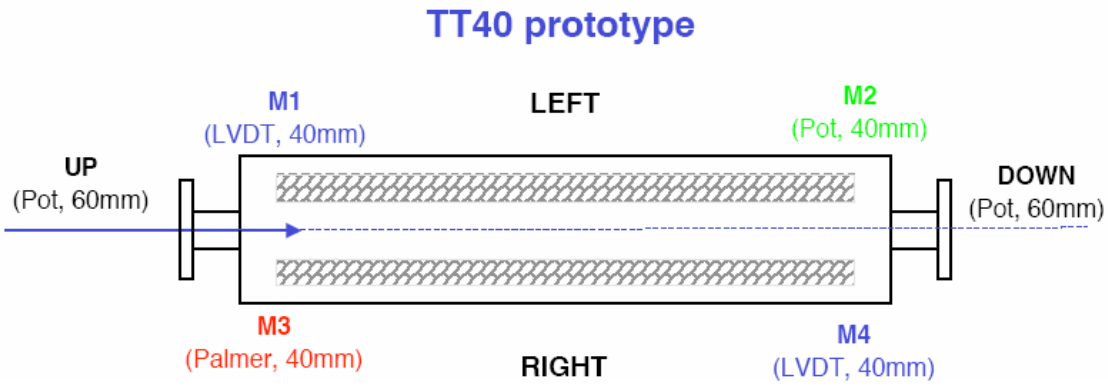

Fig. A.1: Gauge positions installed on the collimator

The figure below shows the displacement of the right jaw.

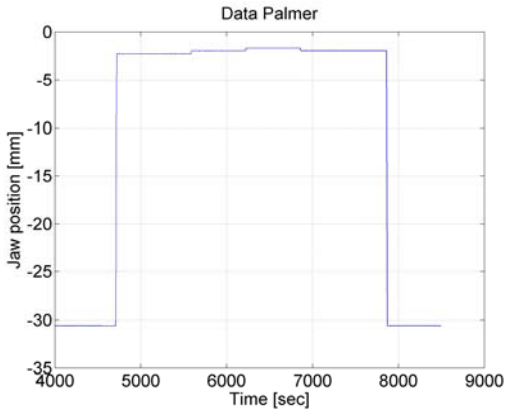

Fig. A.2: displacement of the right jaw, upstream side

The right motor on the upstream side is acted to move the jaw of 0.3 mm to have an angle of 0.3 mrad (the length of the jaw is 1 m). The figure below shows the displacement measured by the palmer. The position of the jaw is going up from -1.9186 mm to -1.6272 mm and then is going down to -1.9056 mm; the mechanical play of 13 µm is only measurable by this capacitive gauge.

This device worked well and it provides a high resolution and a measurement accuracy of 3.5 µm which is below the LHC requirements. The probe seems to work properly in the radioactive environment because it does not have active electronics. Many aspects remain to be addressed (robustness over thousands cycles, electric stability with the radiation etc.) but it does not seem more critical than the other proposed solutions. Therefore, it should be seriously taken into account as an option for the LHC.

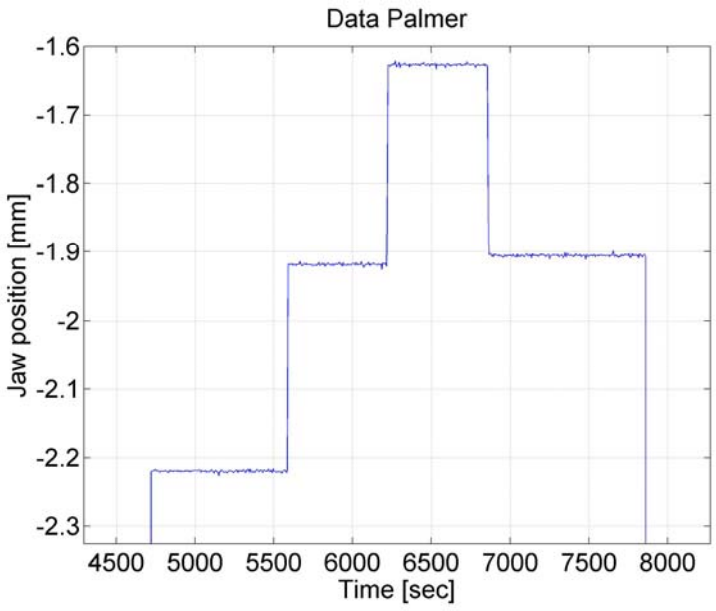

Fig.A.3: 0.3 mm displacement

APPENDIX B

Studies of the Dose Rate in ECA4 due to Beam Losses in TT40

This note describes a series of FLUKA simulations designed to estimate the dose rates in ECA4 due to protons impacting on the external beam dump (TED) in the TT40 tunnel and from losses in the proton line just in front of the mouth of TT40 entrance to the TA40 access tunnel. The ECA4 underground area at Point 4 of the SPS will house equipment associated with the extraction of the SPS beam towards the LHC and the CNGS facility. ECA4 must be accessible at all times and is separated from the beam area (ECX4) by a wall of concrete that varies in thickness from 4.8 to 5.0 m. The extracted beam will pass through the TT40 tunnel which is connected to ECA4 via an access gallery (TA40). A plan of this TA40 tunnel is given in Figure B.1.

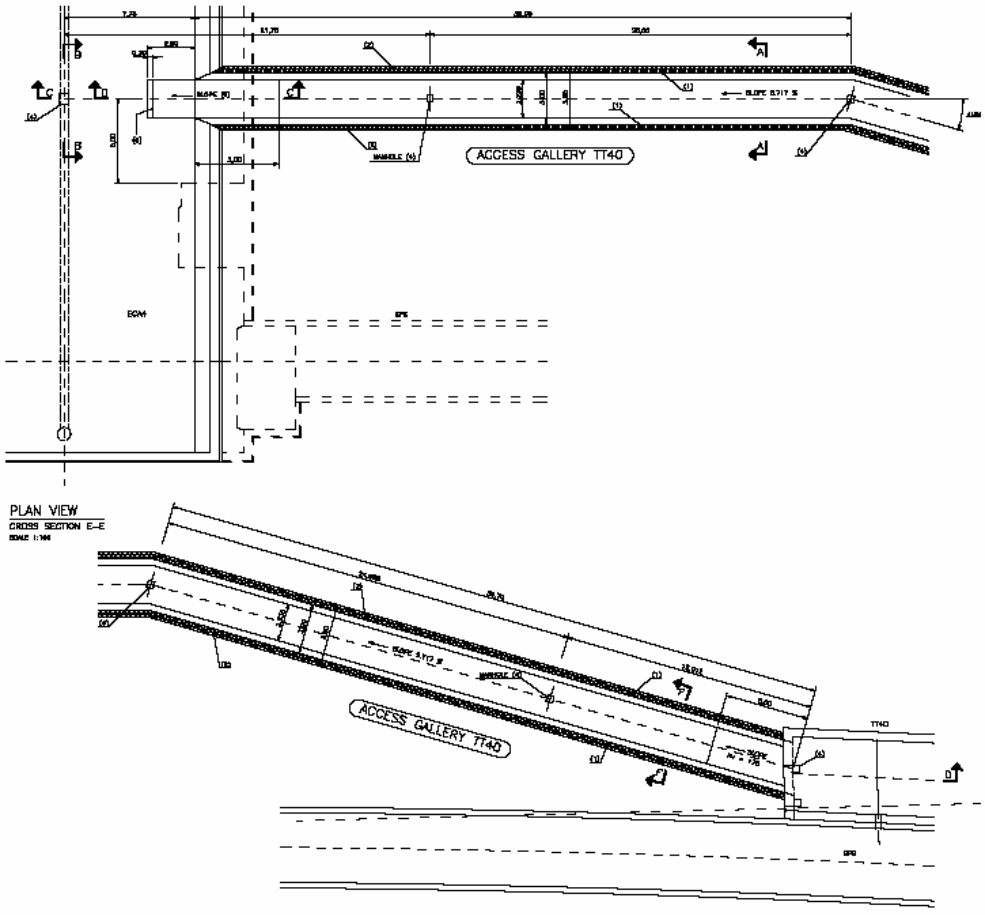

Fig. B.1: Plan view of the TA40 Access Tunnel.

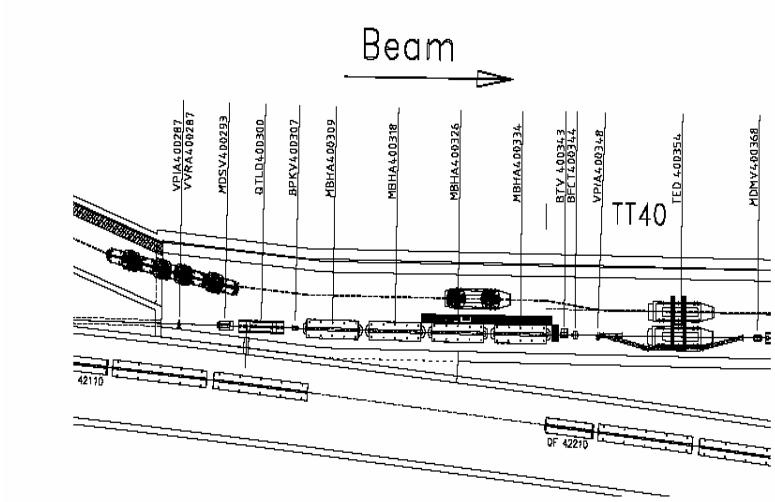

Fig. B.2: Layout of the beam-line in TT40

For the simulations, the source particles were protons at an intensity of 1.2 x 10^{13} protons per second interacting either in the TED or in an iron cylinder of 5 cm radius placed on the beam axis at the entrance to TA40 (an "optimum" target). In the TA40 tunnel there is a strong reduction of the dose rate as one passes out of the direct view of the TED.

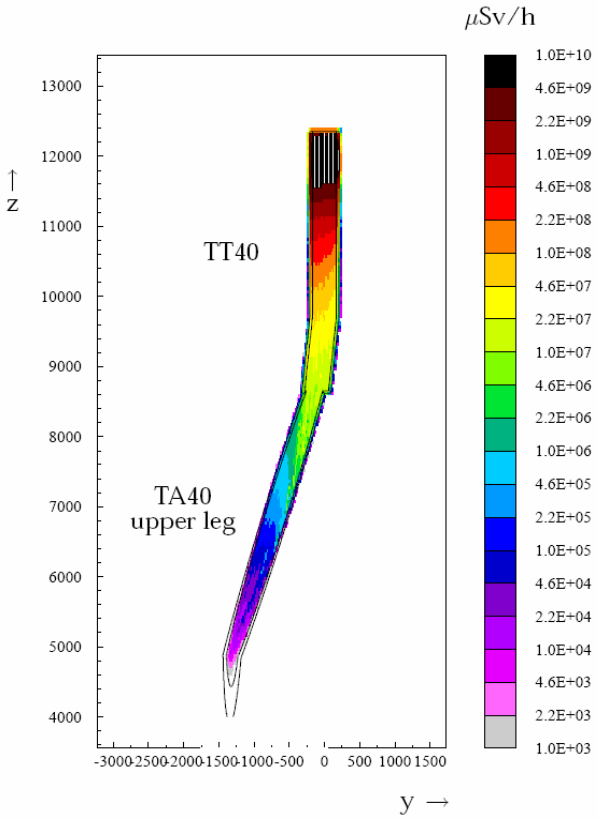

Fig. B.3: Dose rate contours in μSv/h at the floor level of TT40 due to proton interactions in the unshielded TED. All dimensions are in cm.

Out of the direct line of the tunnel entrance, the dose rate is reduced by more than an order of magnitude.

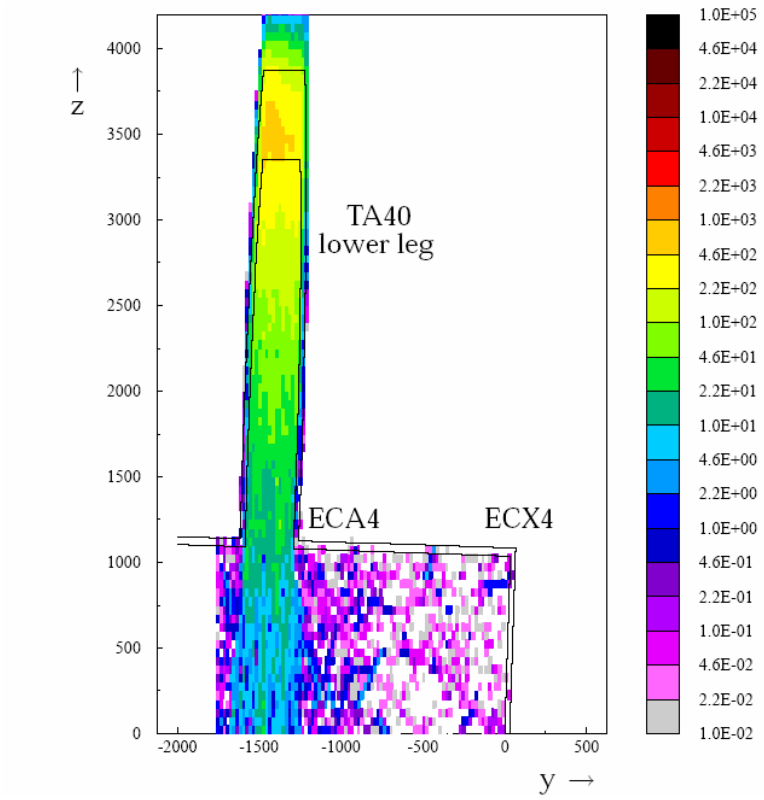

Fig. B.4: Dose rate contours in μSv/h in the lower leg of TA40 and at the floor level of ECA4 due to proton interactions in the unshielded TED. All dimensions are in cm.

The results of this simulations show that the dose rate, in μSv/h, decreases only in the lower leg of TA40.